Evelyn Zottler

Interactions between Metal Ions and pH-Sensitive Nitroxides
An EPR Study

Diplomarbeit

zur Erlangung des akademischen Grades einer
Diplom-Ingenieurin

der Studienrichtung Technische Chemie
erreicht an der

Technischen Universität Graz

Univ.-Prof. Mag.rer.nat. Dr.phil. Georg Gescheidt-Demner

Institut für Physikalische und Theoretische Chemie

Technische Universität Graz

2010

Statutory Declaration

I declare that I have authored this thesis independently, that I have not used other than the declared sources/resources, and that I have explicitly marked all material which has been quoted either literally or by content from the used sources.

Eidesstattliche Erklärung

Ich erkläre an Eides statt, dass ich die vorliegende Arbeit selbstständig verfasst, andere als die angegebenen Quellen/Hilfsmittel nicht benutzt, und die den benutzten Quellen wörtlich und inhaltlich entnommenen Stellen als solche kenntlich gemacht habe.

Graz, October 27, 2010 Evelyn Zottler

For Christa, Eduard
and Michaela

Acknowledgement

My special thanks go to Prof. Dr. Georg Gescheidt-Demner for giving me the possibility to work on this diploma thesis and offering guidance, patience, thought-provoking impulses, and fertile discussions whenever needed.

A big thank you to Dr. Arnulf Rosspeintner who altruistically dedicated himself to introducing me to EPR intstruments and MATLAB in the beginning of this project.

I also want to thank Dr. Lev Weiner who generously provided the nitroxide spin probes.

I want to express my gratitude towards Dr. Pawel Cias for helping me with quantum mechanical calculations. Furthermore, I would like to thank DI Christine Onitsch, DI Markus Griesser, and all my colleagues who so kindly helped me during my time here at the institute and contributed to a pleasant working environment.

My thanks go to all members of the institute for their help and support. Special thanks to Ing. Helmut Eisenkölbl who gave a helping hand whenever technical problems arose.

I am also much obliged to DI Johannes Kreutzer, not only for his generous help with LaTeX but also for his friendship and psychological support over innumerable cups of tea.

Finally, I want to thank my friends and family who supported me each in their own way during my studies. Without them none of this would have been possible.

Abstract

The aim of this work was to establish if specific interactions exist between pH-sensitive nitroxide radicals and selected metal ions. To this end, the influence of different metal salts at varying concentrations on the CW EPR spectra of two imidazoline nitroxides was studied. Among the investigated metal ions, zinc most significantly affected the spectral profile, analogous to the effect attributed to protonation of the nitroxide imino nitrogen known from pH studies. Simulations showed the acquired spectra to result from the superposition of the signals of the coordinated and the uncoordinated species. The results suggest that metal-nitroxyl interactions need to be taken into account when working with nitroxide pH probes.

Zusammenfassung

Das Ziel dieser Arbeit war, die Existenz spezifischer Wechselwirkungen zwischen pH-sensitiven Nitroxidradikalen und ausgewählten Metallionen zu überprüfen. Zu diesem Zweck wurde der Einfluss verschiedener Metallsalze in unterschiedlichen Konzentrationen auf die CW EPR Spektren zweier Imidazolinnitroxide untersucht. Unter den betrachteten Metallionen beeinflusste Zink das Aussehen des Spektrums am signifikantesten, analog dem der Protonierung des Iminostickstoffs zugeschriebenen Effekt, welcher aus Nitroxid-pH-Studien bekannt ist. Simulationen zeigten, dass die experimentell erhaltenen Spektren auf eine Überlagerung der Signale der koordinierten und der unkoordinierten Spezies zurückzuführen sind. Die Ergebnisse legen nahe, dass bei der Verwendung von nitroxidbasierenden pH-Sonden Metall-Nitroxid-Wechselwirkungen zu berücksichtigen sind.

Contents

List of Figures

List of Tables

1. Introduction

The very first reported organic nitroxide (Figure 1.1) to appear in the literature, named "porphyrexide", was synthesized in 1901 by O. Piloty and B. G. Schwerin,[1] although its radical nature was not discovered until 1951.[2] Since then, the field of stable nitroxyl

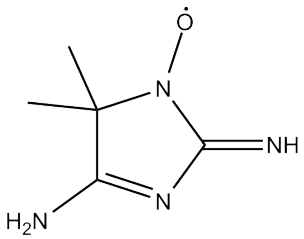

Figure 1.1.: Structure of the first organic nitroxide, porphyrexide.

radicals and their applications has undergone unforeseen evolution and expansion. This has certainly been aided by the tremendous advancements in computational approaches, digital electronics, microwave technology, superconducting magnets, and the development of advanced EPR instrumentation and new sophisticated magnetic resonance methods. Nowadays, nitroxides are used as spin oximeters, antioxidant drugs, regulators of radical polymerization, and as efficient probes to investigate, for example, microstructure, membrane properties, and specific interactions at a molecular level in many biologically and technically relevant systems.

Among the vast range of synthesized nitroxide structures, the group of imidazoline and imidazolidine nitroxides has become one of particular interest to the scientific community. Distinct spectral changes dependent on the protonation state of their imino nitrogen atom make them potent molecular pH-meters. However, despite an impressive number of publications in this field, there are almost no reports on whether nitroxides could also serve as indicators for interactions with metal ions. The aim of this work therefore was to examine, on the basis of simple systems, how different metal ions interact with two selected persistent radicals of the pH-sensitive imidazoline nitroxyl series. The method chosen for this study was Continuous Wave Electron Paramagnetic Resonance (CW EPR) spectroscopy, a technique well established in the investigation of radicals, which provides valuable information with a minimum of experimental effort.

2. Theoretical Background

2.1. Electron Paramagnetic Resonance

This section is mainly based on the books "Electron Spin Resonance Spectroscopy of Organic Radicals",[3] by F. Gerson and W. Huber, "Electron Paramagnetic Resonance: A Practitioner's Toolkit",[4] edited by M. Brustolon and E. Giamello, and "Nitroxides: Applications in Chemistry, Biomedicine, and Materials Science",[5] by G. I. Likhtenshtein, J. Yamauchi, S. Nakatsuji, A. I. Smirnov, and R. Tamura. Due to the nature of this work, considerations focus on the technique of CW EPR in liquid solution.

2.1.1. Basic Principles

EPR spectroscopy allows the investigation of species containing at least one unpaired electron, such as organic radicals, paramagnetic transition metal ions and their complexes. It is based on the nonclassical angular momentum of the electron, the *spin*, which is characterized by the spin quantum number $S = 1/2$. In presence of an external magnetic field B_0 the spin can be pictured as a vector $\boldsymbol{S}$ precessing around this field (Figure 2.1). The quantum number m_S specifies its z component ($S_z = m_S\hbar$). m_S can either be $+1/2$ (spin up or α) or $-1/2$ (spin down or β). Due to the requirements of quantum mechanics, the x and y components of the vector are not defined. Its spin angular momentum gives rise to the magnetic moment of the electron, $\boldsymbol{\mu_e}$:

$$\boldsymbol{\mu_e} = g\mu_B\boldsymbol{S} \tag{2.1}$$

$\mu_B = \hbar e/(2m_e) = 9.2741{\times}10^{-24}\,\mathrm{JT}^{-1}$ is the atomic unit of the magnetic moment, the Bohr magneton (m_e and e are the electron mass and charge, respectively), and $g_e = 2.002319$ is the dimensionless g or Landé factor of the free electron. Depending on m_S, the z component of the magnetic moment $\mu_{e,z}$ can take one of two values:

$$\mu_{e,z} = -m_S g_e \mu_B = \begin{cases} -(+1/2)g_e\mu_B & \text{for } m_S = +1/2 \\ -(-1/2)g_e\mu_B & \text{for } m_S = -1/2 \end{cases} \tag{2.2}$$

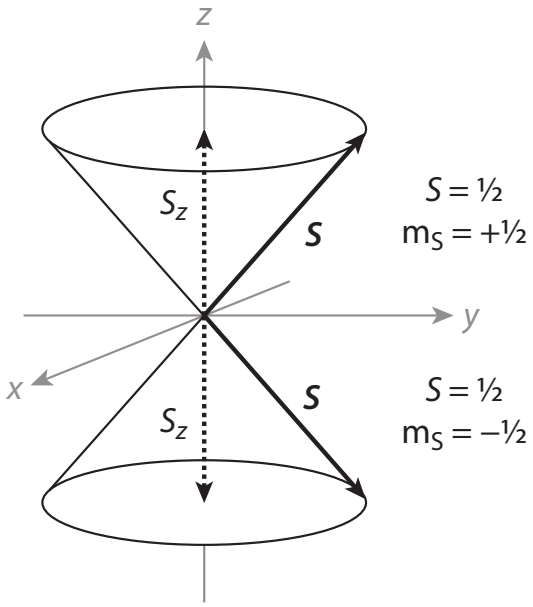

Figure 2.1.: Precession of the spin vector $\boldsymbol{S}$ (bold arrow) around a magnetic field along the z axis, and its z component (dotted arrow).

While in the absence of an external magnetic field the two spin states are degenerate, they align themselves either parallel or antiparallel in respect to a magnetic field B_0 along the z-axis, resulting in two states of different energy:

$$E = -\boldsymbol{\mu_e} \cdot \boldsymbol{B_0} = -\mu_{z,e} B_0 = m_S g_e \mu_B B_0 \tag{2.3}$$

This phenomenon is known as *Zeeman effect* (Figure 2.2). The energy difference ΔE separating the two levels is:

$$\Delta E = E_\alpha - E_\beta = g_e \mu_B B_0 \tag{2.4}$$

When an oscillating magnetic field emanating from electromagnetic radiation of $h\nu = g_e \mu_B B_0$ is applied to the system perpendicular to B_0, an exchange of spins via absorption and stimulated emission is induced between the two energy levels E_α and E_β. In contrast to Nuclear Magnetic Resonance (NMR) and other types of spectroscopy, in EPR experiments ν is usually kept constant while B_0 is varied. In X-band EPR, a frequency of $\nu \approx 9.5\,\mathrm{GHz}$ is used. Spectrometers with working frequencies over 70 GHz are referred to as high field/high frequency spectrometers. ΔE increases with the magnetic field until the resonance condition is satisfied and the energy gap matches the chosen microwave frequency, which equates to a B_0 of ca. 3500 G or 0.35 T for X-band EPR.

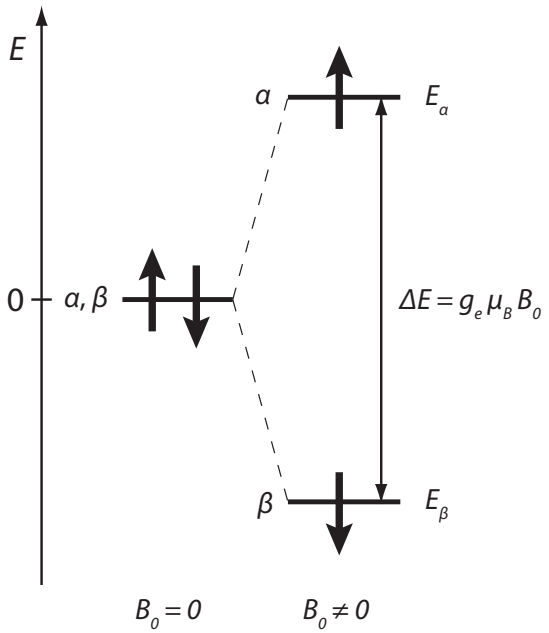

Figure 2.2.: Energy splitting due to the electron Zeeman effect. The energy gap ΔE between the α and the β state is directly proportional to the magnetic field intensity B_0.

In order to acquire a signal, many electrons are needed rather than one alone (10^{10} or more). They have to be embedded in a so-called lattice (usually atoms or molecules). If $B_0 \neq 0$, according to the Boltzmann distribution law

$$\frac{N_\alpha}{N_\beta} = exp\left(-\frac{\Delta E}{kT}\right) = exp\left(-\frac{g_e \mu_B B_0}{kT}\right) \tag{2.5}$$

more electrons of the ensemble are found in the lower energy state. N_α and N_β are the populations of the upper and lower Zeeman levels, $k = 1.3806 \times 10^{-23}\,\mathrm{JK}^{-1}$ is the Boltzmann constant, and T is the absolute temperature in Kelvin. In order to accomplish an excess of N_β, and thus magnetization, some α spins residing in the upper level E_α have to change into β spins. The associated energy transfer to the lattice is brought about by *spin-lattice relaxation* (SLR). The excess ΔN is very small ($\sim 1/1000$) but, since the probability for both transitions is the same, it leads to a net absorption of energy when the spin ensemble experiences radiation ($h\nu$). The *spin lattice relaxation time* T_1 quantifies the efficiency of SLR and can be determined by saturation experiments. It is the time in which the number of "hot" (α) spins forced out of equilibrium is reduced again by $1/e$. SLR prevents the disappearance of ΔN, and with it the EPR signal, under continuous

radiation. The equalization of N_α and N_β is called saturation and is described as follows:

$$\Delta N = \Delta N_{max} \cdot e^{(-2Pt)} \tag{2.6}$$

$\Delta N_{max} \approx \frac{N}{2} \cdot \frac{g_e \mu_B B_0}{kT}$ is the population excess at maximum magnetization in the absence of electromagnetic radiation and P is the transition probability between the two Zeeman levels. The competition between SLR and saturation results in the establishment of an equilibrium value ΔN_{eq}:

$$\Delta N_{eq} = \frac{\Delta N_{max}}{(1 + 2PT_1)} \tag{2.7}$$

The main mechanism for SLR is spin-orbit coupling. It is negligible for organic radicals without heavy atoms, which accounts for their long T_1. Thus, to keep the saturation term PT_1 small, P must be minimized by attenuating the radiation intensity to an optimum value that ensures a strong signal.

2.1.2. The g Factor

Apart from the external magnetic field B_0, an unpaired electron also experiences local magnetic fields caused by atoms close to the radical center. The effective field B_{eff} is described by

$$B_{\text{eff}} = B_0(1 - \sigma) \tag{2.8}$$

where σ sums up local magnetic effects and can reach positive or negative values. Thus, the resonance condition changes into

$$h\nu = g_e \mu_B B_0 (1 - \sigma) \tag{2.9}$$

The term $g_e(1 - \sigma)$ is called the g factor, leading to the final version of the resonance condition:

$$h\nu = g \mu_B B_0 \tag{2.10}$$

The g factor of a specific paramagnetic species determines the center of its EPR spectrum. It can be calculated from Equation 2.10 using the value of the magnetic field at which resonance occurs and the operating frequency of the spectrometer. Deviations of the g factor from the free electron value g_e are caused by a change of the electron's angular momentum due to spin-orbit coupling, which partly restores the otherwise quenched orbit contribution. For most organic radicals spin-orbit interaction is small, therefore their g factors only vary over a relatively narrow range. Nevertheless, the g factor is an important characteristic of radical species, providing information about the molecule's structure as well as its environment. It is especially valuable when hyperfine splittings (see section

2.1.4) cannot be observed because the spin-bearing atom is nonmagnetic (i.e. ^{16}O, ^{32}S).

Spin-orbit coupling originates from orbital motion. Hence, it is anisotropic. This means that the g value depends on the relative orientation of the external magnetic field and the molecular axes. It contains information about the symmetry of the spin-bearing orbital: a high σ character leads to a g value close to the one of the free electron. The axial components g_x, g_y and g_z can be determined from spectra of a single crystal, whereas in liquid solution anisotropies are averaged out and a single value $g_{iso} = (g_x + g_y + g_z)/3$ is found.

2.1.3. Line Shape and Bloch Equations

Due to the modulation used for signal amplification, an EPR spectrum is recorded and displayed in form of the first derivative of the absorption dA/dB as a function of B_0. It is characterized by the magnetic field intensity at which resonance occurs, the number and shape of lines, and their relative intensities and distances. In combination, these features provide information about the structure of the radical(s) under investigation as well as about dynamic processes and environmental interactions. The linewidth, ΔB (in mT), depends on the lifetime, Δt (in s), of the state responsible for the respective signal. This relation can be expressed by a formula equivalent to the Heisenberg uncertainty relation, $\Delta E \cdot \Delta t \approx \hbar$:

$$\Delta\nu \cdot \Delta t = \gamma_e \Delta B \cdot \Delta t \approx \frac{1}{2\pi} \tag{2.11}$$

where $\Delta\nu$ ($= \gamma_e \Delta B$; in Hz) is just another term for the width of the EPR line and γ_e is known as the gyromagnetic ratio of the electron, the ratio between the magnetic moment and the angular momentum that is used to convert a frequency ν into a field strength B (for $g_e = 2.0023$, $\gamma_e = 2.8024 \times 10^{10}\,\mathrm{HzT^{-1}}$). From Equation 2.11 follows that the longer lived the observed spin state the narrower the resulting signal. Δt in turn is governed by T_1 and T_2:

$$\frac{1}{\Delta t} \approx \frac{1}{T_1} + \frac{1}{T_2} \tag{2.12}$$

While T_1 represents the recovery of the (longitudinal) z component of the magnetization, the transverse or *spin-spin relaxation* (SSR) time T_2 describes how fast M_x and M_y vanish. It only contains interactions within the spin ensemble itself (such as spin exchange between two electrons, known as Heisenberg exchange), without any exchange with the lattice. This kind of interaction requires a certain amount of orbital overlap to become effective, as in case of high radical concentrations. For organic radicals, T_1 is much longer than T_2 ($T_2 \sim 10^{-5}$–$10^{-7}\,\mathrm{s}$) and $T_1^{-1} \ll T_2^{-1}$. Thus, the linewidth can be expressed as

$$\Delta\nu = \gamma_e \Delta B \propto \frac{1}{\Delta t} \approx \frac{1}{T_2} \tag{2.13}$$

and roughly ranges between 10^5 and 10^7 Hz (or $\Delta B \approx 0.001$–0.1 mT). ΔB can either be given as $\Delta B_{1/2}$, the width at half-height ($A_{max}/2$) in the absorption curve, or as ΔB_{pp}, the (peak-to-peak) distance along the x axis between the extrema of the function dA/dB.

Even though the behavior of individual electrons is governed by quantum mechanics, the spin ensemble on the whole behaves as a macroscopic system, with a macroscopic magnetization $\boldsymbol{M} = \sum \mu_i$ arising from a macroscopic angular momentum $\boldsymbol{J} = \sum \boldsymbol{S}_i$. The time evolution of $\boldsymbol{M}$ is described by a set of phenomenological equations, known as the *Bloch equations*, which include the two relaxation times T_1 and T_2:

$$\begin{aligned} \frac{dM_z}{dt} &= -M_y\omega_1 - \frac{(M_z - M_0)}{T_1} \\ \frac{dM_x}{dt} &= M_y(\omega - \omega_0) - \frac{M_x}{T_2} \\ \frac{dM_y}{dt} &= M_z\omega_1 - M_x(\omega - \omega_0) \end{aligned} \tag{2.14}$$

$\omega_1 = \hbar^{-1} g \mu_B B_1$ is the angular frequency at which $\boldsymbol{M}$ precesses about the oscillating microwave field B_1. The detected EPR signal is proportional to M_y, the magnetization component perpendicular to B_1. If the perturbation originating from the microwave field is a continuous one and small enough, equations 2.14 can be solved in the stationary (CW) regime giving

$$M_y = \frac{M_0}{B_0} \cdot \frac{B_1 T_2}{1 + (\omega - \omega_0)^2 T_2^2} \tag{2.15}$$

which is called the *Lorentzian* function. It represents the homogeneous line shape resulting from an ensemble of magnetically equivalent paramagnetic species, in contrast to the inhomogeneous situation occurring in immobilized samples where the spectrum is actually a superposition of the signals of many species all aligned differently in respect to the magnetic field, better approximated by a *Gaussian* curve.

2.1.4. Hyperfine Splitting

Just as an electron, a nucleus has a spin angular momentum, $\boldsymbol{I}$, with an associated spin quantum number I which can be 0 or a multiple of 1/2 (up to $I = 9/2$). If the unpaired electron experiences the proximity of a nucleus with a nonzero nuclear spin, their magnetic moments will interact. Analogous to Equation 2.1 for the electron, the nuclear magnetic moment is described by the relation

$$\boldsymbol{\mu_N} = g_N \mu_N \boldsymbol{I} \tag{2.16}$$

where g_N is the nuclear g factor, and $\mu_N = 5.0493 \times 10^{-24}\,\mathrm{JT}^{-1}$ is the nuclear magneton. g_N is characteristic for a specific type of nucleus and can either be positive (i.e. for ^{1}H) or negative (as for ^{15}N), ranging from -4 to $+6$. The z component of the nuclear magnetic moment is given by:

$$\mu_{N,z} = m_I g_N \mu_N \tag{2.17}$$

The magnetic nuclear spin quantum number m_I can amount to $m_I = -I, -I+1, \ldots, I$ ($2I+1$ values). Analogous to the behavior of an electron in presence of a magnetic field, there also is a *nuclear Zeeman effect*:

$$E = -m_I g_N \mu_N B_0 \tag{2.18}$$

The interaction between electron and nuclear spin is known as hyperfine interaction. It leads to additional allowed energy levels, resulting in a multi-lined spectrum. Therefore, in presence of magnetic nuclei, Equation 2.3 has to be adjusted to include both a term for the nuclear Zeeman interaction and one accounting for the interaction between nuclear and electron spin. Regarding the hyperfine field, the two spatial regions of inside and outside the nuclear volume are considered individually. The latter equates to the classical field of a magnetic dipole, decreasing with the third power of the distance between nucleus and electron. The dipolar interaction between the nuclear and the electron spin are only relevant in immobilized systems, such as powders, glasses, and single crystals. It is orientation dependent and averaged out by rapid tumbling in an isotropic medium. The isotropic energy contribution originating from the region inside the nucleus, E_{Fc}, usually dominates for organic radicals in fluid solution. It is called *Fermi contact* contribution:

$$E_{hf} \approx E_{Fc} = a_X \boldsymbol{S} \cdot \boldsymbol{I} \tag{2.19}$$

a_X is the *hyperfine coupling constant* (hfcc) and quantifies the interaction. For a specific type of nucleus X, a_X only depends on the spin density, $\rho_S(0)$, at the respective nucleus:

$$a_X = \frac{8\pi}{3} g \mu_B g_N \mu_N \rho_S(0) \tag{2.20}$$

Since the only orbital with a nonzero probability of finding the electron at the nucleus is the s orbital, a_X includes information about the s character of the singly occupied molecular orbital (SOMO). The absolute value of a_X can be derived from the distance between the lines of the multiplet.

Generally, n equivalent nuclei with a spin quantum number I give rise to $(2nI+1)$ equidistant lines with intensities following Pascal's triangle for $I = 1/2$. The presence of k sets of n_k equivalent magnetic nuclei each results in a spectrum comprising $\prod (2n_k I_k + 1)$

lines of which the outermost always possess the lowest intensity.

In isotropic solution, the energy contribution related to the nuclear spin is:

$$E_N = -g_N \mu_N \boldsymbol{B_0} \cdot \boldsymbol{m_I} + a_X \boldsymbol{S} \cdot \boldsymbol{I} \tag{2.21}$$

If the so-called high field approximation is met and $|a| \ll g|\mu_B|B_0$, E_N can be dealt with as a perturbation on the electron spin energy, which therefore becomes:

$$E_{tot} = g|\mu_B|B_0 m_S - g_N \mu_N B_0 m_I + a_X m_S m_I \tag{2.22}$$

Under the conditions of the high field approximation, only transitions between levels of the same nuclear spin state are observed, following the EPR selection rule ($\Delta m_S = \pm 1$ and $\Delta m_I = 0$). NMR transitions ($\Delta m_S = 0$ and $\Delta m_I = \pm 1$) would appear at much lower frequencies than those used in EPR spectroscopy and have been neglected in Equation 2.22. The nuclear Zeeman effect does not affect the gap between the energy levels involved in EPR transitions. The energy scheme for a system containing a nucleus with $I = 1/2$ is shown in figure 2.3.

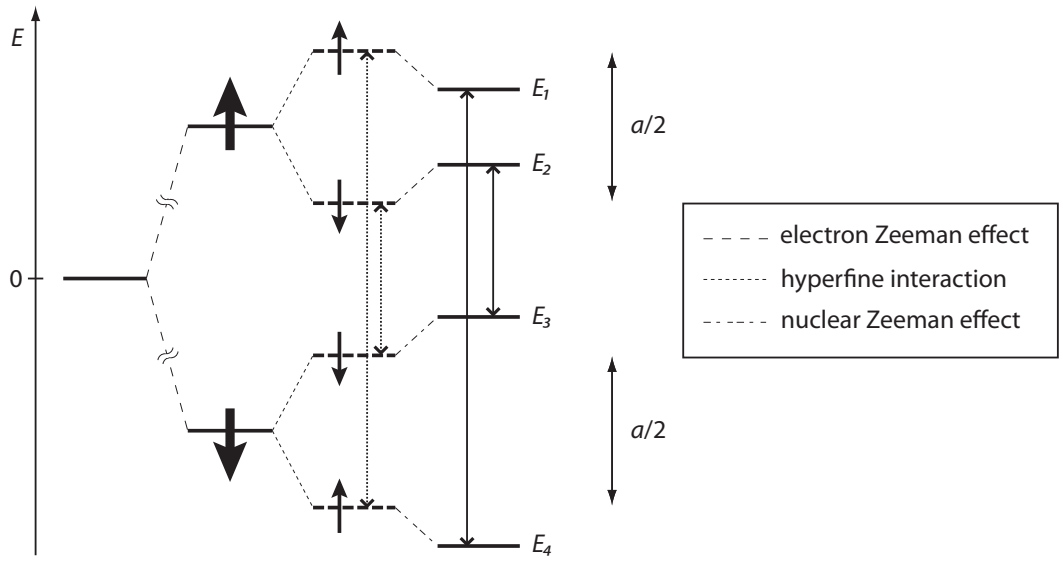

Figure 2.3.: Energy scheme (not to scale) for a radical system containing a magnetic nucleus with $I = 1/2$. The heavier and the lighter arrows illustrate the electron and nuclear spin components along the direction of the external magnetic field. The vertical double arrows represent the allowed EPR transitions. Depicted are (from left to right) the electron Zeeman interaction, the hyperfine splitting due to coupling with the magnetic nucleus, and the effect of the nuclear Zeeman term. Note that the latter does not influence the energy gap between the levels involved in EPR transitions. The signs of m_I values hold for a positive a_X. In case of a negative a_X they would be opposite.

2.1.5. Mechanisms of Spin Transfer

In most organic radicals the unpaired electron is found in a π-type orbital. However, some spin densitiy can be transferred to atoms which themselves are not part of the π system, giving rise to an isotropic hfcc a_X (with X referring to a nearby magnetic nucleus to which spin transfer occurs).

One mechanism leading to such a transfer is *spin polarization*. For example, an α hydrogen atom (^{1}H, $I = 1/2$) linked to a carbon center which is part of the π system accommodating the unpaired electron (such as in the benzene radical anion) exhibits a hfcc a_H, even though the hydrogen atom lies in the nodal plane of the spin-bearing π orbital. This results from the fact that the repulsive interactions between the unpaired electron and the electrons of the C-H σ bond are not of exactly the same magnitude for the two bond electrons. Let us assume the unpaired electron is in an α (spin up) state. Due to the Pauli principle, repulsion between two electrons of the same spin state is slightly weaker than between two electrons of opposite spin state. Therefore, the probability of finding the C-H bond α electron will be higher close to the carbon center, whereas the β electron will preferably reside near the hydrogen atom (figure 2.4). This effect is known as spin polarization. The sign of the resulting spin density at H_α is always opposite to that of the π orbital at the respective carbon atom. Thus, $a_H(\alpha)$ is negative.

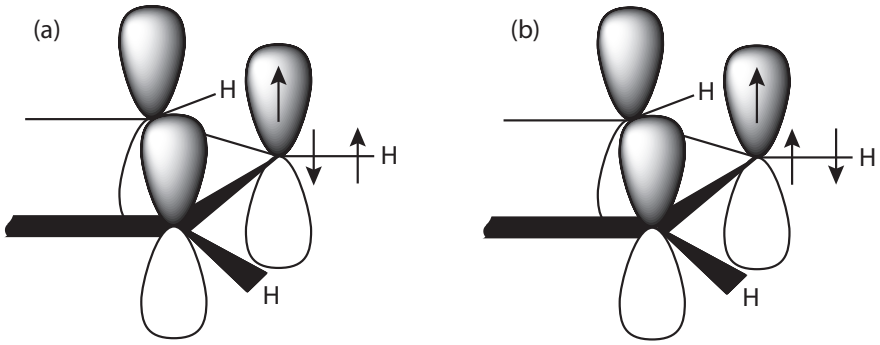

Figure 2.4.: π-σ spin polarization: due to Hund's rule and the Pauli principle, spin arrangement (b) is energetically favored.

The second possibility of spin transfer is *hyperconjugation*. Spin polarization over two or more σ bonds is very weak. Therefore, hyperconjugation is the mechanism mainly responsible for the coupling constants of atoms separated from the π system, i.e. by a sp^3 hybridized carbon atom. Spin density can be transferred from the singly occupied orbital to the 1s orbitals of the methyl hydrogen atoms through space (Figure 2.5). The efficiency of this process, in alkyl-substituted π radicals referred to as π-σ spin delocalization, depends on the dihedral angle Θ between the z axis (perpendicular to the nodal

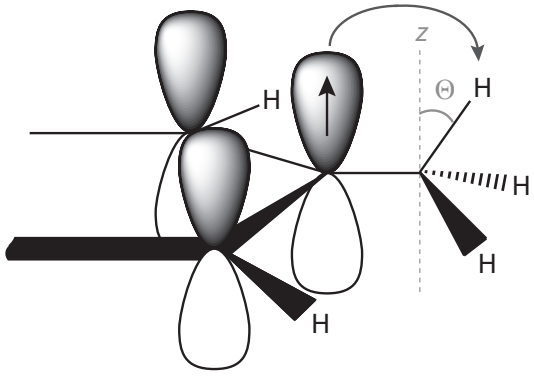

Figure 2.5.: Principle of hyperconjugation: Spin delocalization from a carbon π center to the 1s orbitals of methyl hydrogen atoms.

plane of the π orbital) and the C-H_β bond. This relation can be utilized in conformation determination studies. It is expressed by the following equation:

$$a_H(\beta) = \rho(C_\alpha) \cdot (A + B\cos^2(\Theta)) \tag{2.23}$$

where $\rho(C_\alpha)$ represents the spin density at the substituted carbon of the π system. A and B are empirical parameters. A accounts for the small contribution of spin polarization over two bonds and is often neglected, whereas B describes the effect of hyperconjugation. As a result of the direct nature of the spin transfer process, B is always positive. Consequently, $a_H(\beta)$ is of the same sign as the spin population at the π center C_α. Orbital overlap and, thus, spin transfer are maximal if the C-H_β bond is perpendicular to the molecular plane ($\Theta = 0°$; figure 2.6). In the case of a freely rotating methyl group, only one average hfcc for all three β hydrogens is found, arising from the mean dihedral angle $\langle\cos^2\Theta\rangle = 0.5$.

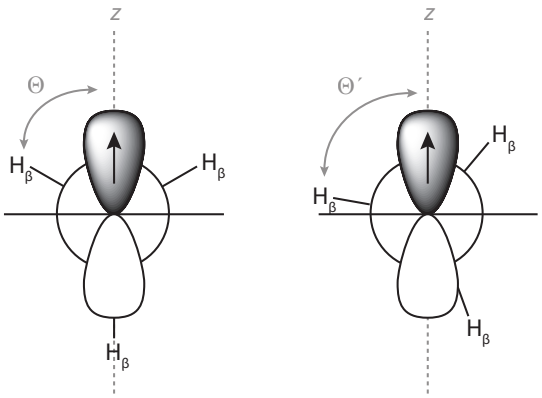

Figure 2.6.: Newman projections in the direction of the C_α-C(methyl) bond, with Θ indicating the dihedral angle between the molecular z axis and the C-H_β bond.

2.1.6. Dynamics

Dynamic phenomena, such as molecular rotations, vibrations, irregular Brownian motions, and chemical exchanges, can cause fluctuations in local fields. Their effect on the spectrum depends on the rate of the respective process compared to the dynamic time scale of EPR. In viscous media or at low temperatures for example, hyperfine and g anisotropies are often only partly averaged out and line broadening effects appear. This is especially distinct for radical species with an unpaired electron occupying an orbital of non-spheric symmetry, such as the p-type orbital of a N-based nitroxide radical (Section 2.1.7).

If a radical alternates between two states A and B which differ in their coupling constants a_i^A and a_i^B (i.e. due to proton exchange or conformational interconversion), the associated frequency jump $\Delta\nu$ is given by:

$$\Delta\nu = 2\pi\gamma_e(|a_i^A| - |a_i^B|) \tag{2.24}$$

When the rate of the underlying dynamic process, τ^{-1}, falls into the fast-exchange limit ($\tau^{-1} \gg \Delta\omega$; $\Delta\omega = 2\pi\Delta\nu$), an average hfcc is observed. In case of a very low rate ($\tau^{-1} \ll \Delta\omega$), the two states become distinguishable by EPR. For organic radicals $\Delta\nu$ values calculated from Equation 2.24 usually amount to $\sim$ 100–1 MHz. This means that any involved state with a lifetime longer than $\sim 10^{-6}$ s can be detected by EPR, while only averaged a_X and g values are observed for states shorter lived than $\sim 10^{-8}$ s. Within an intermediate time regime dynamic phenomena form the spectrum, and line shape simulations can provide valuable information about molecular dynamics.

2.1.7. Nitroxide EPR Spectra

Alkyl nitroxides belong to the class of π radicals. Their unpaired electron mainly resides in an antibonding π^*-SOMO. The carbon atoms next to the planar >NO· moiety are usually alkyl-substituted for protection, and splittings from γ protons are not resolved. The spin populations ρ_N^π and ρ_O^π are typically comparable (both $\sim$ 0.5). However, the distribution of spin density strongly depends on the polarity of the solvent. This is due to the two resonance structures of the nitroxyl moiety (Figure 2.7). In a polar environment, the ionic resonance structure (structure (b) in Figure 2.7) is energetically favored and thus spin density is shifted towards the nitrogen center at the expense of ρ_O^π, leading to a larger a_N.

The EPR spectrum of a typical nitroxyl radical consists of three equidistant lines originating from the hyperfine interaction between the unpaired electron and the ^{14}N nucleus ($I = 1$; natural abundance: 99.63 %). Although, as a result of dynamic phenomena, the intensities of the triplet lines tend to deviate from the expected 1:1:1 ratio. The concept

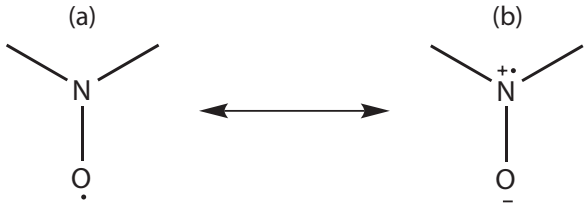

Figure 2.7.: Resonance structures of the nitroxyl moiety. In polar solvents structure (b) is favored.

considered in Section 2.1.6 also applies to a radical tumbling in solution. Its varying orientations in respect to the external magnetic field and the associated anisotropies are only incompletely averaged out if the correlation rate τ_C^{-1} of the motion is low compared to the anisotropy of the hyperfine and Zeeman interactions $\Delta\omega$ (for nitroxide radicals: ca. τ_C >10 ns). This leads to significantly increased linewidths (Figure 2.9). This line broadening effect is exploited in spin labeling studies to investigate local environments (see Section 2.2.2). The correlation time τ_C is linked to the viscosity through the Debye equation:

$$\tau_C = \frac{\eta \cdot V}{k \cdot T} \tag{2.25}$$

where η represents the local viscosity and V is the rotational volume of the spin label (or any other radical).

The broadening in magnetic field units for each line of the spectrum (ΔB) is approximated by the following expression:

$$\Delta B = A + B \cdot m_I + C \cdot m_I^2 \tag{2.26}$$

A, B, and C linearly depend on the correlation time τ_C and on the anisotropic g and hyperfine tensors. Because of the contribution of m_I the individual lines of the spectrum are broadened to a different extent. Parameters A and B contain the Larmor frequency ω_0. Therefore, the appearance of the recorded spectrum is also dependent on the frequency band of the spectrometer. Often, τ_C is determined from the line intensities using the following empirical expression:

$$\tau_C = C \cdot \Delta B_{+1} \left(\sqrt{\frac{h_{+1}}{h_{-1}}} - 1 \right) \tag{2.27}$$

ΔB_{+1} is the width of the low-field line and h_{+1}/h_{-1} is the ratio of the heights of the two outermost lines. Another possibility to acquire τ_C is to simulate the spectrum with a program developed by Freed *et al.*[6] and extract the data or by using the program E-SpiReS.[7]

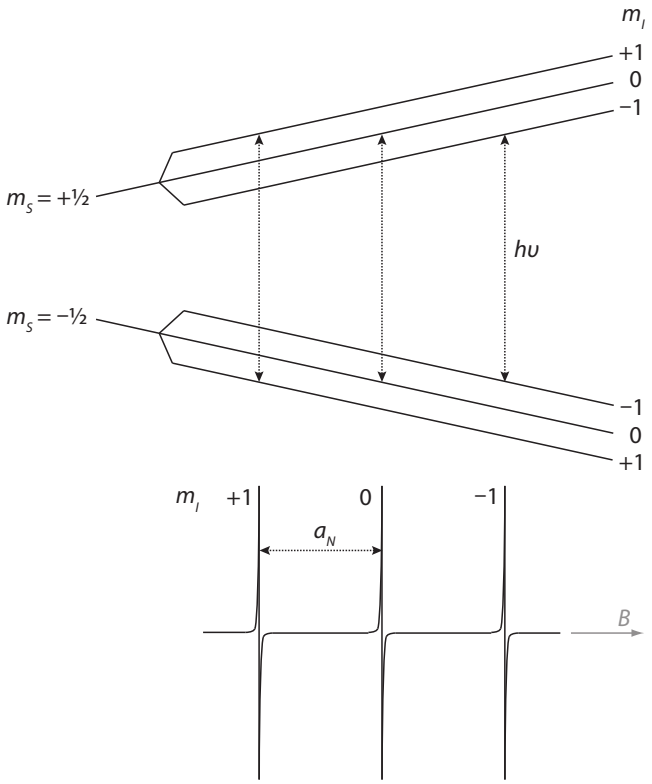

Figure 2.8.: Energy level scheme for the interaction between the unpaired electron and the ^{14}N nucleus of the nitroxyl moiety ($I = 1$) and the resulting triplet signal.

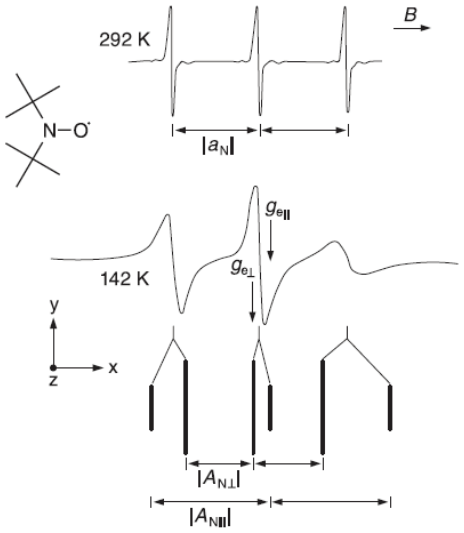

Figure 2.9.: Demonstration of line broadening effects due to incomplete averaging out of g and hyperfine anisotropies depending on solvent viscosity for di-*tert*-butyl nitroxide in ethanol at two different temperatures. Image taken from "ESR Spectroscopy of Organic Radicals" p. 138.[3]

2.2. Nitroxides

2.2.1. Introduction

First sythesized in the early 1960s,[8,9] nitroxides have become the probably most popular persistent radicals. Their long half-life times and the sensitivity of their spectromagnetic properties to local environment (polarity, hydrogen bonding power, pH and viscosity of the surrounding medium, proximity to other paramagnetic or charged species) and intramolecular effects (conformation and vibrational behavior) make them an attractive tool in various areas of application, particularly in the fields of biochemistry, biophysics, and biology. Technical advances in EPR instrumentation and the development of sophisticated new EPR techniques further extended the field of possible applications and helped to attain a more detailed understanding of underlying processes and mechanisms. Imidazoline and imidazolidine nitroxyl radicals have gained popularity because they surpass their predecessors, such as piperidine and pyrrolidine spin probes, in several aspects. Some advantages include their higher stability in acidic environments, their ability to chelate metals via the N-3 ring nitrogen atom and a substituent at position 4,[10] and their high sensitivity towards local pH (see Section 2.2.3).[11,12]

2.2.2. Applications of Nitroxyl Radicals

With the technique of site-directed spin labeling (SDSL),[13,14] valuable insights into biological structures and dynamics have been acquired. Most commonly, free cysteine thiol groups of proteins and peptides are targeted with spin labels. The development of site-directed mutagenesis in the 1990s greatly expanded the range of accessible proteins by allowing the production of mutants with cysteine residues at any desired position. The label can be attached by alkylation, acylation or the formation of a disulfide bond. The labeled protein is then separated from excess free radicals by, for example, gel filtration, dialysis or precipitation. Intramolecular distances can either be determined by introducing two spin labels or by genetically implementing a metal ion binding motif and a spin label at different sites. Based on paramagnetic interactions between the two spin labels, or between spin label and metal ion, interspin distances can be obtained, as has been done for T4 lysozyme mutants by quantitative analysis of Cu(II)-induced relaxation effects on a nitroxide spin label.[15] Similarly, the processes of ATP and metal-ATP binding in rabbit muscle phosphofructokinase were studied by Jones and coworkers.[16] The EPR spectra of the spin labeled enzyme reflected conformational changes as well as ATP and metal-ATP binding (metal = Mg, Mn), based on label mobility and dipolar interactions. The complementary employment of EPR spectroscopy, high resolution NMR of ATP protons, and Paramagnetic Relaxation Enhancement (PRE) yielded the first self-consistent 3-D model

of the protein's regulatory site.

Even though rotational diffusion of spin labels is usually a utile source of information, it can become undesirable when motions of the host molecule represent the main interest. For this purpose, Chao *et al.* introduced the idea of doubly anchored labels (Figure 2.10) which follow peptide backbone movements more closely.[17] They investigated the in-

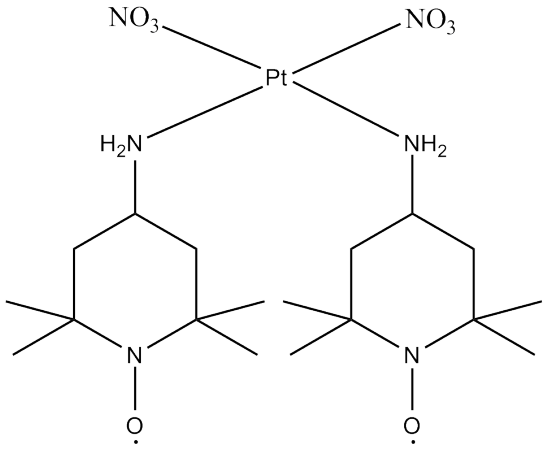

Figure 2.10.: Structure of the doubly anchored biradical synthesized by Chao *et al.*, platinum cis-(4-amino-2,2,6,6-tetramethylpiperidinyl-1-oxy) dinitrate.

teractions of biradical *cis*-platinum(II) species with poly(*L*-glutamate). Two tempamine substituents on the platinum species served as radical probes. Attachment to the peptide was achieved by the displacement of two nitrate groups by glutamate carboxylate side chains. Poly(*L*-aspartate) and poly(*L*-lysine) were less suitable due to the unfavorable length of their side chains. Changes of EPR spectral features indicated a helix-coil transition and polymer aggregation.

Nitroxides allow very accurate observations of macromolecular surfaces. This is particularly useful for proteins of which crystals for X-ray structure determinations are hard, if not impossible, to obtain, such as membrane proteins. EPR spectroscopy and SDSL make it possible to conveniently gather information on structural features and dynamics, often under physiological conditions. Owing to the high sensitivity of EPR spectroscopy, only approximately 10–20 nmol singly labeled protein are usually sufficient per sample. Proteins can even be studied directly within a membrane or micelle. Spin probes, in contrast to most fluorescent probes, are about the size of an amino acid residue and therefore unlikely to perturb the native structure of the protein. Membrane proteins are part of the complex border between cells and their surroundings and essential for cell energetics. Fractions of them can either be accessible to water, buried inside the protein or surrounded by lipid molecules. Volkov *et al.* quantified water accessibility of the plant light-harvesting complex IIb (LHCIIb) at different amino acid residues (Figure 2.11).[18] They compared the performance of several EPR techniques and corresponding accessibil-

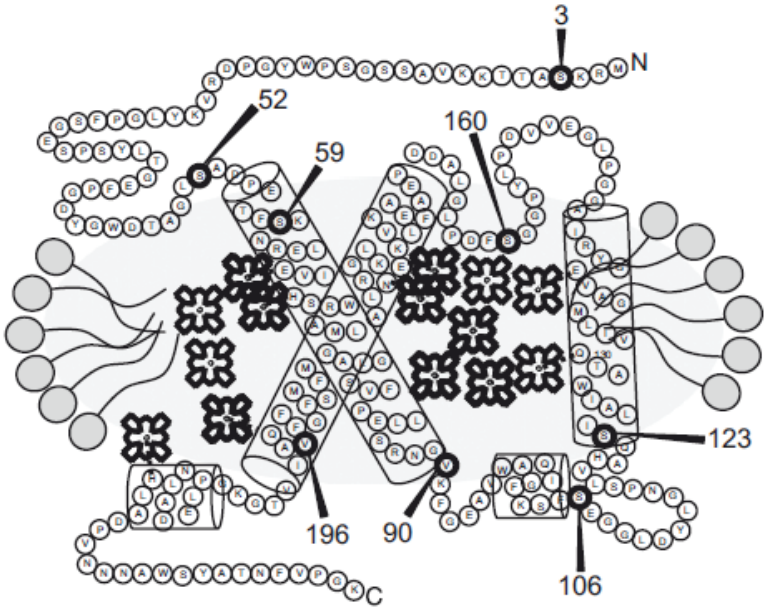

Figure 2.11.: Schematic structure of LHCIIb. Each circle with a letter represents an amino acid residue. Circles labeled with numbers show mutation positions where spin labels were attached. Cylinders represent helices, and chlorophylls are symbolized by schematic porphyrin formulas. Other pigments and lipids are not shown. The gray oval represents the micelle. The top corresponds to the stromal side and the bottom to the lumenal side of the thylakoid membrane. Picture and description taken from Volkov *et al.*[18]

ity parameters. The A_{zz} principle component of the hyperfine tensor obtained by X-band CW EPR spectroscopy of shockfrozen samples was found to depend on the local dielectric constant. However, sensitivity and, due to line-broadening effects, overall precision were relatively low. Nevertheless, this relatively simple method was shown to give adequate results for less complex systems, like membranes and micelles. In progressive saturation CW EPR experiments, the immersion depth of the label was estimated by quantifying the accessibility of spin labels to paramagnetic quenchers, such as chromium oxalate (CrOx) or Nickel(II) ethylenediamine-N,N'-diacetic acid (NiEDDA). The relation of longitudinal relaxation times to dynamic processes is quantifiable by line shape analysis. Advantages of the technique are that measurements are conducted at physiological temperatures in fluid water solution, and a smaller relative error. However, care must be taken in choosing the quencher as it may be significantly larger compared to a water molecule, and an electric charge may lead to unwanted interactions with charges located on the protein. Electron Spin Echo Envelope Modulation (ESEEM) and the related water accessibility parameter $\Pi(D_2O)$ proved the most robust and most precise among the investigated approaches. The method allowed estimates of the distance and number of deuterium nuclei in proximity of the spin label on length scales between $\sim$3–6 Å.[19] In summary, almost

all parameters showed a strong correlation and provided complementary information on water accessibility. Only $\Pi(CrOx)$ correlated poorly with the other parameters, probably due to the bulkiness and/or negative charge of the quencher.

RNA structure is crucial in molecular recognition and gene expression. Spin probes are able to distinguish even subtle variations of surface structure and can help reveal dynamic motions and conformational changes. The use of TEMPOL (4-hydroxy-2,2,6,6-tetramethylpiperidine-1-oxyl) as probe in combination with multidimensional NMR spectroscopy (2-D ^{1}H-^{13}C HSQC) yielded detailed information on the dynamic surface accessibility of both stable and dynamic RNA molecules in good agreement with the predicted data.[20] The technique is based on the ability of the nitroxide to enhance paramagnetic relaxation, leading to line broadening and an attenuation of cross-peak intensity, the extent of which depends on the local radical concentration which in turn corresponds to surface accessibility. The spin probe should ideally be water-soluble and small enough to approach structural details of the surface. It must not interact strongly with the macromolecule. Common probes are TEMPOL,[21–25] Gd(III)DTPA-BMA,[26] $Gd_2(L7)(H_2O)_2$[27] and O_2.[28]

Furthermore, nitroxides allow the characterization of membranes and their dynamic properties. n-(4,4-dimethyl-3-oxazolidinyl)oxy-octadecanoic acid (n-DSA) spin probes are frequently used for this purpose, n denoting the site of the nitroxyl moiety in the alkyl chain. Lebedeva *et al.* investigated the location of pyrene in sodium dodecyl sulfate (SDS) micelles.[29] The distance between the spin probes (methyl esters of 5- and 16-DSA;

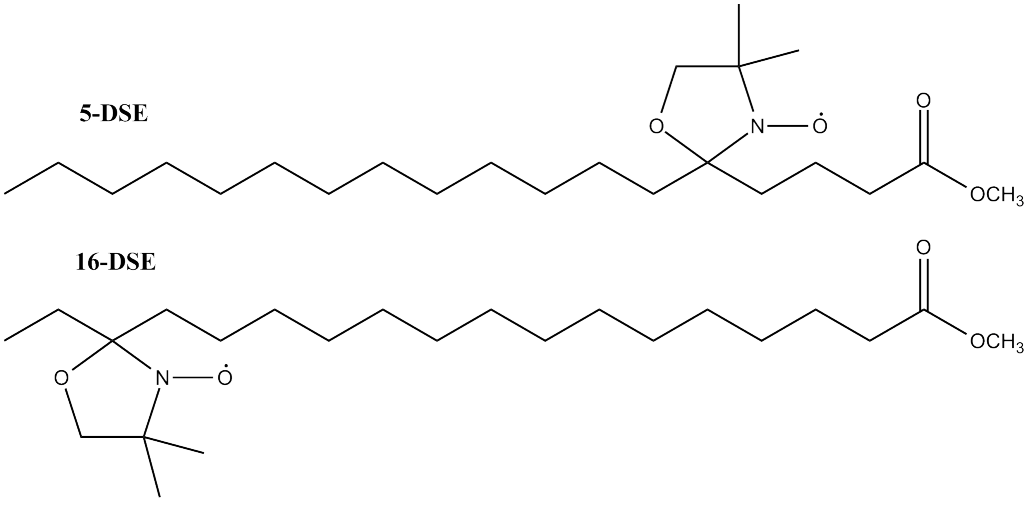

Figure 2.12.: Structures of the spin probes 5-DSE and 16-DSE.

Figure 2.12) and pyrene was determined based on the ability of the probes to quench pyrene fluorescence. The hydrodynamic theory used to attain the quenching rate constant requires information on local microviscosity which is accessible via EPR spectroscopy. The location of the methyl esters within the membrane was known from previous work.[30]

Nakagawa studied the rotational and translational diffusion of spin labeled aliphatic chains in poly(oxyethylene)hydrogenated castor oil (HCO) vesicles in aqueous solution (Figure 2.13).[31] The results were obtained by a combination of CW EPR and saturation recovery

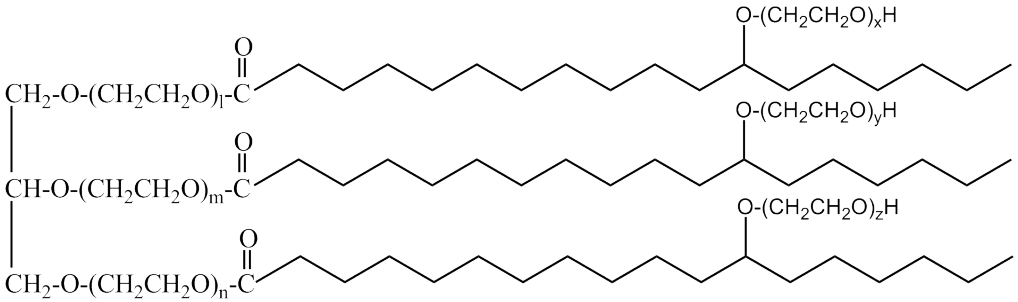

Figure 2.13.: Structure of poly(oxyethylene) HCO (l, m, n, x, y, z $\sim$ 10).

methods, the former providing rotational diffusion coefficients and the latter information on membrane fluidity and translational diffusion. The application of spin probes with the nitroxide substiuent at different locations along the molecule (7-, 12-, and 16-DSA) showed that membrane properties vary along the aliphatic chain (Figure 2.14). Often, a

Figure 2.14.: EPR spectra of various DSAs in aqueous dispersed HCO at two temperatures, indicating the different membrane viscosities depending on the spin label position along the aliphatic chain. Picture taken from Nakagawa.[31]

compatible spin probe for the investigation of a specific micellar system has to be designed first. For example, perfluoropolyether surfactants (PFPE-X; X=Na^+, NH_4^+) were studied in aqueous solution with fluoroalkyl esters of carboxy pyrroline nitroxide (FPn; n=8 and 12).[32] The critical micellar concentration (CMC) was determined at different temperatures

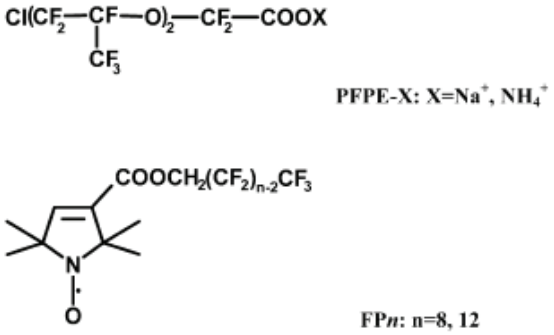

Figure 2.15.: Structures of the perfluoropolyether surfactants (PFPE-X) and the fluorinated spin probes (FPn) used by Szajdzinska-Pietek *et al.*[32]

by exploiting the dependence of the ^{14}N hfcc on medium polarity. When the surfactant concentration exceeded the CMC, a_N decreased as the spin probes were incorporated into the hydrophobic micelles. The hfcc for FP12 was found to be less sensitive, probably due to its longer alkyl chain less perfectly matching the surfactant molecules. Generally, FP8 proved to be the better indicator, featuring a sharper change in a_N occurring already at a lower PFPE-X concentration. Additionally, EPR line shapes were analyzed as a function of concentration and temperature. Linewidths increased with concentration as a result of tighter molecular packing slowing down the rotational diffusion of the probes. The ratio of the low-field and central lines were found to be sensitive to the concentration dependent transformation of aggregate shape from spherical to ellipsoidal previously determined by Small Angle Neutron Scattering (SANS) studies.[33–35] Furthermore, a counterion effect was observed. With sodium as the counterion faster probe dynamics were measured. The lower degree of counterion binding caused a higher overall charge of the aggregate, forcing it to adopt a less packed shape with a larger surface to limit electrostatic repulsion.

TEMPO (2,2,6,6-tetramethylpiperidine-1-oxyl) derivatives were used to study the influence of the hydrophobicity of flavonoids on their antioxidant reactivities in micellar systems.[36] Hydrogen transfer from phenols and polyphenols to the prefluorescent nitroxide probe led to the formation of a fluorescent and diamagnetic hydroxylamine. The reduction rate increased significantly when changing from a methanol solution to micellar media due to partitioning and the preferred location of the reactants in the membrane. Spin probes with different partition constants and locations within the micelles were achieved by varying the substituents.

Trubitsin and Tikhonov determined the pH difference between chloroplast thylakoids and the bulk of the lumen with the spin probe tempamine (4-amino-2,2,6,6-tetramethylpiperidine-1-oxyl).[37] Depending on ΔpH, the probe accumulated inside the thylakoids. In order to determine intrathylakoid tempamine concentrations, the concentration dependent broadening of the EPR signal due to spin exchange phenomena was utilized instead of adding broadening agents. Additionally, the internal volume of the thylakoids was evaluated.

The use of the spin labeling technique is not limited to biological systems but equally valuable in studying molecular structure and dynamics of synthetic polymers. Furthermore, nitroxides are important regulators of radical polymerization, then referred to as nitroxide-mediated living polymerization (NMLP). Pioneering work in this field has been done by the Neiman group. In 1966, Neiman *et al.* were the first to discover the inhibiting effect nitroxyl mono- and biradicals have on radical polymerization.[38] Since then, nitroxides have become valued and extensively investigated mediators in living homo- and copolymerization processes. The regulating function of the often phosphorous-containing nitroxides results from a phenomenon known as *persistent radical effect* (Figure 2.16).[39–41]

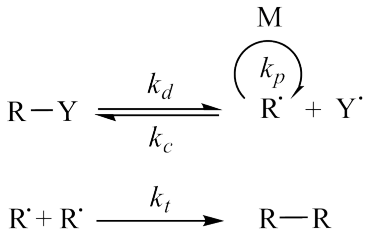

Figure 2.16.: Principle of the persistent radical effect. Y· is the nitroxide regulator, R· is the polymer radical and R-Y represents the formed polymeric alkoxyamine. k_d and k_c are the rate constants of decomposition and composition, k_t is the rate constant for the recombination or disproportion of the polymer radicals, and k_p characterizes the polymerization reaction itself.

By tuning the rate of formation and dissociation of the polymeric alkoxyamine, optimized polymers can be produced, in terms of homogeneity, chain length, and texture. Nitroxides also play an important role in the mechanism underlying the protective effect of so-called hindered amine light stabilizers (HALS). These sterically hindered amines (mostly 2,2,6,6-tetramethylpiperidine derivatives) are added to polymers for protection against oxidative degradation. In contrast to other light stabilizers, they do not absorb UV radiation but rather work similarly to antioxidants. The exact mechanism of the process is still disputed. It involves the oxidation of the amine compound to a nitroxide radical, which undergoes various further reactions and is recycled in a complex catalytic cycle called the *Denisov cycle*. A recent paper aimed for the elucidation of the process

via high-level *ab initio* calculations of the many previously proposed individual reactions on the basis of which a preferred mechanism and its most likely side reactions were presented.[42]

Nitroxides are also popular as products of spin trapping, a very pragmatic application of which is the investigation of beer staling. At elevated temperatures and in presence of air, spin trap adduct formation is observed only after the endogeneous antioxidant pool is depleted. The main product is the adduct of the spin trap phenyl-N-*tert*-butylnitrone and the 1-hydroxyethyl radicals resulting from the reaction of hydroxyl radicals and ethanol. The lag period and the kinetics of the process can be used as indicators of flavor stability and shelf-life of beer and other beverages. Kocherginsky *et al.* suggested a composite experimental parameter characterizing the antioxidant potential of beer: the product of lag time and the initial rate of spin adduct formation, normalized by the steady-state adduct concentration.[43] This new dimensionless parameter allows the comparison of results obtained on different instruments and long-term monitoring of beer quality without elaborate additional calibration.

Medicinal applications of nitroxyl radicals include their use as antioxidant drugs, contrast agents, and means to investigate the effects and mechanisms of oxidative stress. Hosokawa *et al.* investigated the role of oxidative stress on the progression of ataxia telangiectasia (A-T), a degenerative genetic childhood disease for which there is no treatment available so far.[44] They tested the influence of three water-soluble carboxy nitroxides on the survival rate of A-T cells after irradiation. In contrast to the natural antioxidant vitamine E or its water-soluble analog Trolox, all three nitroxide antioxidants led to significantly prolonged postirradiation lifetimes and reduced chromosome aberrations. Although the maximum achieved survival rates didn't reach those of healthy cells, a promising way was found to curb the degenerative progress of the disease. Due to their ability to increase the relaxation rates of solvent protons, nitroxides have aroused interest as contrast-enhancing agents in Magnetic Resonance Imaging (MRI).[45–47] In biological systems, however, they undergo bioreduction to the respective diamagnetic hydroxylamines. Yelinova *et al.* studied the influence of chemical structure on reduction susceptibility by comparing the initial rates of reduction by rat liver microsomes and ascorbate of 30 different nitroxides.[48] Five-membered ring radicals were shown earlier to be more stable towards reduction than six-membered species. Imidazolidine and 3-imidazoline proved to be the most resistant. Among heterocyclic nitroxides, substituents play an important role. An iminoxide group, for example, increases the electron deficiency on the nitroxide moiety leading to higher oxidative activity. Complex formation with paramagnetic ions can further enhance T_2 relaxativity to values about a hundred times higher.[49] However, the stability of these complexes in solution still needs improvement to make them feasible

for *in vivo* usage.

Since spin trapping in functional tissues and larger biological systems requires knowledge about biological distribution and metabolism of both the spin trap and the resulting adduct, Rosen *et al.* measured the pharmacokinetics of two nitroxides in isolated, perfused rat hearts using low-frequency EPR.[50] Nitroxide spin labels and spin probes are also versatile tools in dermatological research. They are used to probe hydrophobicity, fluidity, pH and, for example, the oxygen content of the skin or parts of it. Further applications of persistent free radicals and EPR spectroscopy in the field of skin and hair research can be found in P. M. Plonka's review on the topic published in 2009.[51]

Nitroxides are also valuable probes for the characterization of novel solvent systems. Ionic liquids are salts consisting of organic cations and organic or inorganic anions which are liquid at room or working temperature. Compared to conventional solvents, they exhibit unique properties, such as virtually nonexistent vapor pressure, non-flammability and high termal stability, which make them interesting for organic and inorganic synthesis, electrochemistry, separation processes and polymer chemistry. Solvent properties can be tuned by modifying cation and anion structure. When selecting the ideal ionic liquid for a specific job, it is important to regard macroscopic behavior as well as molecular interactions between solvent and solute. Two fundamental microscopic characteristics are microviscosity and micropolarity, both of which can be evaluated with spin probes. A study using TEMPO, TEMPOL and CAT-1 (4-trimethylammonium iodide-TEMPO) to characterize two series of imidazolium based ionic liquids showed significant influence of microviscosity on all three probes.[52] The Stokes-Einstein relation did not apply, which is common for ionic liquids. According to their different structures and, therefore, differentially strong interactions with the ionic liquid, rotational correlation times were highest for CAT-1 (Coulomb interactions), followed by TEMPOL (hydrogen bonding) and TEMPO (van der Waals forces only). The nitrogen isotropic hfcc was used as indicator of micropolarity. The a_N values of TEMPO and TEMPOL showed no sensitivity to the structure of the ionic liquid. In contrast, due to its ionic structure, the a_N values of CAT-1 decreased with increasing alkyl chain length of the solvent cation. Charged spin probes have been specifically designed to investigate interactions with ionic liquids. Similar counterions to those of the respective ionic liquid improve solubility and prevent counterion exchange. An example of such a probe targeting interaction with the cation of an ionic liquid is 4-trimethylammonio-2,2,6,6-tetramethylpiperidine-1-yloxyl (the aforementioned CAT-1) with tetrafluoroborate or hexafluorophosphate counterions.[53]

Furthermore, nitroxide spin probes have been used to examine the properties of organic glasses. Molecules dissolved in glassy materials undergo fast librational motions as has been shown by echo detected EPR. The orientational oscillation is quantified by the

mean square amplitude of motion, $< \alpha^2 >$ (α = deviation angle from equilibrium), which can be derived from the CW EPR spectra of nitroxide radicals due to the anisotropy of hyperfine interactions and g factors.[54] $< \alpha^2 >$ values were found to linearly increase with temperature in the low temperature region. The slope of this function did not depend on the nitroxide but was linked to the strength of intermolecular interactions within the glass-forming liquid. The method is capable of distinguishing glassy and crystalline areas. Dzuba *et al.* suggested their technique for the investigation of vitrification phenomena in biological systems.

The nitroxide moiety can serve as good hydrogen bond acceptor, which has been shown for complexes of TEMPO with phenol, benzyl alcohol, diphenyl amine and dibenzyl amine.[55] The formed hydrogen bonds were found to be approximately as strong as those of ethers or esters. EPR spectroscopy proved to be an attractive alternative to Fourier transform infrared (FTIR) measurements. To determine the energy of hydrogen bonds from a_N values, the contribution of the general medium effect must be substracted, which can easily be obtained from the dielectric constant and the alcohol concentration. Detailed information on hydrogen bonding efficiency can be useful in the development of organomagnets and the reactivity of oxygen-centered radicals in general.

Macromolecular multiply charged ions are widely found both in nature (DNA, proteins) and technology (polyelectrolytes in fuel cells, cosmetics, etc.). Still, the characterization of their molecular interactions with counterions remains a difficult task. Hinderberger and coworkers recently showed the power of various EPR techniques in combination with nitroxide spin probes as counterions for the investigation of these complex electrostatic systems in solutions and networks.[56]

2.2.3. pH-Sensitive Nitroxides

The pH value is one of the most important characteristics in the field of chemistry, biology and medicine. It greatly influences a variety of catalytic reactions in cellular as well as in technological processes. The prevalent method to measure the pH is electrometrically with glass electrodes. For small closed structures, such as cell organelles and vesicles, the application of electrodes is obviously limited due to their size. For microscopic systems, NMR and fluorescence based methods are widely used. However, they do have their drawbacks, such as the rather low sensitivity of NMR spectroscopy and the often high sensitivity of the fluorescence intensity to the type of buffer and ionic power of the solution. Also, fluorescence probes are often relatively large molecules and can therefore perturb the system under investigation. A special class of nitroxides proved well suited to the task, making it possible, in combination with EPR spectroscopy, to circumvent the problems mentioned above.

The first comprehensive systematic investigation of proton exchange and its effects on the EPR spectra of stable nitroxyl radicals (SNR) was published by Khramtsov and Weiner[57] in 1988. The pH sensitivity of these molecules is caused by the reversible protonation of functional groups, in most cases an iminonitrogen atom, close to the radical center.

$$R + BH^+ \underset{k_{-1}}{\overset{k_1}{\rightleftharpoons}} RH^+ + B \tag{2.28}$$

The protonated (RH^+) and unprotonated (R) forms of the respective radical differ in their spectral features. The EPR line shape is given by: (Emsley *et al.*, 1965; Khramtsov and Weiner, 1987, 1988a):[58]

$$G(B_0 - B_R) = Jm\left[i \cdot G_0 \cdot \frac{\tau_{RH^+} + \tau_R \cdot (p_{RH^+} \cdot \alpha_R \cdot p_R \cdot \alpha_{RH^+})}{(1 + \alpha_R \cdot \tau_R)(1 + \alpha_{RH^+} \cdot \tau_{RH^+}) - 1}\right] \tag{2.29}$$

τ_R and τ_{RH^+} are the lifetimes of radicals R and RH^+, B_0 is the constant magnetic field and B_R the field at the center of the EPR signal of R. G_0 is the numerical coefficient. $p_R = \tau_R/(\tau_R+\tau_{RH^+})$, $p_{RH^+} = \tau_{RH^+}/(\tau_R+\tau_{RH^+})$, $\alpha_R = (1/T_2)_R - i\cdot\gamma\cdot(B_0 - B_R + \Delta\omega/\gamma)$, and $\alpha_{RH^+} = (1/T_2)_{RH^+} - i\cdot\gamma\cdot(B_0 - B_R)$. $\Delta\omega$ is the difference in frequencies of corresponding lines in the EPR spectrum of the radical species R and RH^+. $(T_2)_R$ and $(T_2)_{RH^+}$ are the transverse relaxation times of R and RH^+, respectively. γ is the gyromagnetic ratio.

Depending on the pK_a value of the nitroxide, frequency exchange can be slow, intermediate or fast. The lifetimes, τ_R and τ_{RH^+}, and the rate constants, k_1 and k_{-1}, are accessible in case of intermediate exchange ($\tau_R^{-1}, \tau_{RH^+}^{-1} \sim \Delta\omega$). Fast ($\tau_R^{-1}, \tau_{RH^+}^{-1} \gg \Delta\omega$) or slow ($\tau_R^{-1}, \tau_{RH^+}^{-1} \ll \Delta\omega$) exchange only allow determination of the ratio τ_R/τ_{RH^+} (from Equation 2.29) from which the equilibrium constant K can be derived:[57]

$$K = \frac{k_{-1}}{k_1} = \frac{[BH^+]\cdot[R]}{[B]\cdot[RH^+]} = \frac{\tau_R}{\tau_{RH^+}} \cdot \frac{[BH^+]}{[B]} \tag{2.30}$$

Therefore, if BH^+ is a (solvated) proton H^+, pH values can be deduced from:

$$[H^+] = K \cdot \frac{\tau_{RH^+}}{\tau_R} \tag{2.31}$$

Proton exchange involves the following two mechanisms:

$$R + H^+ \underset{k_{-1}^{H^+}}{\overset{k_1^{H^+}}{\rightleftharpoons}} RH^+ \tag{2.32}$$

$$RH^+ + OH^- \underset{k_{-1}^{OH^-}}{\overset{k_1^{OH^-}}{\rightleftharpoons}} R + H_2O \tag{2.33}$$

From Equations 2.30 and 2.31, the slow exchange requirement ($\tau_R^{-1}, \tau_{RH^+}^{-1} \ll \Delta\omega$) is obtained:[57]

$$lg\left(\frac{k_1^{H^+}}{\Delta\omega}\right) < pK, \quad pH < 14 - lg\left(\frac{k_1^{OH^-}}{\Delta\omega}\right) \tag{2.34}$$

Imidazoline radicals ($\Delta\omega \approx 3 \times 10^7\,\mathrm{s}^{-1}$; diffusion control, $k_1^{H^+} \approx k_1^{OH^-} \approx 10^{10}\,\mathrm{M}^{-1}\mathrm{s}^{-1}$) with a pK_a of 3 to 11 exhibit slow exchange, a pK_a value under 3 or over 11 relates to fast and $pK_a \sim 3$ or 11 to intermediate exchange. For radicals undergoing slow exchange, addition of a buffer with a similar pK_a as the nitroxide can increase proton exchange without the need to raise the temperature. This shift into the intermediate exchange region allows quantitative determination of the equilibrium constants.[57]

In very acidic solutions, di-*tert*-alkyl and nitronyl nitroxides are protonated directly at their N-O· group. For most nitroxides in aqueous solutions, this leads to disproportionation into the respective oxoammonium and hydroxyammonium ions. However, in imino nitroxides, such as the most widely used and highly stable imidazoline and imidazolidine nitroxides, protonation occurs at their more basic N-3 ring nitrogen:[59,60] This

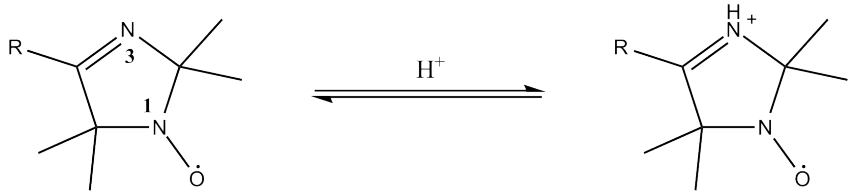

Figure 2.17.: Protonation of nitroxide N2 at the N-3 ring nitrogen.

increases the electron withdrawing power of N-3, thus reducing the importance of the charged resonance structure (b) (Figure 2.7). The resulting lower spin density on N-1 leads to a decrease of a_N (up to $\Delta a_N \sim 1.2\,\mathrm{G}$)[11] and a small increase of the g factor. Even though at X-band g value changes are rarely large enough to obtain quantitative information from, at higher frequencies, Δg can become a valuable and accurate source of information.[61] Under fast exchange conditions only one triplet with a changing a_N is found. Slow proton exchange leads to more complex spectra due to superposition of the signals of R and RH^+ at pH values close to pK_a. In X-band spectra, only splitting of the high-field component is observed, whereas spectra acquired at higher working frequencies show doublet splitting of two or all three lines of the nitroxide triplet. The dependence of a_N on proton concentration can be fitted to the conventional titration curve[57]

$$a_{H^+} = a_R \cdot \frac{\tau_R}{\tau_R + \tau_{RH^+}} + a_{RH^+} \cdot \frac{\tau_{RH^+}}{\tau_R + \tau_{RH^+}} = \frac{a_R + a_{RH^+} \cdot \frac{[H^+]}{K}}{1 + \frac{[H^+]}{K}} \tag{2.35}$$

and the following relation can be used as calibration curve for pH measurements and to

determine pK_a values:

$$a_{pH} = \frac{a_R + a_{RH^+} \cdot 10^{(pK_a - pH)}}{1 + 10^{(pK_a - pH)}} \tag{2.36}$$

pK_a values obtained potentiometrically and by EPR spectroscopy coincide within experimental error.[57]

The pH sensitivity of a series of the nowadays widely used imidazoline and imidazolidine nitroxides was first discovered in 1982 by Keana *et al.* (1982) and Khramtsov *et al.* (1982). The remarkable difference of the spectral parameters of their R and RH^+ forms in combination with the wide range of pK_a values accessible make them most promising as a tool for pH determination over a range of pH 0 to 14 (pH-sensitive $\sim$3 pH units around pK_a), with an accuracy of up to 0.03–0.05 pH units.[57,62] The acidity of the spin probes strongly depends on substitution at C-4 (ΔpK_a: up to 5). Also, according to its electron-accepting properties, the nitroxyl moiety itself lowers the pK_a of the molecule compared to diamagnetic analogues, as has been demonstrated by substituting N-O· for N-OH or N-OCH_3.[63]

The pH-sensitive nitroxides most widely used are 2,2,5,5-tetramethyl substituted. However, Kirilyuk and coworkers synthesized 2,2,5,5-tetraethyl derivatives with further improved stability against reduction and pK_a values in the neutral region, making them favorable for biological applications.[64] As mentioned above, in biological systems unwanted chemical conversions of nitroxides into diamagnetic products may interfere with their detection. Therefore, it is of interest to determine the reducibility of nitroxyl radicals. Kroll *et al.* demonstrated the use of Differential Pulse Polarography (DPP) peak potentials for this problem. With this method, they studied the influence of proton concentration and substituents on the chemical reduction of several piperidine, imidazoline and imidazolidine derivatives by ascorbate.[65]

Computational quantum chemistry provides satisfying Δa_N but often struggles with the calculation of absolute values.[62,63] More accurate results are obtained by including several solvating H_2O molecules.[66] The influence of the solvent is usually divided in bulk properties, approached with the polarizable continuum model (PCM), and specific interactions between solvent molecules and the nitroxide. Barone *et al.* combined PCM with the direct interaction of two or three water molecules close to the nitroxyl moiety.[67–70] Even better results can be gained by calculating a complete first hydration sphere, which has been done for ATI (4-amino-2,5-dihydro-2,2,5,5-tetramethyl-3-imidazoline-1-yloxy) by Ikryannikova and coworkers (Figure 2.18). Although many properties already converged at $n(H_2O) = 10$, a water shell of 41 molecules was suggested to assure reliable results.[71]

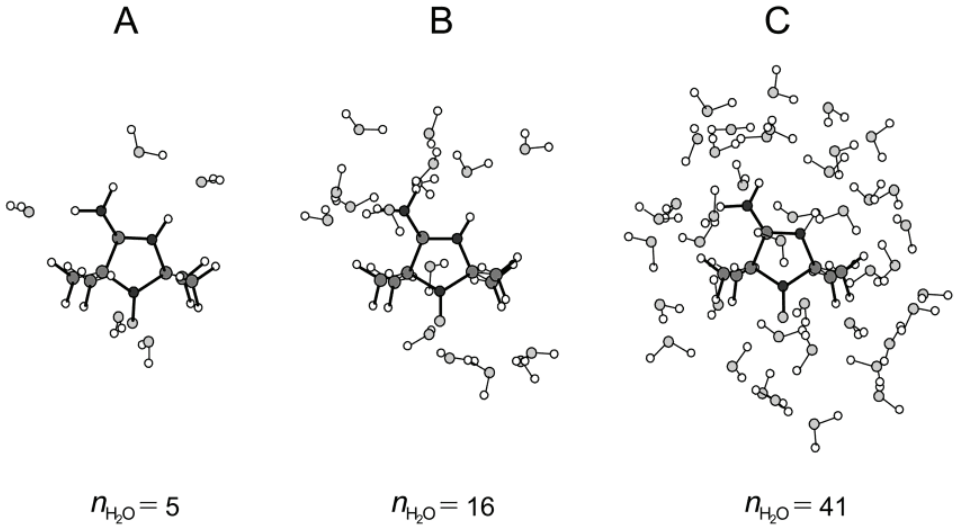

Figure 2.18.: Chemical structures of protonated 4-amino-2,2,5,5-tetramethyl-3-imidazoline-N-oxyl, ATI(H^+), surrounded by water molecules: (A) ATI(H^+) surrounded by five H_2O molecules; (B) ATI(H^+) surrounded by 16 H_2O molecules; (C) ATI(H^+) surrounded by 41 H_2O molecules. Taken from Ikryannikova *et al.*[71]

2.2.4. Applications of pH-Sensitive Nitroxides

The outstanding characteristics and well-developed synthetic chemistry of pH-sensitive nitroxyl radicals opened up a wide spectrum of applications, a selection of which is presented below, without claim to be exhaustive.

pH-probes made from a nitroxide molecule covalently bound to a macromolecule, such as a protein, can be useful in biological research.[63] pH-sensitive radicals with a substituent acting as linking group (i.e. CH_2Br) are synthesized and attached to amino acids, for example via their SH, NH_2 or NH groups. One of the earliest examples of these macromolecular spin probes was spin labeled human serum albumin (HSA).[63] Its EPR spectrum is characteristic for immobilized radicals ($\tau_C \sim 1.5 \times 10^{-9}$ s) and sensitive to pH between 1.6 and 4.6 ($\Delta a_N = 1.2$ G). Spectral changes originating from conformational variations with pH or due to the labeling procedure can be ruled out by repeating the experiment with a structurally similar but pH insensitive nitroxide.

A topic of growing interest, particularly for studying proteins, is the redox state of their thiol groups.[72] For this purpose, a symmetrical imidazoline biradical $\cdot RS-SR\cdot$ was developed.[72] The probe was used to investigate exchange with free thiols in solution. Information was obtained from the relative spectral contributions of the biradical (nine broadened lines) and the monoradical (three narrow lines) depending on glutathione (GSH) concentration. The method was successfully used to determine the concentration of GSH in erythrocytes,[72] hamster ovary cells,[73] various malignent cells,[74–76] and reperfused heart.[77]

In addition, the availability of SH groups in proteins can be estimated from the rate of protein labeling.[78,79] Furthermore, since formation of the disulfide bond is reversible, the label can easily be removed from the protein by the addition of a low-molecular-weight thiol (i.e. mercaptoethanol, reduced glutathione, cysteine). The contribution of a specific amino acid residue to protein stability and 3-D structure can be obtained by monitoring protein activity and/or structural characteristics during demodification.[80]

The investigation of intraliposomal pH and proton transfer across lipid membranes constitutes another interesting application of nitroxide spin probes. The EPR spectra of the probes encased inside the vesicles are used as indicator of pH_{in}. Its changes after the creation of a transmembrane pH gradient deliver insights into proton flux and permeability coefficients, as has been demonstrated by the examples of spin labeled glutathione,[57] sulfonic acid and dextrane[81] in phosphatidylcholine liposomes.

As already mentioned in Section 2.2.1, not only the inside of micelles and vesicels can be studied with spin probes but also well-defined sites of the membrane itself. Khramtsov *et al.* developed a reliable method to determine the surface polarity and the electrostatic potential of membranes based on the dependence of nitroxide pK_a values on these properties.[82] Imidazoline and imidazolidine nitroxides are positioned at the bilayer/water interface by anchoring hydrocarbon tails. Protonation at N-3 changes the interactions between the probe and the membrane. This affects the EPR spectrum of the radical and allows the determination of surface polarity and surface potential. Voinov and coworkers designed imidazoline and imidazolidine labeled phospholipids very closely resembling biological phospholipid structures.[83] The method is also applicable to spin labeled proteins.[82]

Nitroxides also help elucidating questions of membrane bioenergetics. Tikhonov *et al.* used imidazoline and imidazolidine nitroxides that penetrate thylakoids as pH probes inside isolated bean chloroplasts.[84] Changes of the pH-sensitive hfcc a_N and relevant calibrating curves allowed quantitative measurements of the light-induced acidification of the thylakoid lumen (Figure 2.19). The signals of internal and external spin probes were distinguished with chromium oxalate by traditional EPR line broadening technique.[37,85,86] The spin probe ATI (also used in this work) proved to be the most suitable due to its pK_a of 6.2 which is very close to steady-state intrathylakoid pH. It was shown that neither chromium oxalate nor the nitroxide radicals interfere with photosynthetic activity under the experimental conditions used.

With the help of protonable nitroxyl spin probes, Molochnikov *et al.* provided the first direct study of proton activity within the micropores of ion-exchange resins.[87] Ionization constants of functional groups, hydrolytic processes and buffer capacities were determined for different types of cross-linked polyelectrolyte sorbents. The method was suggested for the investigation of other porous systems.

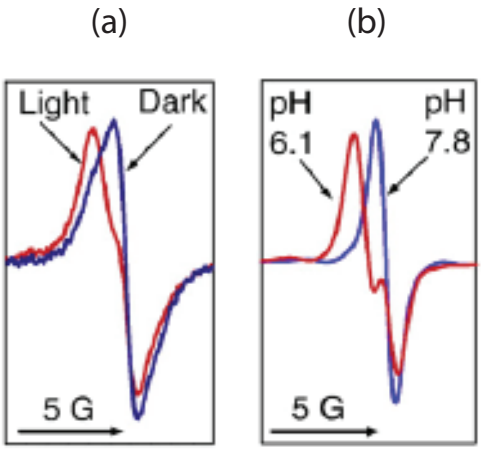

Figure 2.19.: Light-induced changes in the high-field component of the EPR signal for the spin probe ATI, localized inside the thylakoids (a), and in bulk water (b). Taken from Tikhonov *et al.*[84]

Knowledge about and accurate monitoring of pH values is also highly relevant in pharmaceutics. Optimum bioavailability and biocompatibility for various drug delivery systems require appropriate pH values. Furthermore, degradation processes of delivery systems or active compounds are often linked to pH changes. In nonaqueous, nonconducting and nontransparent media, many conventional pH measurement methods fail. Kroll *et al.* showed a simple way to circumvent laborious preparatory steps and other problems by utilizing EPR spectroscopy to continuously monitor pH values in water-in-oil ointments.[88] The a_N values of imidazoline spin probe ATI served as indicator of the changes in proton concentration over time associated with hydrolysis of acetylsalicylic acid and benzocain at different temperatures.

Bioerodible polymers have been developed for drug delivery. However, *in vivo* degradation into their acidic monomers can lead to high local acidity, potentially compromising the activity of the incorporated drug or triggering inflammatory responses. EPR imaging and a combination of pH-sensitive nitroxides were used to monitor poly(ortho ester) degradation *in vitro* over a pH range from 1.0 to 8.0 in a noninvasive, spatially resolved way.[89] Already several years earlier, Maeder and coworkers had successfully measured the release processes of a subcutaneous biopolymer drug delivery system in living mice by low-frequency EPR spectroscopy.[90]

In recent years, nanoparticles with their unusual optical, electrical, and other properties have become a field of growing interest. They are considered up-and-coming candidates for numerous applications, such as sensors, drug delivery systems, diagnostics, biomolecular recognition and many more. Both their stability and their interactions with proteins[91] and DNA[92] are strongly influenced by surface potential. Nitroxides can add to a better understanding of their behavior by characterizing the nanoparticle-solution interface. Imi-

dazoline nitroxide derivatives with hydrocarbon spacers of various length (Figure 2.20) were linked to the surface of monolayer-protected gold clusters (MPCs) via a disulfide moiety.[93] Valuable insights into the MPC surface electrostatic potential, micropolarity

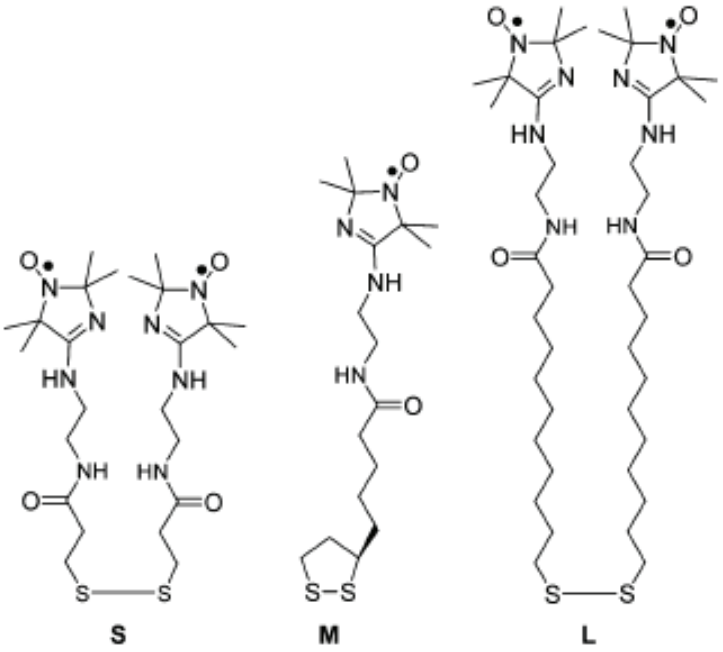

Figure 2.20.: Structures of pH-sensitive spin labeled ligands designed for anchoring to the gold surface. The labels **S**, **M**, and **L** reflect the linker length. Taken from Khlestkin *et al.*[93]

and ligand packing were gained by analysis of their pK_a values and rotational correlation times.

Imidazoline nitroxides and a Ru(III) complexes have also been used to study photo-electron transfer in solution and proteins.[62]

3. Experimental

3.1. Chemicals

In the course of the project the influence of different metal salts of variable concentration on the CW EPR spectra of pH-sensitive nitroxides was studied. All experiments were carried out, if not otherwise stated, at room temperature (ca. 296 K) with de-ionized water as solvent. The investigated imidazoline derivatives 4-(cyclohexylamino)-2,5-dihydro-2,2,5,5-tetramethyl-3-imidazoline-1-yloxy (N1) and 4-amino-2,5-dihydro-2,2,5,5-tetramethyl-3-imidazoline-1-yloxy (N2; sometimes referred to as ATI[84,94]) were generously provided by Dr. Lev Weiner (synthesized by the group of Prof. Dr. Igor A. Grigor'ev, Institute of Organic Chemistry, Russian Academy of Science, Novosibirsk, Russia; see Figure 3.1 for structures). The screened metal salts included the chlorides of lithium, sodium, potassium,

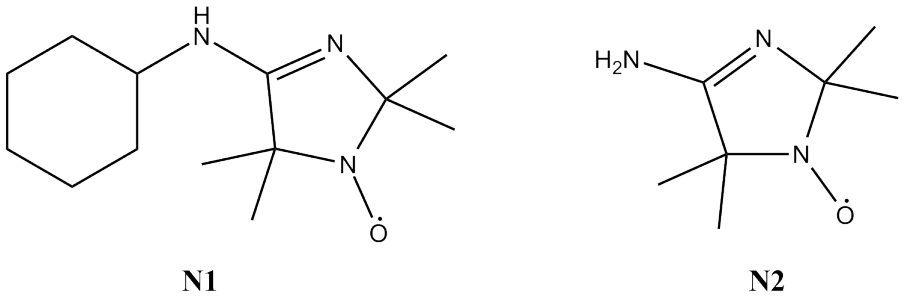

N1 **N2**

Figure 3.1.: Structures of N1 and N2.

calcium, and zinc. Furthermore, solutions of zinc fluoride, bromide, iodide, sulfate, and acetate as well as manganese sulfate were examined. The persistent radical 2,2-diphenyl-1-picrylhydrazyl (DPPH) was used as standard for the determination of g factors.

3.2. Instrumentation

X-band CW EPR spectra were acquired on a Bruker EMX spectrometer (Figure 3.2). The samples were loaded into custom made quartz capillaries (outer diameter: 3 ± 0.1 mm, inner diameter: 1 ± 0.1 mm, length: 150 ± 2 mm) and inserted into the resonator. For temperature controlled measurements liquid nitrogen was evaporated and guided through

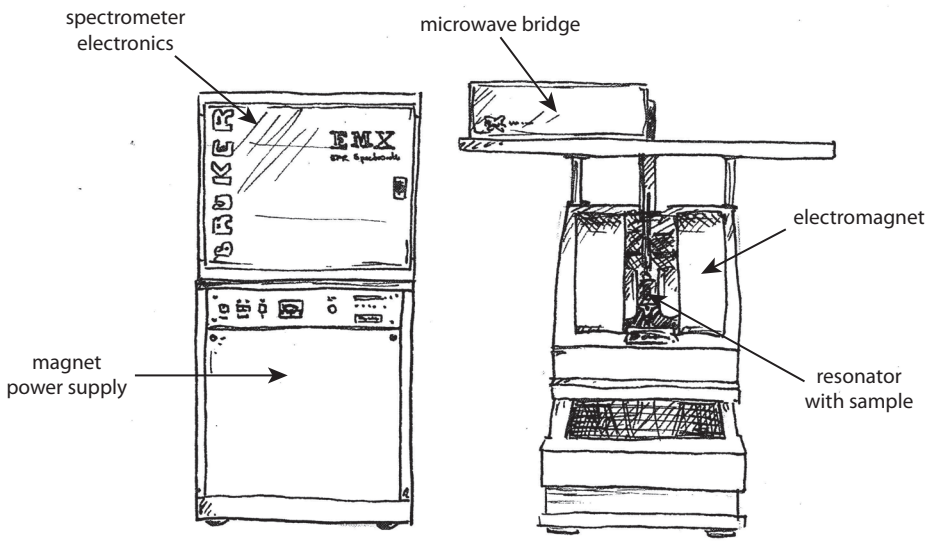

Figure 3.2.: Equipment: EPR spectrometer (Bruker EMX).

the cavity. A variable temperature unit B-VT 2000 (Bruker) was used to regulate the power needed for the heating process.

3.3. Measurements

3.3.1. Sample Preparation

For all measurements the sample concentration of the respective nitroxide was 1 mM. 2 mM stock solutions were prepared by dissolving the suitable amount of nitroxide in 5 mL de-ionized water. In the case of the rather nonpolar N1 an ultrasonic bath was used to help solubilization. Concerning the metal salts, 2 M stock solutions were made which were diluted in steps of 1:10 down to a concentration of 0.1 mM. Due to lower solubility products, the concentrations for the parent solutions of zinc fluoride, zinc acetate, and zinc sulfate were 20 mM, 1 M, and 0.2 M, respectively. 50 μL nitroxide solution was pipetted into a 1.5 mL Eppendorf tube with a 100 μL-sampler and mixed with 50 μL of the salt solution. The sample was then loaded into a quartz capillary with a 1 mL disposable syringe. The capillary was closed with a piece of parafilm, and approximately an hour later it was inserted into the resonator of the spectrometer.

3.3.2. EPR Experiments

During all experiments a microwave power of 2 mW was applied. The modulation amplitude was set to 0.5 G with the width of the central line of the nitroxide spectrum being

0.8-1.0 G. Five scans were averaged, each comprising 4096 data points. Other parameters: center field, 3489.80 G; sweep width, 77.19 G; receiver gain, 2.24×10^3; time constant, 10.24 ms; conversion time, 40.96 ms.

3.3.3. Data Analysis

EPR spectra were visualized, processed and interpreted using MATLAB 7.5.0 and the toolbox *EasySpin* (available free of charge from http://www.easyspin.org[95]). The overall a_N values for titration-type curves were obtained by reading out the distance between the low-field and the central lines of the nitroxide spectra. The obtained spectra were simulated using the program WinSIM2002, which is available for free on the homepage of the National Institute of Environmental Health Sciences (NIEHS).[96] "Nitroxide" was chosen as simulation type in the parameter menu. The spectra were calculated as a superposition of two species. The spectra of N1 with zinc bromide were additionally computed as a combination of four species to include ^{13}C satellites.

3.3.4. Quantum Mechanical Calculations

Calculations for N2 were done at the Density Functional Theory (DFT) B3LYP/SVP level by Dr. Pawel Cias. Molecular structures of the Li^+, Na^+, K^+, Ca^{2+}, and Zn^{2+} complexes were optimized in unrestricted Kohn-Sham calculations using TURBOMOLE. Total energies of the complexes were calculated in the same way. The structure and energy of the nitroxide ligand and the energies of the appropriate cations were obtained in restricted Kohn-Sham calculations at the same level of theory. In all calculations, the SVP basis set was used for all atoms.

4. Results and Discussion

4.1. Previous Work on Metal-Nitroxyl Interactions

Compared to the multitude of studies about the pH dependence of EPR spectra of nitroxides, there is surprisingly little information available about their behavior in the presence of metal salts. Most papers about metal-nitroxyl interactions focus on paramagnetic metals. There are many publications in the field of molecular magnets featuring complexes composed of a central transition metal atom and nitroxyl ligands, such as TEMPO,[97–99] nitronyl or imino nitroxides, their synthesis, structures, magnetic and spectroscopic properties. However, there are also some papers about 1:1 and 1:2 complexes between diamagnetic zinc and nitroxides. For example, Yamamoto *et al.* examined zinc(II) in addition to manganese(II), cobalt(II) and nickel(II) as central atom in their complexes with a 2-pyridyl-substituted imino nitroxide ligand.[100,101] Coordination to the metal occurred through the pyridyl and imidazoline imine nitrogen atoms. Wagner *et al.* investigated spin density delocalization from the same free radical ligand onto diamagnetic metal ions via EPR spectroscopy,[102] based on the simplified Karplus-Fraenkel expression[103]

$$a_N \approx Q_N \cdot \rho_N \tag{4.1}$$

where ρ_N is the nitrogen spin density and Q_N is the spin polarization parameter. Additional splitting of the ^{14}N triplet of the nitroxide EPR spectrum caused by interactions with zinc are usually not observed due to the low natural abundance of the only magnetic isotope ^{67}Zn (4.11 %). While considerable spin delocalization was found between the nitroxyl ligands and Group II$_B$ metals, no interaction between ligands and alkali metals or alkaline earths could be detected via solution EPR. A few years later, labile complex formation between ^{7}Li and nitroxyl radical ligands in organic solvents was described by Wagner and others using intermolecular Dynamic Nuclear Polarization (DNP) and EPR.[104] Their findings were consistent with previous studies in that coordination to the 2-pyridyl-imidazoline-1-oxyl ligands occurs through the pyridyl and imidazoline imine nitrogen atoms, while in the case of nitronyl nitroxide ligands the nitronyl oxygen atom is involved.

Waclaw Kolodziejski studied sodium and lithium cation solvation by TEMPO via EPR

hyperfine splittings, contact shift and paramagnetic broadening of the ^{23}Na NMR signal.[105] Ionic association was discussed in different solvents, and it was concluded that the alkaline metal ion is located between the anion and the nitroxyl oxygen atom in the complexes.

Zolotov *et al.* reported a method for the determination of metals using spin labeled chelating reagents.[106] The resulting complexes maintain the properties of the original radical which can be detected by EPR spectroscopy. After removing the excess nitroxide, the metal concentration is obtained from the signal intensity. Variations of the method are suggested to further facilitate the process, i.e. the use of nitroxyl reagents with strong exchange interactions, since the complex spectra would differ from their corresponding precursors, allowing detection without a separation step.

By their ability to datively bind to strong Lewis acids via lone-pairs while retaining their unpaired electron,[107] aliphatic nitroxide radicals can also be used to probe the surface of oxide catalysts, such as Al_3O_3, Al_2O_3-SiO_2, zeolites etc.[108] The method provides an advantageous means of e.g. determining the specific surface area or controlling the surface acidity of Lewis acid catalysts.

Maybe one of the most important applications for metal-nitroxyl interactions is the determination of intramolecular distances between natural or engineered metal binding sites and spin labels in proteins. The majority of those studies applies Leigh's theoretical treatment for the dipolar interaction between a paramagnetic metal ion and a nitroxide based on Redfield theory.[109,110] Voss *et al.* showed, by the example of a spin labeled T4 lysozyme mutant, that Leigh's theory can be used for the quantitative analysis of Cu(II)-induced relaxation effects to attain interspin distances not only under rigid-lattice conditions but also at room temperature under physiological conditions.[15]

Paramagnetic metals are also used as broadening agents in studies of membrane and cell interiors. By adding i.e. $[Fe(CN)_6]^{3-}$ or $[Cr(oxalate)_3]^{3-}$ the EPR lines of the nitroxide in the solution surrounding the investigated cell are broadened and the amplitude of the first derivative spectrum is decreased due to collisions with the paramagnetic metal species, thus facilitating the observation of the intracellular nitroxide.[111,112] The effectiveness of the broadening is influenced – apart from the choice of the broadening agent itself – by the concentration of the spin label and the buffer, the pH value of the medium, and the type of the buffer.

A very good survey of metal-nitroxyl interactions is given by the reviews "Interaction of Spin Labels with Transition Metals" part one[113] and two[114] by Eaton and Eaton.

4.2. EPR Experiments and Simulations

To fill the gap regarding the behavior of nitroxide spin probes in the presence of metal ions in solution, this work investigates the influence of lithium, sodium, potassium, calcium, and zinc salts on the CW EPR spectra of the two selected imidazoline nitroxides N1 and N2 (for structures see page 32 Figure 3.1). Manganese sulfate was also tested, although the EPR signal of manganese ($I = 5/2$) itself interferes with the nitroxide triplet and completely covers it at higher concentrations.

Among the tested metal salts, lithium, sodium, and potassium chloride do not remarkably influence the spectra within the range of concentrations investigated. Despite the high oxygen affinity of the lithium ion no such interaction was observed. The four methyl groups efficiently shield the nitroxyl moiety from the hydrated ion. The spectra show the triplet signal typical for nitroxides, arising from interaction of the unpaired electron spin with the ^{14}N nucleus ($I = 1$). The three lines of the spectrum are not of equal intensity due to incomplete molecular rotations and the associated g and a_N anisotropies (see Section 2.1.7). Figure 4.1 shows the high-field peaks of N1 in the absence (red) and presence (blue: 1 mM, green: 100 mM) of lithium chloride. Sodium and potassium ions

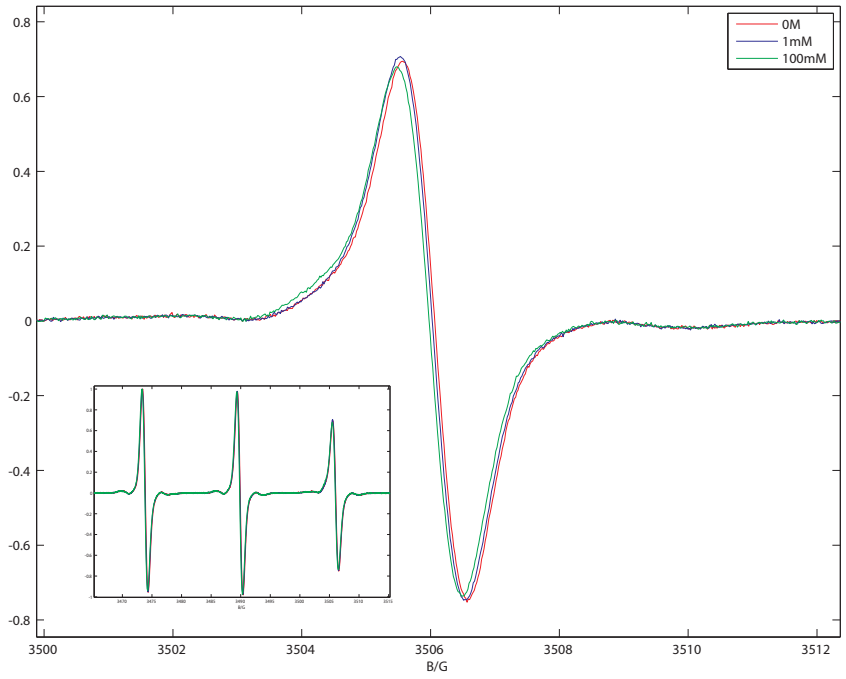

Figure 4.1.: High-field peaks and full spectra of N1 with different concentrations of lithium chloride. Red: N1 without added salt, blue: 1 mM LiCl, green: 100 mM LiCl.

behave analogously, while calcium chloride shows a small effect at high concentrations. 100 mM $CaCl_2$ led to the appearance of a second peak approximately 1 G downfield of the high-field line of the original signal (indicated by the arrow in Figure 4.2).

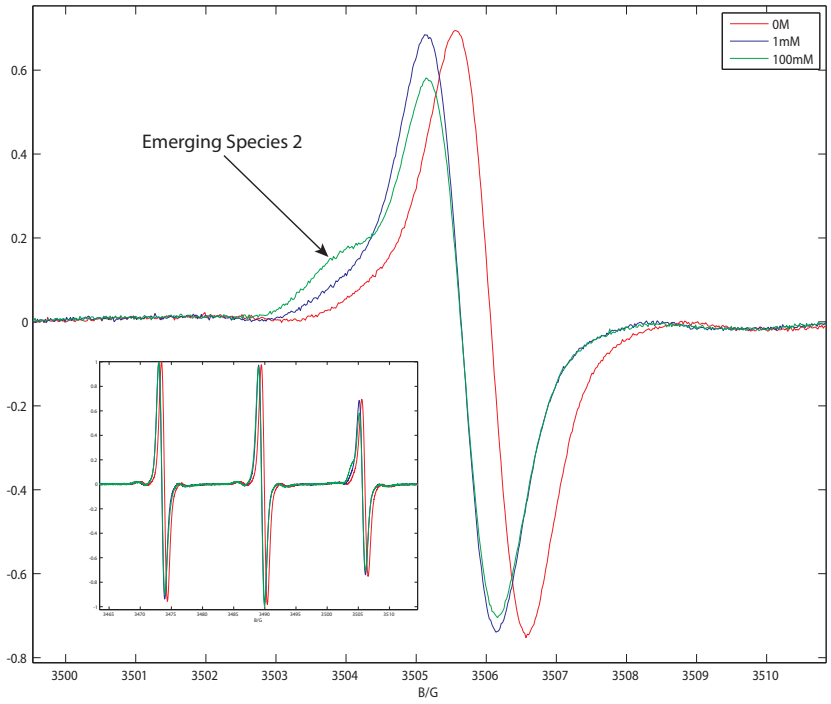

Figure 4.2.: High-field peaks and full spectra of N1 with different concentrations of calcium chloride. Red: N1 without added salt, blue: 1 mM $CaCl_2$, green: 100 mM $CaCl_2$.

The addition of zinc chloride results in a significant change of the hyperfine coupling constant and a slightly differing g value already at concentrations much lower than in the case of calcium chloride. Hereupon, other zinc salts with different anions were studied, namely zinc fluoride, bromide, iodide, acetate, and sulfate. All of the above proved to have a similar effect on the nitroxide spectra. At zinc concentrations in the range of 1–100 mM the high-field line is split into two well distinguishable components whose relative intensities depend on the salt concentration. An equivalent behavior is well known from pH studies of imidazoline nitroxides, where the pH value is varied instead of the zinc concentration. As can be seen in Figure 4.3, already 1 mM of zinc bromide change the spectrum of N1 as much as 100 mM of calcium chloride do. At a zinc salt concentration of 100 mM and more the signal with the smaller hfcc clearly predominates the spectrum. The choice of the anion does not seem to have a great influence. Although, in comparison with N1, about five times more zinc salt is necessary for N2 to reach a 1:1 ratio of the two species (see Figure 4.4 for the spectrum of N2 with $ZnBr_2$) which is not surprising as N1 also has a slightly higher pK_a value. This may be attributed to the $+I$ effect of the cyclohexyl group enhancing the basicity of the side group amine nitrogen to which it is attached.

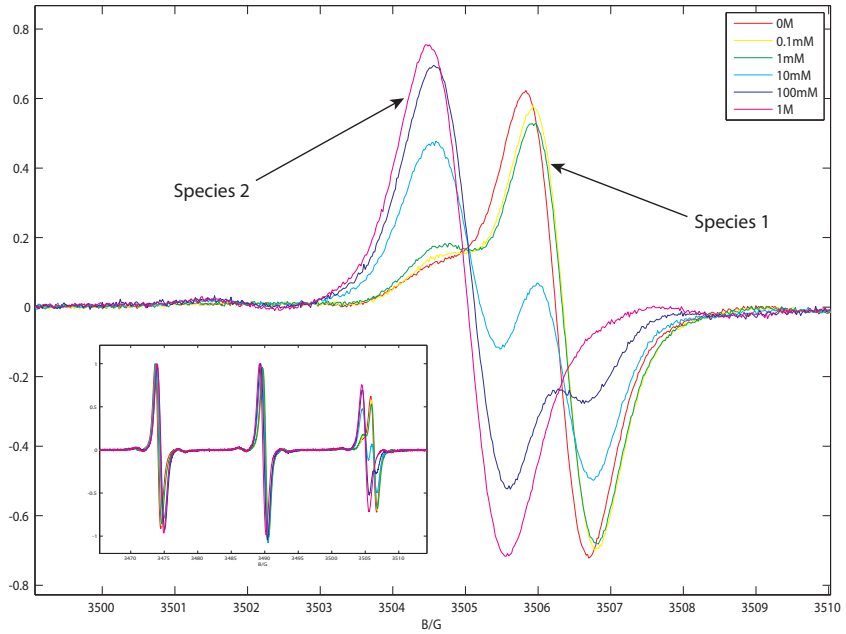

Figure 4.3.: High-field peaks and full spectra of N1 with different concentrations of zinc bromide. Red: N1 without added salt, yellow: 0.1 mM $ZnBr_2$, green: 1 mM $ZnBr_2$, cyan: 10 mM $ZnBr_2$, blue: 100 mM $ZnBr_2$, magenta: 1 M $ZnBr_2$.

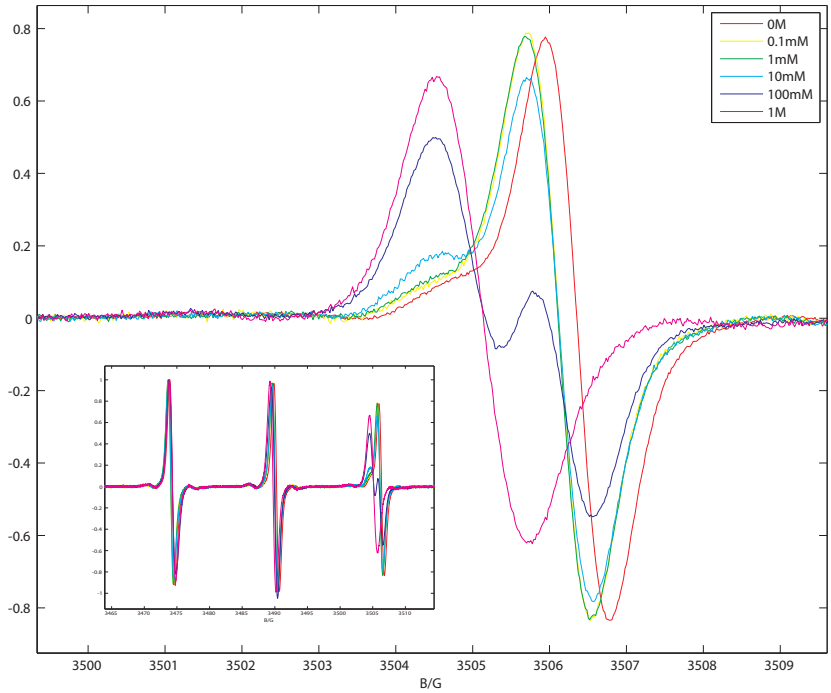

Figure 4.4.: High-field peaks and full spectra of N2 with different concentrations of zinc bromide. Red: N2 without added salt, yellow: 0.1 mM $ZnBr_2$, green: 1 mM $ZnBr_2$, cyan: 10 mM $ZnBr_2$, blue: 100 mM $ZnBr_2$, magenta: 1 M $ZnBr_2$.

The observed dependency of a_N on the zinc concentration resembles a pH titration curve fitted to the Henderson-Hasselbalch equation:[115]

$$a = \frac{a_R \cdot 10^{(pH-pK_a)} + a_{RH^+}}{1 + 10^{(pH-pK_a)}} \tag{4.2}$$

Although, the turning point appears shifted towards higher concentrations for zinc in comparison to protons (see Figures 4.5 and 4.6). a denotes the overall hfcc at a given pH value. a_R and a_{RH^+} stand for the coupling constants of the unprotonated and protonated form of the nitroxide, respectively. Even though, to a certain degree, differences between the tested anions would be expected and very small variations were indeed observed, no systematic tendencies could be identified. Fluoride, acetate, and sulphate as the strongest Lewis bases among the investigated anions (see Table 4.1 for an overview of anion properties) show the strongest association to the zinc cation. This is also apparent in the

Table 4.1.: Properties of investigated counterions. Values taken from "Ion Properties" by Yizhak Marcus (1997).[116]

Anion	z	r	V_i^∞	Hydr Nr	Stokes	Softness	β_- (calc)	β_- (Gtr)	β_- (DN)
F^-	-1	133	4.3	2.7	5.5	-0.66	2.88	2.95	
Cl^-	-1	181	23.3	2.0	3.9	-0.09	1.67	1.01	1.01
Br^-	-1	196	30.2	1.8	3.4	0.17	1.25	0.67	0.71
I^-	-1	220	41.7	1.6	2.8	0.50	0.71	0.31	0.14
$CH_3CO_2^-$	-1	232	46.2	2.2	1.1	-0.22	2.01	1.49	
SO_4^{2-}	-2	230	25.0	3.1	5.3	-0.38	2.91	6.91	

z: charge; r: ionic radius [pm]; V_i^∞: standard partial molar volume in water [cm^3mol^{-1}]; Hydr Nr: hydration numbers (model radii); Stokes: hydration numbers (employing ionic Stokes radii); Softness: dimensionless parameter[117] quantifying Pearson's concept of soft and hard acids and bases; β_-: Lewis basicity parameters obtained by different approaches (calc: calculated, Gtr: from experimental $\Delta_{tr}G^\circ$ values, DN: donor numbers from measurements).

low water solubility of zinc acetate, zinc sulphate, and especially zinc fluoride, which is the reason why for these salts no data could be obtained for concentrations higher than 100 mM. In comparison to the cations, all anions have far larger ionic radii which may sterically prevent significant interaction with the nitroxide. Several aspects seem to compete regarding the association and dissociation of anions, zinc ions, nitroxides, and solvent water molecules, including the size, charge, and (Lewis) acidity or basicity of all involved species. These complex interactions make the identification of reproducible effects for the individual counterions impossible under the experimental conditions. Higher precision experiments may be able to shed more light on anion effects. Furthermore, it would be interesting to repeat the measurements in different media to determine the influence of the solvent and to check if the observed effects are typical for aqueous solutions only.

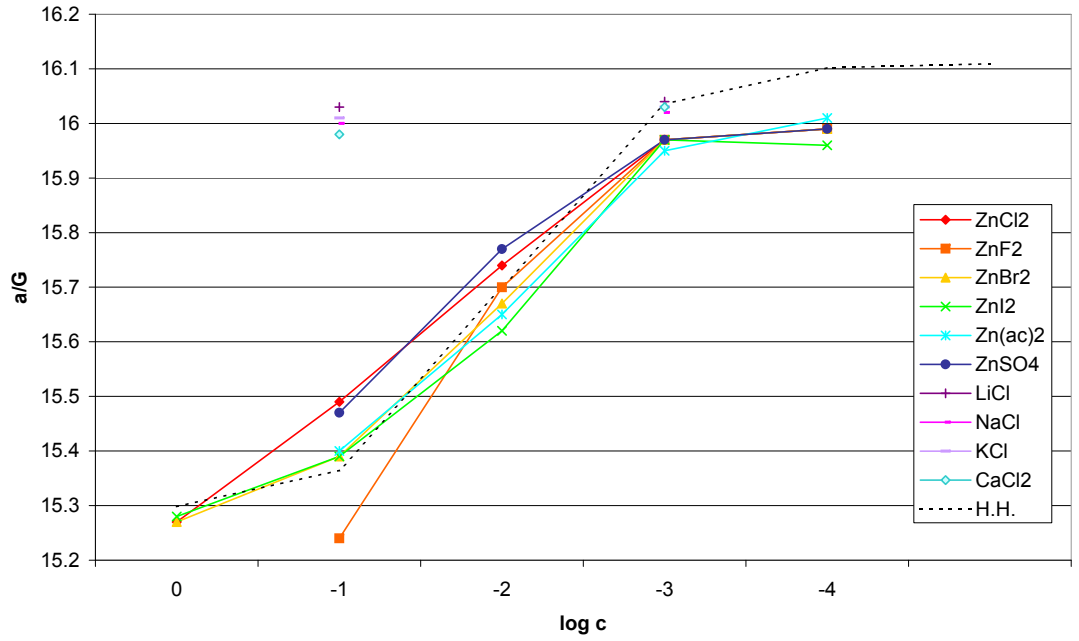

Figure 4.5.: Titration curve for N1 with different metal salts. Red: $ZnCl_2$, orange: ZnF_2, yellow: $ZnBr_2$, green: ZnI_2, turquoise: $Zn(O_2CCH_3)_2$, blue: $ZnSO_4$, purple: LiCl, pink: NaCl, lavender: KCl, aquamarine: $CaCl_2$, black dotted: Henderson-Hasselbalch-type curve, calculated with an estimated "$pK(Zn)$" of 2, in place of the pK_a.

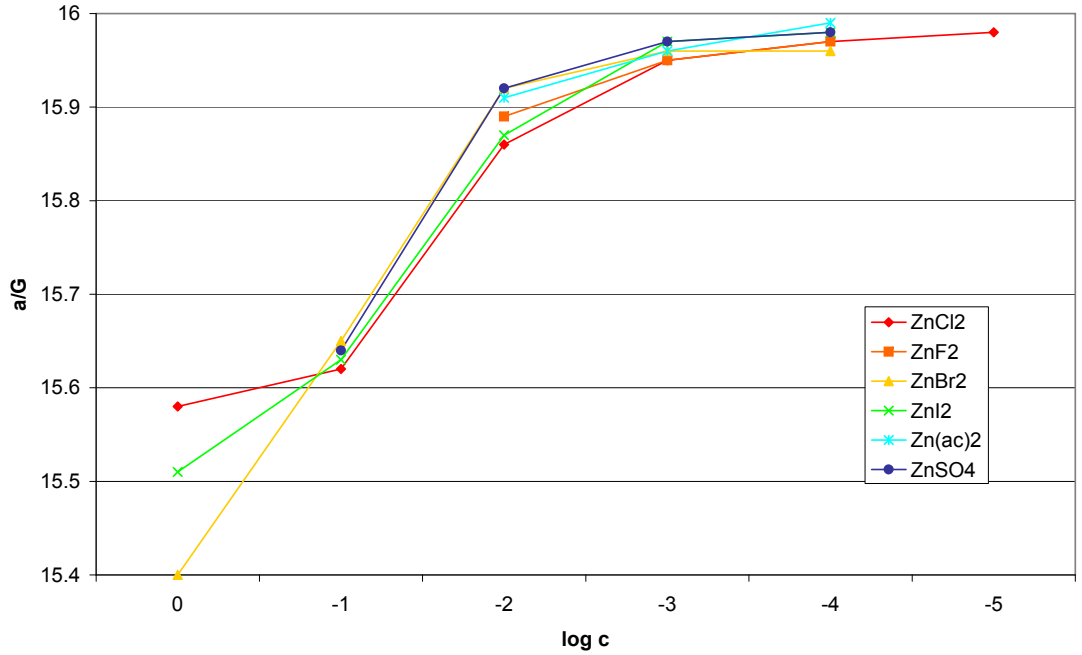

Figure 4.6.: Titration curve for N2 with different zinc salts. Red: $ZnCl_2$, orange: ZnF_2, yellow: $ZnBr_2$, green: ZnI_2, turquoise: $Zn(O_2CCH_3)_2$, blue: $ZnSO_4$

For zinc chloride, bromide, and iodide the sigmoidal titration curves were fitted with OriginPro 8 to determine equilibrium constants according to the equation:

$$y = A1 + \frac{A2 - A1}{1 + 10^{[(logx0 - x)\cdot p]}} \tag{4.3}$$

where $logx0$ is the turning point of the curve, which corresponds to the logarithm of the equilibrium constant for the formation of the coordinated nitroxide-zinc species. The results are summarized in Table 4.2.

Table 4.2.: Equilibrium constants for $ZnCl_2$, $ZnBr_2$, and ZnI_2, determined by a sigmoidal curve fit (DoseResp of OriginPro 8).

Radical	**Salt**	**logx0**	**std error**	**K**	**R^2**
N1	$ZnCl_2$	1.41	0.28	25.9	0.98234
	$ZnBr_2$	1.88	0.14	75.8	0.98594
	ZnI_2	2.02	0.19	104.4	0.95754
N2	$ZnCl_2$	1.685	0.062	48.39	0.99615
	$ZnBr_2$	1.033	0.007	10.79	0.99994
	ZnI_2	1.429	0.020	26.86	0.99973

The fitted curve for N2 in presence of $ZnBr_2$ is shown in Figure 4.7 as an example (the remaining curves can be found in the appendix). The best fits were obtained for N2.

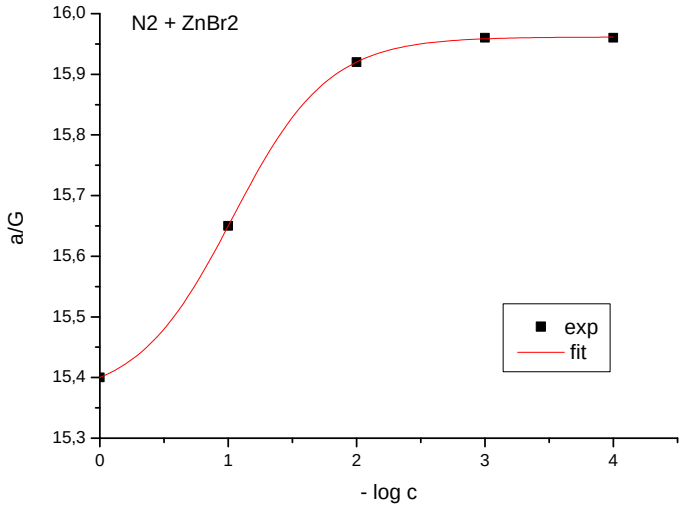

Figure 4.7.: Sigmoidal fit of the titration curve for the system N2 + $ZnBr_2$. Squares: experimental values, line: fit according to Equation 4.3

As spectrum simulations with WinSIM2002 confirm, the observed effect results from the superposition of the EPR signals of two different species: two triplets with different a_N and g factors (summarized in Table 4.3). In analogous pH studies the two species proved to be the protonated and unprotonated form of the nitroxide. Protonation occurs at the ring nitrogen in position 3.[115] The correlation between the observed a_N values and zinc salt concentrations suggests coordination of the zinc ion to the same position. Zinc acts as a Lewis acid withdrawing spin density from the nitroxyl moiety, thus lowering its a_N value with increasing concentration. The obtained a_N and g values are consistent with data reported previously in studies of proton exchange in imidazoline nitroxides.[57]

Table 4.3.: pK_a values, a_N and g factors of protonated and unprotonated forms.

		$\boldsymbol{a_N}$ (± 0.03 G)		$\boldsymbol{g}$ (± 0.0001)	
Radical	**pK_a**	**R**	**RH^+**	**R**	**RH^+**
N1	6.4	16.11	15.29	2.0062	2.0064
N2	6.2	16.03	15.21	2.0063	2.0065

The question arises in what way calcium and zinc differ from the other cations which do not have an equally substantial effect on the nitroxide spectra. In contrast to the monovalent alkali metal ions, they bear a higher charge (and charge density) and they are stronger Lewis acids. The acidity parameters of the two cations are roughly comparable. The reason for the remarkably higher effect of zinc compared to calcium may be due mainly to its smaller size. Zn^{2+} has an ionic radius of 75 pm while the Ca^{2+} cation is about 33 % larger, making an interaction with the nitroxide distinctly less favorable. Size issues may also attribute to the low nitroxide affinity of the alkali metal ions (a summary of cation properties can be found in Table 4.5). The possibility that exchange for the monovalent species may just be too fast on the EPR timescale to be observed cannot be completely ruled out either.

Low level DFT calculations (B3LYP/SVP) for N2 further support the experimental results. Table 4.4 contains the ΔE values for the metal-nitroxyl complexes (for computational details see Section 3.3.4). Even though the very high values provided by the quick calculations must be considered rough approximations only, they qualitatively show a trend. Complexation is least favorable for the alkali metal ions, with the bulky K^+ clearly

Table 4.4.: DFT results: ΔE values (in $kJmol^{-1}$) for the metal-nitroxyl complexes of N2.

	Li^+	**Na^+**	**K^+**	**Ca^{2+}**	**Zn^{2+}**
ΔE	-205	-106	-6.82	-358	-697

showing the weakest and Zn^{2+} the strongest interactions. Structures of the calculated complexes can be found in the appendix (Supplement D).

Table 4.5.: Properties of investigated metal ions. Data taken from "Ion Properties" by Yizhak Marcus (1997).[116]

Cation	z	r	V_i^∞	Hydr Nr	Stokes	Softness	α_+ (calc)	α_+ (Gtr)	α_+ (AN)
Li^+	+1	69	-6.4	5.2	7.4	-1.02	1.24	2.07	1.97
Na^+	+1	102	-6.7	3.5	6.5	-0.60	0.89	0.83	0.88
K^+	+1	138	3.5	2.6	5.1	-0.58	0.85	0.85	0
Ca^{2+}	+2	100	-28.9	7.2	10.4	-0.66	3.54		2.67
Zn^{2+}	+2	75	-32.6	9.6	11.3	-0.35		3.67	6.04

z: charge, r: ionic radius [pm], V_i^∞: standard partial molar volume in water [cm^3mol^{-1}], Hydr Nr: hydration number (model radius), Stokes: hydration number (employing ionic Stokes radius), Softness: dimensionless parameter[117] quantifying Pearson's concept of soft and hard acids and bases, α_+: Lewis acity parameters obtained by different approaches (calc = calculated, Gtr = from experimental $\Delta_{tr}G^\circ$ values, AN = acceptor numbers from measurements).

Even in the absence of metal ions the nitroxide spectra seem to consist of two species which may be attributed to partial protonation of the imine nitrogen, since in the neutral aqueous sample solutions pH was relatively close to the pK_a values of the investigated substances (N1: $pK_a = 6.4$; N2: $pK_a = 6.1$). Spectra of N1 and N2 were recorded without the addition of metal salts at pH 4.0 and 9.2. Only species 2 was present at pH 4.0, while at pH 9.2 species 1 exclusively accounted for the spectrum (Figure 4.8), which supports the above assumption.

The two smaller humps to both sides of each triplet line are ^{13}C satellites which can be simulated by factoring in approximately 3 % of ^{13}C atoms ($I = 1/2$) with an a_N value of 6.4 ± 0.1 G (Figure 4.9). ^{13}C satellites were only simulated for the spectra with zinc bromide. They were ignored in all other simulations for reasons of simplicity.

At zinc salt concentrations of 1 M the spectra show presence of species 2 alone for N1. For N2 these high concentration spectra could not be satisfyingly simulated. The curves in Figure 4.11 and 4.12 depict the varying compositions of the spectra for N1 and N2. For the purpose of clarity, the diagram for N1 in the presence of zinc chloride (see Figure 4.10) is shown separately. At a zinc chloride concentration of 1 M the spectrum is solely made up of species 2 (dashed line). With lower zinc salt concentrations the amount of species 2 decreases in favor of species 1 (solid line) until the equilibrium composition for the present pH value ($\sim$85 % species 1, $\sim$15 % species 2 for zinc chloride and N1) is reached at approximately 0.1 mM.

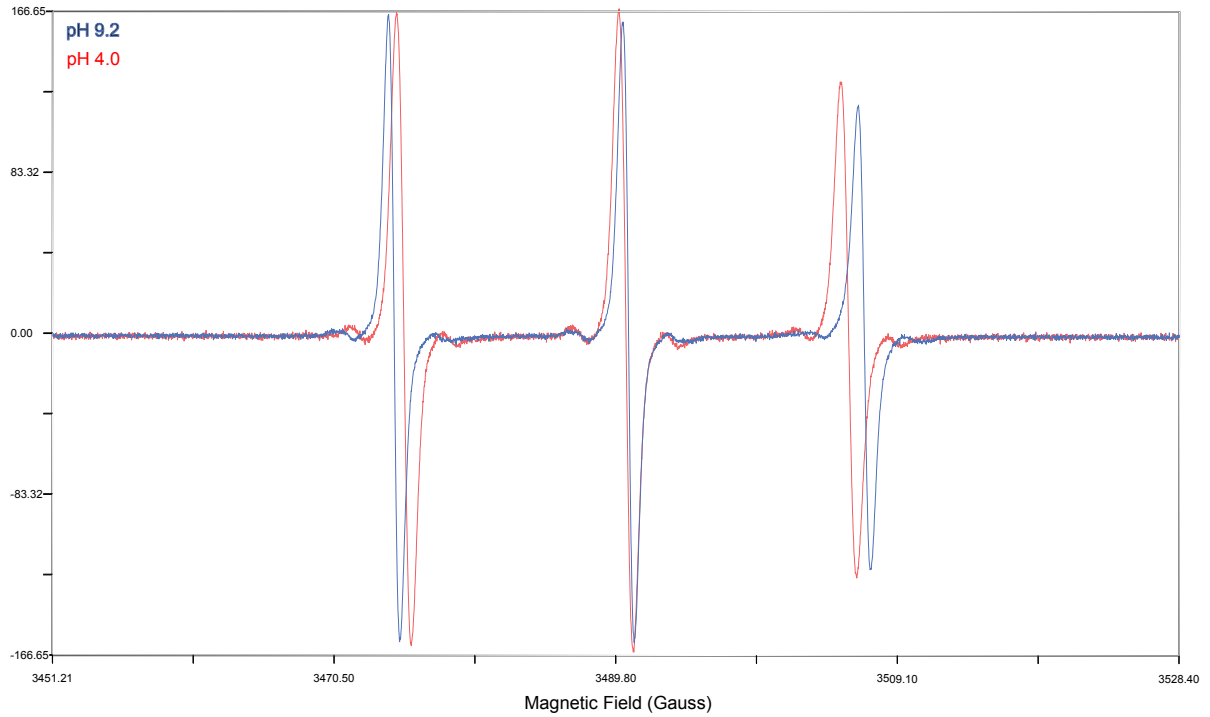

Figure 4.8.: EPR spectra of N1 for different pH values. Species 2 at pH = 4.0 (red), species 1 at pH = 9.2 (blue).

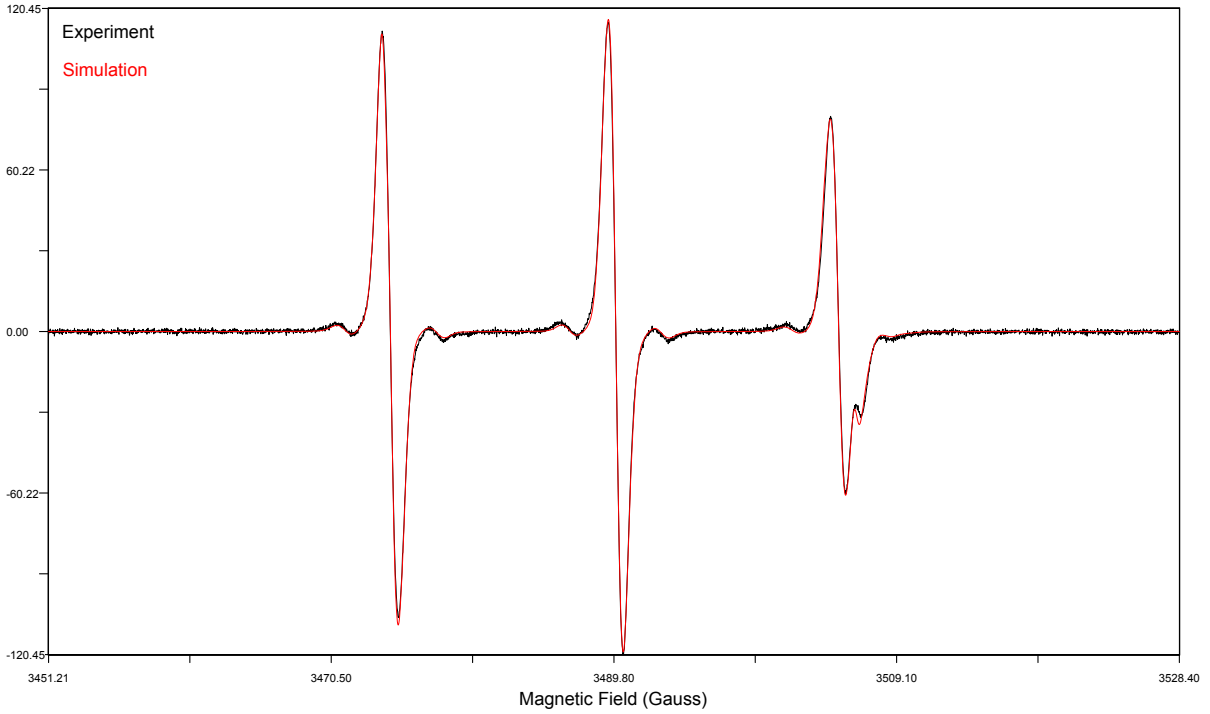

Figure 4.9.: Simulation including 3 % ^{13}C with a hfcc of 6.3 G, exemplified by the spectrum of N1 in presence of 100 mM $ZnBr_2$. Black: Experimental, red: simulation.

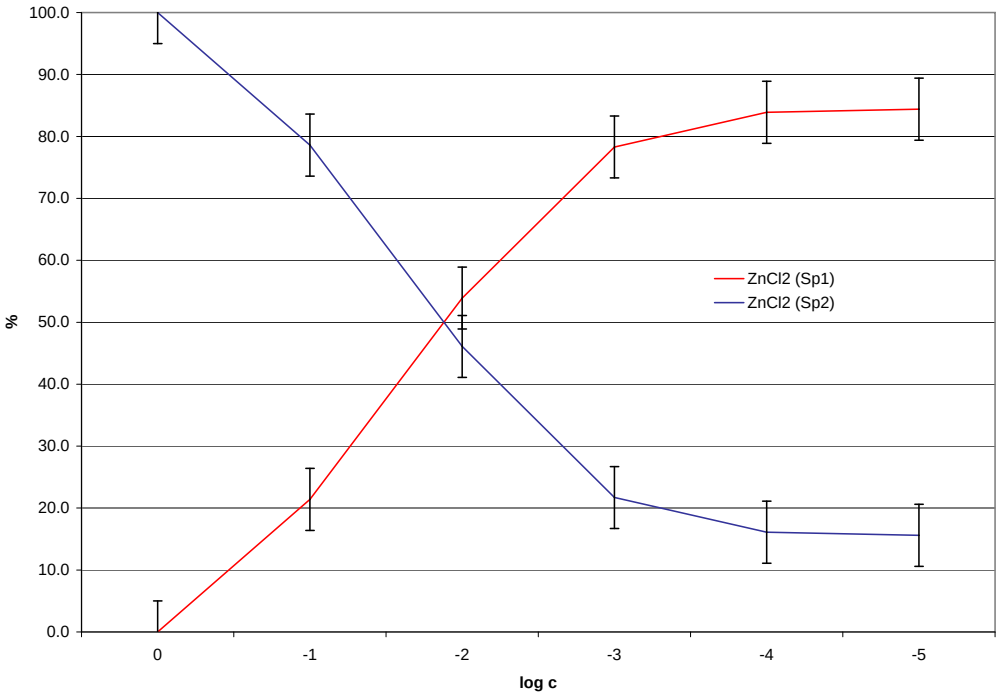

Figure 4.10.: Relative amounts of species 1 and 2 depending on zinc chloride concentration for N1. Ascending red graph: Species 1 (Sp1), descending blue graph: Species 2 (Sp2).

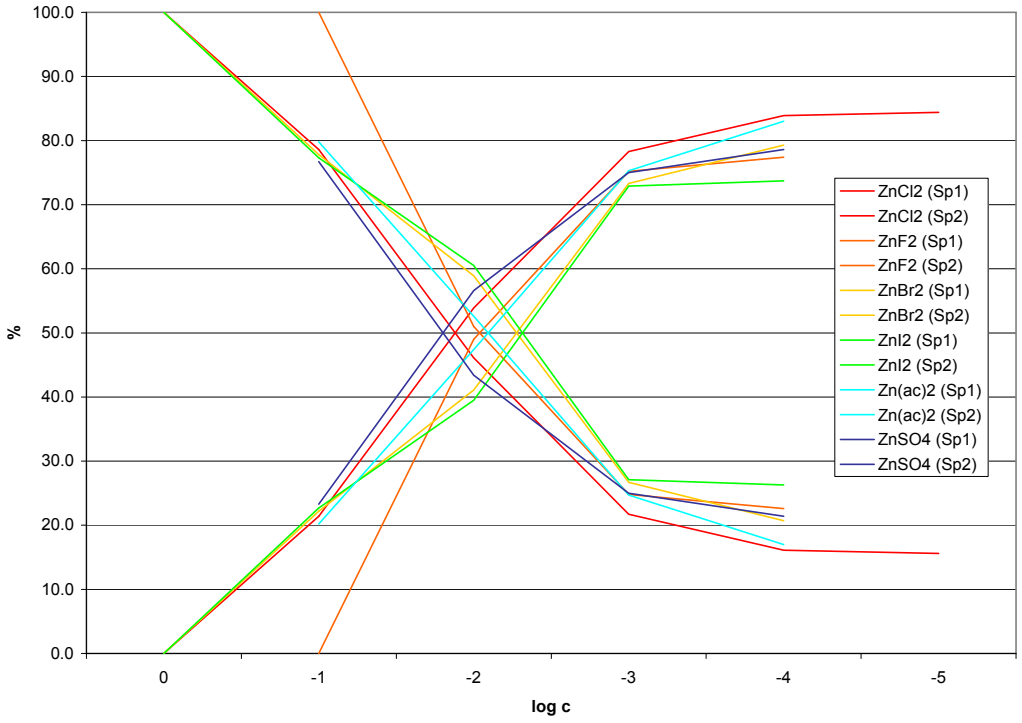

Figure 4.11.: Relative amounts of species 1 and 2 depending on zinc salt concentration for N1. Ascending graphs: Species 1 (Sp1), descending graphs: Species 2 (Sp2). Error bars have been omitted for the purpose of clarity but can be found in the example diagram (Figure 4.10).

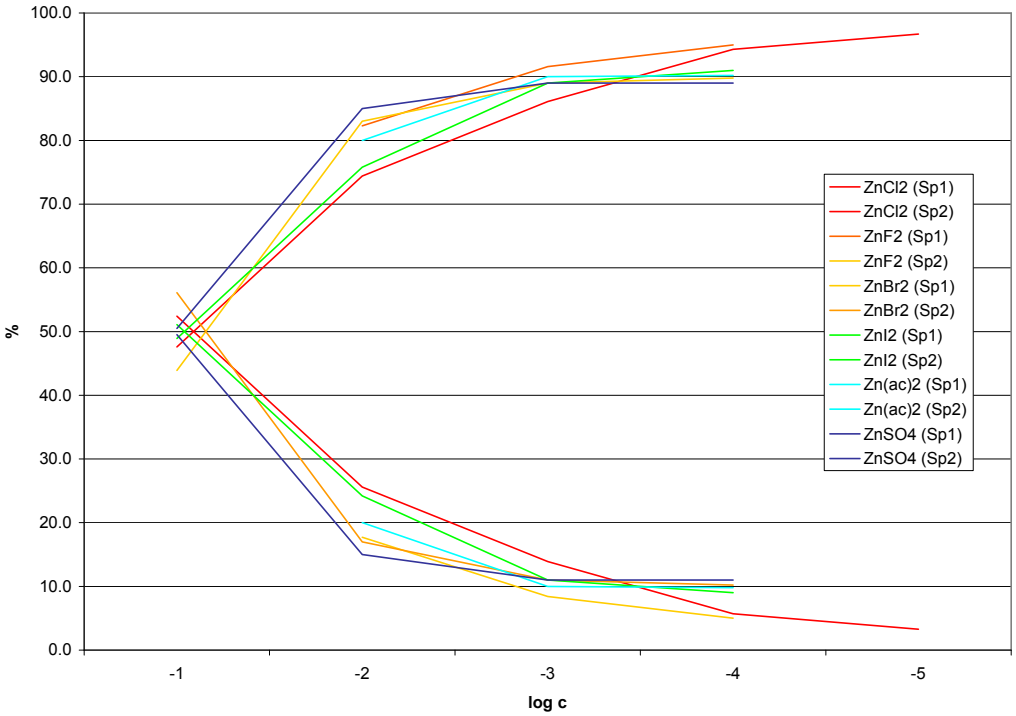

Figure 4.12.: Relative amounts of species 1 and 2 depending on zinc salt concentration for N2. Ascending graphs: Species 1 (Sp1); descending graphs: Species 2 (Sp2). Error bars have been omitted for the purpose of clarity.

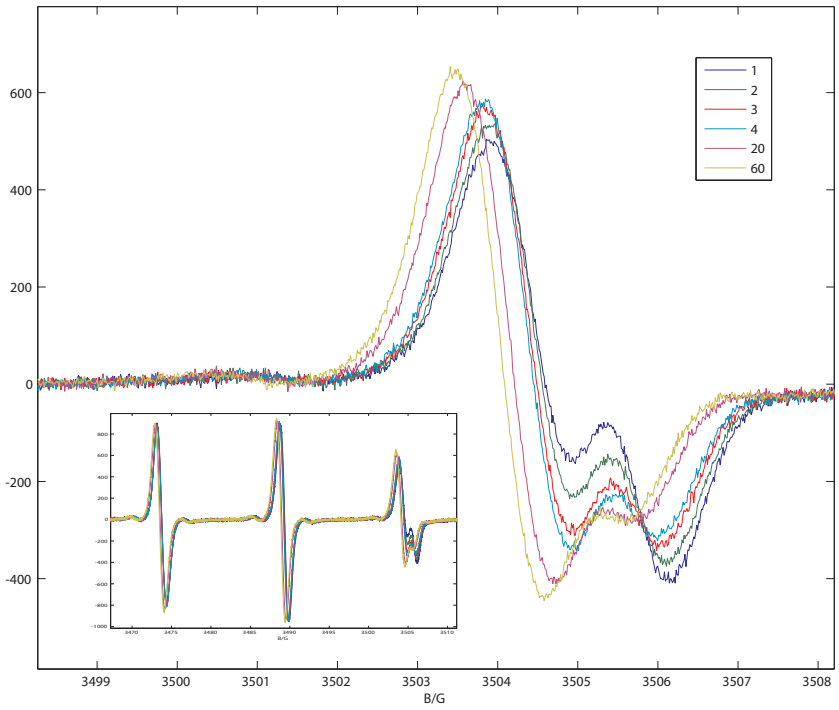

Figure 4.13.: Timescan for N1 in presence of $ZnCl_2$. Legend: scan numbers, delay time after each scan: 5 min.

The reason for waiting with measurements after the sample preparation (Section 3.3.1) was the fact that for both nitroxides some kind of kinetic was noticed in the presence of zinc halides, best observable at a concentration of 100 mM (except for the fluoride, due to its too low solubility product). Figure 4.13 shows the effect exemplified by $ZnCl_2$. The

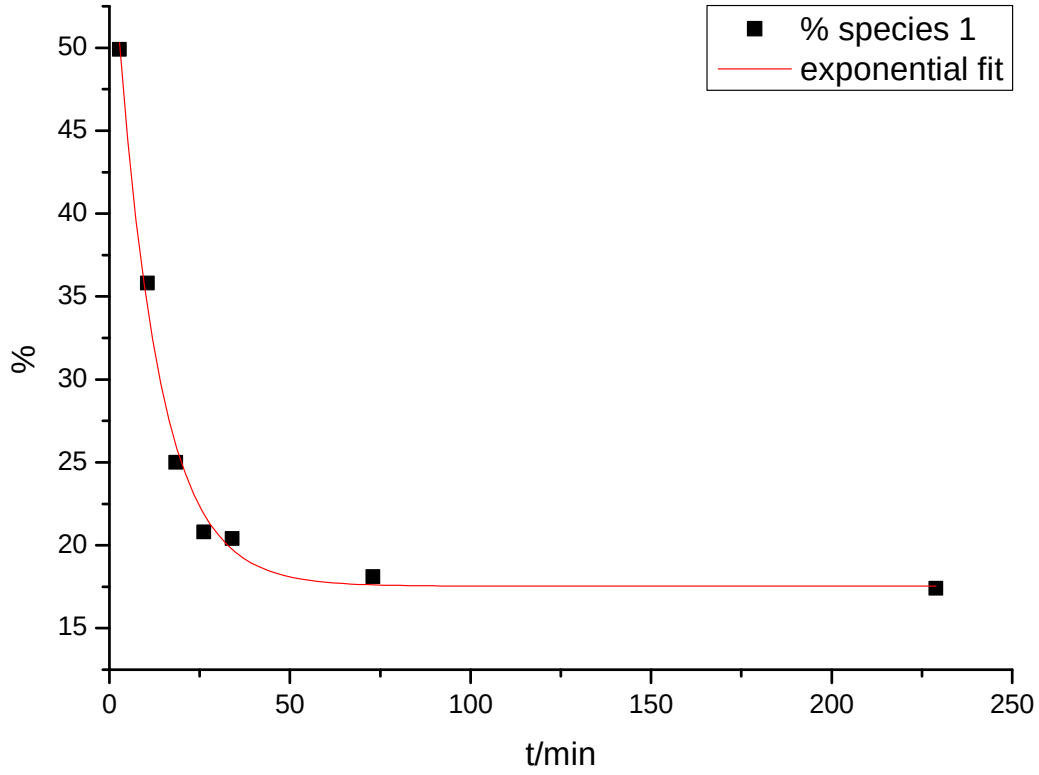

Figure 4.14.: % Species 1 vs time for N1 in presence of $ZnCl_2$. Squares: % species 1 (from WinSIM2002 simulations), line: exponential fit.

first scan (dark blue) was run directly after preparing the sample and placing it into the resonator, a few minutes after the nitroxide and the salt were mixed (time needed for sample handling). A total of 60 scans were recorded, with a delay time of five minutes after each scan. As can be seen in Figures 4.13 and 4.14, the amount of species 2 increases until an equilibrium ratio between species 1 and 2 is reached. The spectra of scans 1–5, 10, and 30 were simulated with WinSIM2002 to determine their respective composition in percentages of species 1 and 2. Figure 4.14 shows a fit of the extracted data to the equation:

$$y = y0 + A \cdot e^{R0 \cdot x} \tag{4.4}$$

The results are summarized in Table 4.6. One possible explanation for this time dependent behavior is the formation of a complex. What speaks for this assumption is the work of Yamamoto and coworkers who described similar complexes of zinc(II) with imino nitroxide

Table 4.6.: Results of the exponential fit (Equation 4.4) for the time-dependent behavior exhibited by N1 in presence of $ZnCl_2$.

y0		**A**		**R0**	
value	error	value	error	value	error
17.54	0.77	41.7	1.9	-0,0864	0,0079

ligands. Figure 4.15 shows the 1:1 ($[ZnCl_2(IMmepy)]$)[101] and 1:2 ($[ZnCl_2(IM2py)_2]$)[100] complex. Crystallization experiments and subsequent X-ray diffraction measurements would be interesing to perform in order to further clarify this behavior.

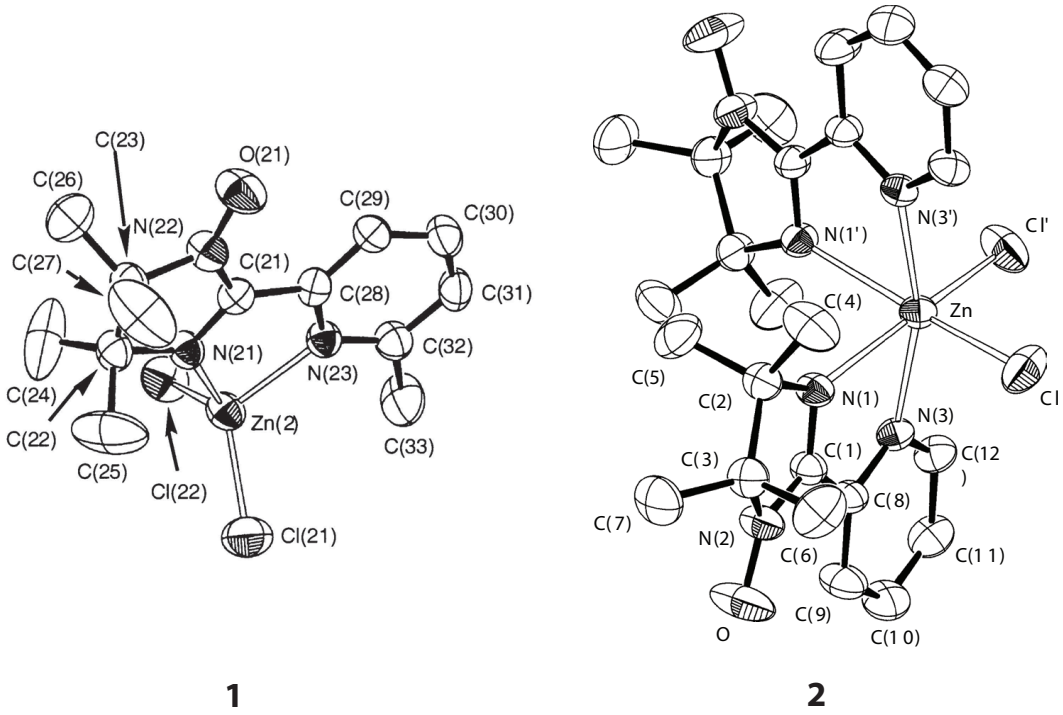

Figure 4.15.: Perspective drawings of $[ZnCl_2(IMmepy)]$ (**1**) and $[ZnCl_2(IM2py)_2]$ (**2**). Hydrogen atoms omitted for clarity, thermal elipsoids drawn at 50 % probability level. Pictures by Yamamoto *et al.*[100,101]

5. Summary and Conclusions

The influence of different metal ions on the CW EPR spectra of pH-sensitive nitroxides was investigated on the example of the two imidazoline nitroxides N1 and N2. Among the screened metal ions, the zinc cation distinctly stood out. Its presence significantly altered the spectrum already at low concentrations, similar to the spectral changes detected upon lowering the pH of the solution. The same observation was made for very high concentrations of calcium ions, although to a much lower extent. The effect was attributed to the metal ions acting as Lewis acids. The cation coordinates to the N-3 ring nitrogen of the nitroxides, thus detracting spin density from the >NO· moiety, which results in a lower a_N value and a slightly increased g factor. This assumption is supported by WinSIM2002 simulations of the spectra as the superimposed spectra of two species (coordinated and uncoordinated). a_N values plotted against - log c give a sigmoidal curve, comparable to a pH titration curve obtained by the Henderson-Hasselbalch equation, with the turning point approximately at - log c = 1–2 for the zinc salts. Generally, equilibrium constants for the coordinated species of N1 were slightly higher than for those of N2, as a comparison of their pK_a values already suggests. This may be led back to the basicity enhancing $+I$ effect of the cyclohexyl side group of N1.

The remarkable differences between the investigated metal cations were attributed to their different charge densities, Lewis acidity parameters, and sizes. Due to the complexity of the interplay between cations, anions, radicals, and water molecules, systematic tendencies for the individual counterions could not be identified. Although, higher precision experiments may help gain further insight into this matter. Additionally, it would be interesting to repeat the measurements in a range of different media to identify the role of the solvent.

Furthermore, the relative concentrations of the coordinated species exhibited an initial time dependency, which may suggest the formation of a complex. However, further investigations, i.e. in the form of crystallization experiments and X-ray structure determination, would be needed to verify this assumption.

In summary, it can be said that the presence of metal ions can remarkably affect the EPR spectral profile of imidazoline nitroxides, which should be taken into consideration when using them, for example, as spin probes in pH studies. Even though they seem to exhibit a comparably small effect, this can be equally important for alkali and alkaline

earth metal ions, due to their abundance in natural fluids and biological samples. And, of course, interactions between nitroxide radicals and metal ions are not merely a potential interference factor for pH measurements, but probably also a basis for the development of new specific metal ion probes.

Bibliography

[1] Piloty, O.; Schwerin, B. G. *Ber. Dtsch. chem. Ges.* **1901**, *34*, 1870–87.

[2] Holden, A. N.; Yager, W. A.; Merritt, F. R. *J. Chem. Phys.* **1951**, *19*, 1319.

[3] Gerson, F.; Huber, W. *Electron Spin Resonance Spectroscopy of Organic Radicals*; Wiley-VCH, 2003.

[4] *Electron Paramagnetic Resonance: A Practitioner's Toolkit*; Brustolon, M., Giamello, E., Eds.; Wiley, 2009.

[5] Likhtenshtein, G. I.; Yamauchi, J.; Nakatsuji, S.; Smirnov, A. I.; Tamura, R. *Nitroxides: Applications in Chemistry, Biomedicine, and Materials Science*; Wiley-VCH, 2008.

[6] Freed, J. H. Theory of slow tumbling ESR spectra for nitroxides. *Spin Labeling*, 1976; pp 53–132.

[7] Zerbetto, M.; Polimeno, A.; Barone, V. *Computer Physics Communications* **2009**, *180*, 2680 – 2697.

[8] Hoffmann, A. K.; Henderson, A. T. *J. Am. Chem. Soc.* **1961**, *83*, 4671.

[9] Neiman, M. B.; Rozantsev, E. G.; Mamedova, Y. G. *Nature (London, U. K.)* **1962**, *196*, 472–4.

[10] Volodarskii, L. B.; Grigor'ev, I. A.; Sagdeev, R. Z. *Biol. Magn. Reson.* **1980**, *2*, 169–241.

[11] Keana, J. F. W.; Acarregui, M. J.; Boyle, S. L. M. *J. Am. Chem. Soc.* **1982**, *104*, 827–30.

[12] Khramtsov, V. V.; Veiner, L. M.; Grigor'ev, I. A.; Volodarskii, L. B. *Chem. Phys. Lett.* **1982**, *91*, 69–72.

[13] Altenbach, C.; Marti, T.; Khorana, H. G.; Hubbell, W. L. *Science (Washington, D. C., 1883-)* **1990**, *248*, 1088–92.

[14] Hubbell, W. L.; Altenbach, C. *Curr. Opin. Struct. Biol.* **1994**, *4*, 566–73.

[15] Voss, J.; Salwinski, L.; Kaback, H. R.; Hubbell, W. L. *Proc. Natl. Acad. Sci. U. S. A.* **1995**, *92*, 12295–9.

[16] Jones, R.; Dwek, R. A.; Walker, I. O. *Eur. J. Biochem.* **1973**, *34*, 28–40.

[17] Chao, Y. Y. H.; Holtzer, A.; Mastin, S. H. *J. Am. Chem. Soc.* **1977**, *99*, 8024–32.

[18] Volkov, A.; Dockter, C.; Bund, T.; Paulsen, H.; Jeschke, G. *Biophys. J.* **2009**, *96*, 1124–1141.

[19] Ichikawa, T.; Kevan, L.; Bowman, M. K.; Dikanov, S. A.; Tsvetkov, Y. D. *J. Chem. Phys.* **1979**, *71*, 1167–74.

[20] Venditti, V.; Niccolai, N.; Butcher, S. E. *Nucleic Acids Res.* **2008**, *36*, e20/1–e20/10.

[21] Niccolai, N.; Spiga, O.; Bernini, A.; Scarselli, M.; Ciutti, A.; Fiaschi, I.; Chiellini, S.; Molinari, H.; Temussi, P. A. *J. Mol. Biol.* **2003**, *332*, 437–447.

[22] Venditti, V.; Bernini, A.; De Simone, A.; Spiga, O.; Prischi, F.; Niccolai, N. *Biochem. Biophys. Res. Commun.* **2007**, *356*, 114–117.

[23] Niccolai, N.; Ciutti, A.; Spiga, O.; Scarselli, M.; Bernini, A.; Bracci, L.; Di Maro, D.; Dalvit, C.; Molinari, H.; Esposito, G.; Temussi, P. A. *J. Biol. Chem.* **2001**, *276*, 42455–42461.

[24] Teng, C.-L.; Bryant, R. G. *J. Magn. Reson.* **2006**, *179*, 199–205.

[25] Zhou, N.; Mascagni, P.; Gibbons, W. A.; Niccolai, N.; Rossi, C.; Wyssbrod, H. *J. Chem. Soc., Perkin Trans. 2* **1985**, 581–7.

[26] Pintacuda, G.; Otting, G. *J. Am. Chem. Soc.* **2002**, *124*, 372–373.

[27] Bernini, A.; Spiga, O.; Venditti, V.; Prischi, F.; Bracci, L.; Tong, A. P.-L.; Wong, W.-T.; Niccolai, N. *J. Am. Chem. Soc.* **2006**, *128*, 9290–9291.

[28] Teng, C.-L.; Bryant, R. G. *Biophys. J.* **2004**, *86*, 1713–1725.

[29] Lebedeva, N.; Ranganathan, R.; Bales, B. L. *J. Phys. Chem. B* **2007**, *111*, 5781–5793.

[30] Lebedeva, N.; Bales, B. L. *J. Phys. Chem. B* **2006**, *110*, 9791–9799.

[31] Nakagawa, K. *Langmuir* **2003**, *19*, 5078–5082.

[32] Szajdzinska-Pietek, E.; Sulak, K.; Dragutan, I.; Schlick, S. *J. Colloid Interface Sci.* **2007**, *312*, 405–412.

[33] Gambi, C. M. C.; Giordano, R.; Chittofrati, A.; Pieri, R.; Baglioni, P.; Teixeira, J. *Appl. Phys. A: Mater. Sci. Process.* **2002**, *74*, S436–S438.

[34] Gambi, C. M. C.; Giordano, R.; Chittofrati, A.; Pieri, R.; Baglioni, P.; Teixeira, J. *J. Phys. Chem. A* **2003**, *107*, 11558–11564.

[35] Gambi, C. M. C.; Giordano, R.; Chittofrati, A.; Pieri, R.; Baglioni, P.; Teixeira, J. *J. Phys. Chem. B* **2005**, *109*, 8592–8598.

[36] Aliaga, C.; Juarez-Ruiz, J. M.; Scaiano, J. C.; Aspee, A. *Org. Lett.* **2008**, *10*, 2147–2150.

[37] Trubitsin, B. V.; Tikhonov, A. N. *J. Magn. Reson.* **2003**, *163*, 257–269.

[38] Ruban, L. V.; Buchachenko, A. L.; Neiman, M. B.; Kokhanov, Y. V. *Vysokomol. Soedin.* **1966**, *8*, 1642–6.

[39] Greszta, D.; Matyjaszewski, K. *Macromolecules* **1996**, *29*, 7661–7670.

[40] Fischer, H.; Souaille, M. *Chimia* **2001**, *55*, 109–113.

[41] Guillaneuf, Y.; Gigmes, D.; Marque, S. R. A.; Astolfi, P.; Greci, L.; Tordo, P.; Bertin, D. *Macromolecules (Washington, DC, U. S.)* **2007**, *40*, 3108–3114.

[42] Hodgson, J. L.; Coote, M. L. *Macromolecules (Washington, DC, U. S.)* **2010**, *43*, 4573–4583.

[43] Kocherginsky, N. M.; Kostetski, Y. Y.; Smirnov, A. I. *J. Agric. Food Chem.* **2005**, *53*, 6870–6876.

[44] Hosokawa, K.; Chen, P.; Lavin, F. M.; Bottle, E. S. *Free Radical Biol. Med.* **2004**, *37*, 946–952.

[45] Brasch, R. C. *Radiology (Easton, Pa.)* **1983**, *147*, 781–8.

[46] Sosnovsky, G.; Rao, N. U. M.; Li, S. W.; Swartz, H. M. *J. Org. Chem.* **1989**, *54*, 3667–74.

[47] Chen, K.; Swartz, H. M. *Biochim. Biophys. Acta, Mol. Cell Res.* **1988**, *970*, 270–7.

[48] Yelinova, V.; Krainev, A.; Savelov, A.; Grigor'ev, I. *J. Chem. Soc., Perkin Trans. 2* **1993**, 2053–5.

[49] Lauffer, R. B. *Chem. Rev.* **1987**, *87*, 901–27.

[50] Rosen, G. M.; Halpern, H. J.; Brunsting, L. A.; Spencer, D. P.; Strauss, K. E.; Bowman, M. K.; Wechsler, A. S. *Proc. Natl. Acad. Sci. U. S. A.* **1988**, *85*, 7772–6.

[51] Plonka, P. M. *Exp. Dermatol.* **2009**, *18*, 472–484.

[52] Strehmel, V.; Laschewsky, A.; Stoesser, R.; Zehl, A.; Herrmann, W. *J. Phys. Org. Chem.* **2006**, *19*, 318–325.

[53] Strehmel, V.; Rexhausen, H.; Strauch, P. *Tetrahedron Lett.* **2008**, *49*, 3264–3267.

[54] Dzuba, S. A. *Spectrochim. Acta, Part A* **2000**, *56A*, 227–234.

[55] Paola, F.; Marco, L.; Pamela, P.; Franco, P. G. *Chemphyschem* **2002**, *3*, 789–93.

[56] Hinderberger, D.; Spiess, H. W.; Jeschke, G. *Appl. Magn. Reson.* **2009**, *37*, 657–683.

[57] Khramtsov, V. V.; Veiner, L. M. *Imidazoline Nitroxides* **1988a**, *2*, 37–80.

[58] Khramtsov, V. V.; Volodarsky, L. B. *Biol. Magn. Reson.* **1998**, *14*, 109–180.

[59] Helbert, J. N.; Kopf, P. W.; Poindexter, E. H.; Wagner, B. E. *J. Chem. Soc., Dalton Trans.* **1975**, 998–1006.

[60] Ullman, E. F.; Call, L.; Osiecki, J. H. *J. Org. Chem.* **1970**, *35*, 3623–31.

[61] Voinov, M. A.; Ruuge, A.; Reznikov, V. A.; Grigor'ev, I. A.; Smirnov, A. I. *Biochemistry* **2008**, *47*, 5626–5637.

[62] Weiner, L. M. *Appl. Magn. Reson.* **2007**, *31*, 357–373.

[63] Khramtsov, V. V.; Veiner, L. M.; Eremenko, S. I.; Bel'chenko, O. I.; Schastnev, P. V.; Grigor'ev, I. A.; Reznikov, V. A. *J. Magn. Reson.* **1985**, *61*, 397–408.

[64] Kirilyuk, I. A.; Bobko, A. A.; Grigor'ev, I. A.; Khramtsov, V. V. *Org. Biomol. Chem.* **2004**, *2*, 1025–1030.

[65] Kroll, C.; Schwarz, K.-H.; Surmann, P.; Borchert, H.-H. *Bioelectrochem. Bioenerg.* **1999**, *48*, 233–236.

[66] Improta, R.; Scalmani, G.; Barone, V. *Chem. Phys. Lett.* **2001**, *336*, 349–356.

[67] Improta, R.; Di Matteo, A.; Barone, V. *Theor. Chem. Acc.* **2000**, *104*, 273–279.

[68] Barone, V.; Bencini, A.; di Matteo, A. *J. Am. Chem. Soc.* **1997**, *119*, 10831–10837.

[69] Barone, V. *Chem. Phys. Lett.* **1996**, *262*, 201–206.

[70] di Matteo, A.; Adamo, C.; Cossi, M.; Barone, V.; Rey, P. *Chem. Phys. Lett.* **1999**, *310*, 159–165.

[71] Ikryannikova, L. N.; Ustynyuk, L. Y.; Tikhonov, A. N. *J. Phys. Chem. A* **2004**, *108*, 4759–4768.

[72] Khramtsov, V. V.; Yelinova, V. I.; Weiner, L. M.; Berezina, T. A.; Martin, V. V.; Volodarsky, L. B. *Anal. Biochem.* **1989**, *182*, 58–63.

[73] Weiner, L. M.; Hu, H.; Swartz, H. M. *FEBS Lett.* **1991**, *290*, 243–6.

[74] Pinkus, R.; Weiner, L. M.; Daniel, V. *Biochemistry* **1995**, *34*, 81–8.

[75] Pinkus, R.; Weiner, L. M.; Daniel, V. *J. Biol. Chem.* **1996**, *271*, 13422–13429.

[76] Hirsch, K.; Danilenko, M.; Giat, J.; Miron, T.; Rabinkov, A.; Wilchek, M.; Mirelman, D.; Levy, J.; Sharoni, Y. *Nutr. Cancer* **2000**, *38*, 245–254.

[77] Nohl, H.; Stolze, K.; Weiner, L. M. *Methods Enzymol.* **1995**, *251*, 191–203.

[78] Weiner, L. M. *Methods Enzymol.* **1995**, *251*, 87–105.

[79] Peretz, M.; Weiner, L. M.; Burstein, Y. *Protein Sci.* **1997**, *6*, 1074–1083.

[80] Berliner, L. J.; Grunwald, J.; Hankovszky, H. O.; Hideg, K. *Anal. Biochem.* **1982**, *119*, 450–5.

[81] Balakirev, M.; Khramtsov, V. *J. Chem. Soc., Perkin Trans. 2* **1993**, 2157–60.

[82] Khramtsov, V. V.; Marsh, D.; Weiner, L.; Reznikov, V. A. *Biochim. Biophys. Acta, Biomembr.* **1992**, *1104*, 317–24.

[83] Voinov, M. A.; Kirilyuk, I. A.; Smirnov, A. I. *J. Phys. Chem. B* **2009**, *113*, 3453–3460.

[84] Tikhonov, A. N.; Agafonov, R. V.; Grigor'ev, I. A.; Kirilyuk, I. A.; Ptushenko, V. V.; Trubitsin, B. V. *Biochim. Biophys. Acta, Bioenerg.* **2008**, *1777*, 285–294.

[85] Nesbitt, D. M.; Berg, S. P. *Biochim. Biophys. Acta, Bioenerg.* **1980**, *593*, 353–61.

[86] Nesbitt, D. M.; Berg, S. P. *Biochim. Biophys. Acta, Bioenerg.* **1982**, *679*, 169–74.

[87] Molochnikov, L. S.; Kovalyova, E. G.; Grigor'ev, I. A.; Zagorodni, A. A. *J. Phys. Chem. B* **2004**, *108*, 1302–1313.

[88] Kroll, C.; Maeder, K.; Stoesser, R.; Borchert, H. H. *Eur. J. Pharm. Sci.* **1995**, *3*, 21–6.

[89] Capancioni, S.; Schwach-Abdellaoui, K.; Kloeti, W.; Herrmann, W.; Brosig, H.; Borchert, H.-H.; Heller, J.; Gurny, R. *Macromolecules* **2003**, *36*, 6135–6141.

[90] Maeder, K.; Gallez, B.; Liu, K. J.; Swartz, H. M. *Biomaterials* **1996**, *17*, 457–61.

[91] You, C.-C.; De, M.; Han, G.; Rotello, V. M. *J. Am. Chem. Soc.* **2005**, *127*, 12873–12881.

[92] McIntosh, C. M.; Esposito, I., Edward A.; Boal, A. K.; Simard, J. M.; Martin, C. T.; Rotello, V. M. *J. Am. Chem. Soc.* **2001**, *123*, 7626–7629.

[93] Khlestkin, V. K.; Polienko, J. F.; Voinov, M. A.; Smirnov, A. I.; Chechik, V. *Langmuir* **2008**, *24*, 609–612.

[94] Kirilyuk, I. A.; Bobko, A. A.; Khramtsov, V. V.; Grigor'ev, I. A. *Org. Biomol. Chem.* **2005**, *3*, 1269–1274.

[95] Stoll, S. *EasySpin*. `http://www.easyspin.org/`.

[96] *Public EPR Software Tools*. `http://www.niehs.nih.gov/research/resources/software/tools/`.

[97] Eaton, G. R. *Inorg. Nucl. Chem. Lett.* **1972**, *8*, 647–52.

[98] Karayannis, N. M.; Paleos, C. M.; Mikulski, C. M.; Pytlewski, L. L.; Blum, H.; Labes, M. M. *Inorg. Chim. Acta* **1973**, *7*, 74–8.

[99] Boymel, P. M.; Chang, J. R.; DuBois, D. L.; Greenslade, D. J.; Eaton, G. R.; Eaton, S. S. *J. Am. Chem. Soc.* **1977**, *99*, 5500–2.

[100] Yamamoto, Y.; Suzuki, T.; Kaizaki, S. *J. Chem. Soc., Dalton Trans.* **2001**, 1566–1572.

[101] Yamamoto, Y.; Suzuki, T.; Kaizaki, S. *J. Chem. Soc., Dalton Trans.* **2001**, 2943–2950.

[102] Wagner, B. E.; Helbert, J. N.; Bates, J., Richard D.; Poindexter, E. H. *J. Chem. Soc., Chem. Commun.* **1973**, 748–9.

[103] Stone, E. W.; Maki, A. H. *J. Chem. Phys.* **1963**, *39*, 1635–12.

[104] Wagner, B. E.; Linowski, J. W.; Potenza, J. A.; Bates, J., R. D.; Helbert, J. N.; Poindexter, E. H. *J. Am. Chem. Soc.* **1976**, *98*, 4405–9.

[105] Kolodziejski, W. *J. Mol. Struct.* **1987**, *159*, 335–43.

[106] Zolotov, Y. A.; Petrukhin, O. M.; Nad, V. Y.; Volodarskii, L. B. *Anal. Chim. Acta* **1980**, *115*, 1–23.

[107] Hoffman, B. M.; Eames, T. B. *J. Amer. Chem. Soc.* **1969**, *91*, 5168–70.

[108] Lunina, E. V.; Markaryan, G. L.; Parenago, O. O.; Fionov, A. V. *Colloids Surf., A* **1993**, *72*, 333–43.

[109] Taylor, J. S.; Leigh, J., John S.; Cohn, M. *Proc. Nat. Acad. Sci. U. S.* **1969**, *64*, 219–26.

[110] Leigh, J., J. S. *J. Chem. Phys.* **1970**, *52*, 2608–12.

[111] Yager, T. D.; Eaton, G. R.; Eaton, S. S. *J. Chem. Soc., Chem. Commun.* **1978**, 944–5.

[112] Yager, T. D.; Eaton, G. R.; Eaton, S. S. *Inorg. Chem.* **1979**, *18*, 725–7.

[113] Eaton, S. S.; Eaton, G. R. *Coord. Chem. Rev.* **1978**, *26*, 207–62.

[114] Eaton, S. S.; Eaton, G. R. *Coord. Chem. Rev.* **1988**, *83*, 29–72.

[115] Voinov, M. A.; Polienko, J. F.; Schanding, T.; Bobko, A. A.; Khramtsov, V. V.; Gatilov, Y. V.; Rybalova, T. V.; Smirnov, A. I.; Grigor'ev, I. A. *J. Org. Chem.* **2005**, *70*, 9702–9711.

[116] Marcus, Y. *Ion Properties*; Marcel Dekker, Inc., 1997.

[117] Marcus, Y. *Thermochim. Acta* **1986**, *104*, 389–94.

Supplementary Material

A. Symbols and Abbreviations

Symbols

α	electron spin quantum number $m_S = 1/2$
α	angle
α_+	Lewis acidity parameter
β	electron spin quantum number $m_S = -1/2$
β_-	Lewis basicity parameter
ΔB	linewidth
$\Delta B_{1/2}$	half height linewidth
ΔB_{pp}	peak-to-peak linewidth
Θ	dihedral angle
η	viscosity
γ	gyromagnetic ratio
γ_e	gyromagnetic ratio of the free electron
μ_B	Bohr magneton
$\boldsymbol{\mu_e}$	magnetic moment of the electron
$\mu_{e,z}$	z component of the magnetic moment of the electron
$\boldsymbol{\mu_N}$	nuclear magnetic moment
μ_N	nuclear magneton
$\mu_{N,z}$	z component of the nuclear magnetic moment
ν	frequency
Π	water accessibility parameter
ρ_S	spin density
τ, τ_C	life time, correlation time
ω	(angular) frequency
ω_L	larmor frequency
a	hyperfine coupling constant
B	magnetic induction
E	energy
e	charge of one electron
g	g factor
g_e	g factor of the free electron
g_{iso}	average of g tensor
g_N	nuclear g factor
h	Planck's constant
$\hbar$	Planck's constant divided by 2π
$\boldsymbol{I}$	nuclear spin angular momentum
I	nuclear spin quantum number

$\boldsymbol{J}$	total angular momentum
K	equilibrium constant
k	Boltzmann constant
k	rate constant
$\boldsymbol{M}$	(macroscopic) magnetization vector
M	(macroscopic) magnetization (M_0, M_x, M_y, M_z)
m_e	electron mass
m_I	nuclear spin quantum number
m_S	electron spin quantum number
P	transition probability between Zeeman levels
Q	spin polarization parameter
r	(ionic) radius
S	spin quantum number
$\boldsymbol{S}$	spin vector
T	temperature
T_1	spin lattice relaxation time
T_2	spin spin relaxation time
t	time
V_i^∞	standard partial molar volume
x, y, z	Carthesian coordinates
z	ionic charge

Abbreviations

A-T	ataxia telangiectasia
ATI	4-amino-2,5-dihydro-2,2,5,5-tetramethyl-3-imidazoline-1-yloxy
ATP	adenosine triphosphate
CAT-1	4-trimethylammonium iodide TEMPO
CMC	critical micellar concentration
CrOx	chromium oxalate
CW EPR	continuous wave electron paramagnetic resonance
DFT	density functional theory
DNA	deoxyribonucleic acid
DNP	dynamic nuclear polarization
DPP	differential pulse polarography
DPPH	2,2-diphenyl-1-picrylhydrazyl

DSA	(4,4-dimethyl-3-oxazolidinyl)oxy-octadecanoic acid
DSE	(4,4-dimethyl-3-oxazolidinyl)oxy-octadecanoic acid ester
EPR	electron paramagnetic resonance
ESEEM	electron spin echo envelope modulation
FTIR	Fourier transform infrared
GSH	glutathione
HALS	hindered amine light stabilizers
HCO	hydrogenated castor oil
HSA	human serum albumin
HSQC	heteronuclear single quantum coherence
hfcc	hyperfine coupling constant
LHCIIb	light-harvesting complex IIb
MPC	monolayer-protected gold cluster
MRI	magnetic resonance imaging
N1	4-(cyclohexylamino)-2,5-dihydro-2,2,5,5-tetramethyl-3-imidazoline-1-yloxy
N2	4-amino-2,5-dihydro-2,2,5,5-tetramethyl-3-imidazoline-1-yloxy
NiEDDA	nickel(II) ethylenediamine-N,N'-diacetic acid
NIEHS	National Institute of Environmental Health Sciences
NMLP	nitroxide-mediated living polymerization
NMR	nuclear magnetic resonance
PCM	polarizable continuum model
PFPE	perfluoropolyether
PRE	paramagnetic relaxation enhancement
RNA	ribonucleic acid
SANS	small angle neutron scattering
SDS	sodium dodecyl sulfate
SDSL	site-directed spin labeling
SLR	spin lattice relaxation
SNR	stable nitroxyl radical
SOMO	singly occupied molecular orbital
SSR	spin spin relaxation
TEMPO	2,2,6,6-tetramethylpiperidine-1-oxyl
TEMPOL	4-hydroxy-TEMPO
tempamine	4-amino-TEMPO

Supplementary Material

B. Spectra

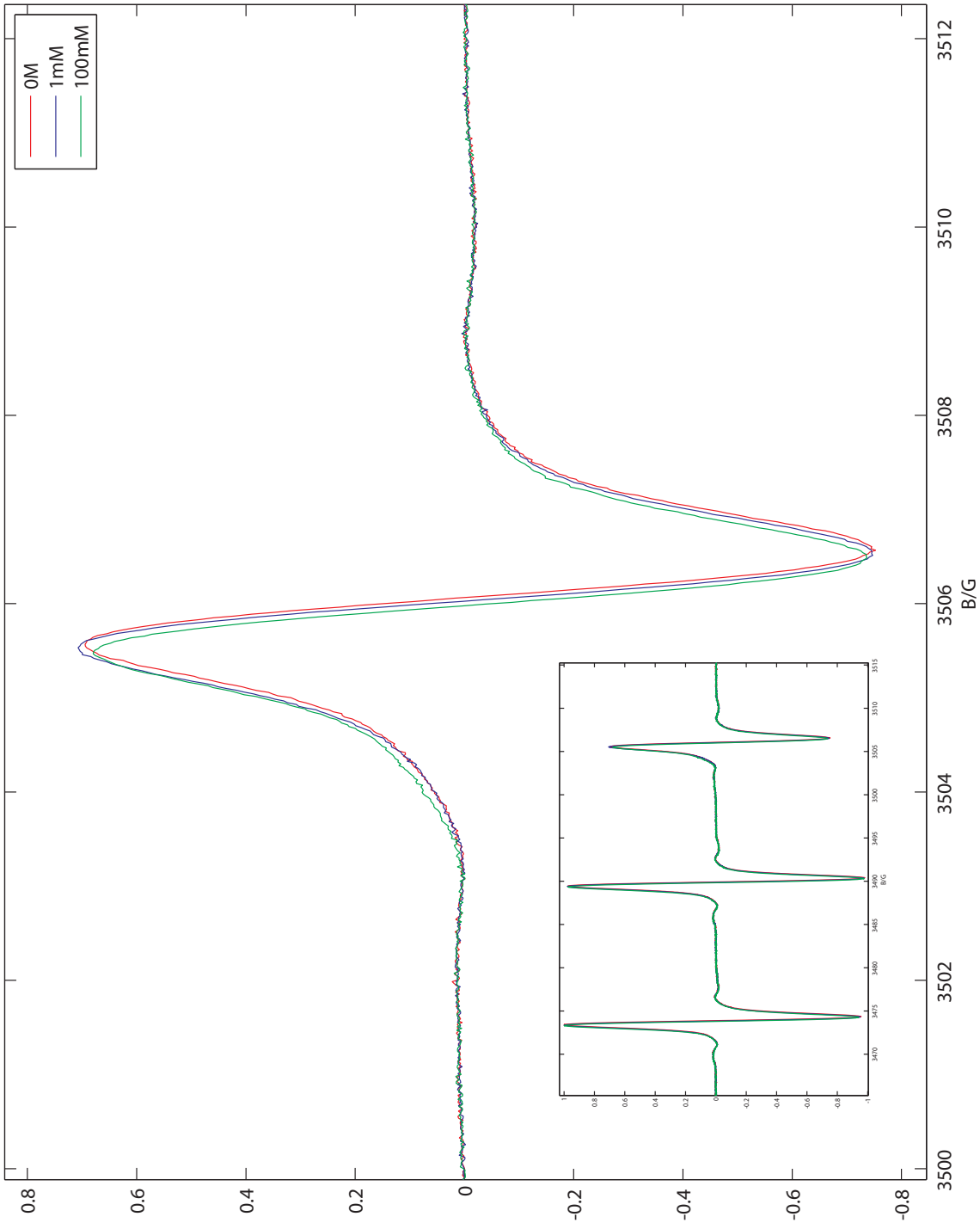

Figure B.1.: High-field peaks and full spectra of N1 with different concentrations of lithium chloride. Red: N1 without added salt, blue: 1 mM LiCl, green: 100 mM LiCl.

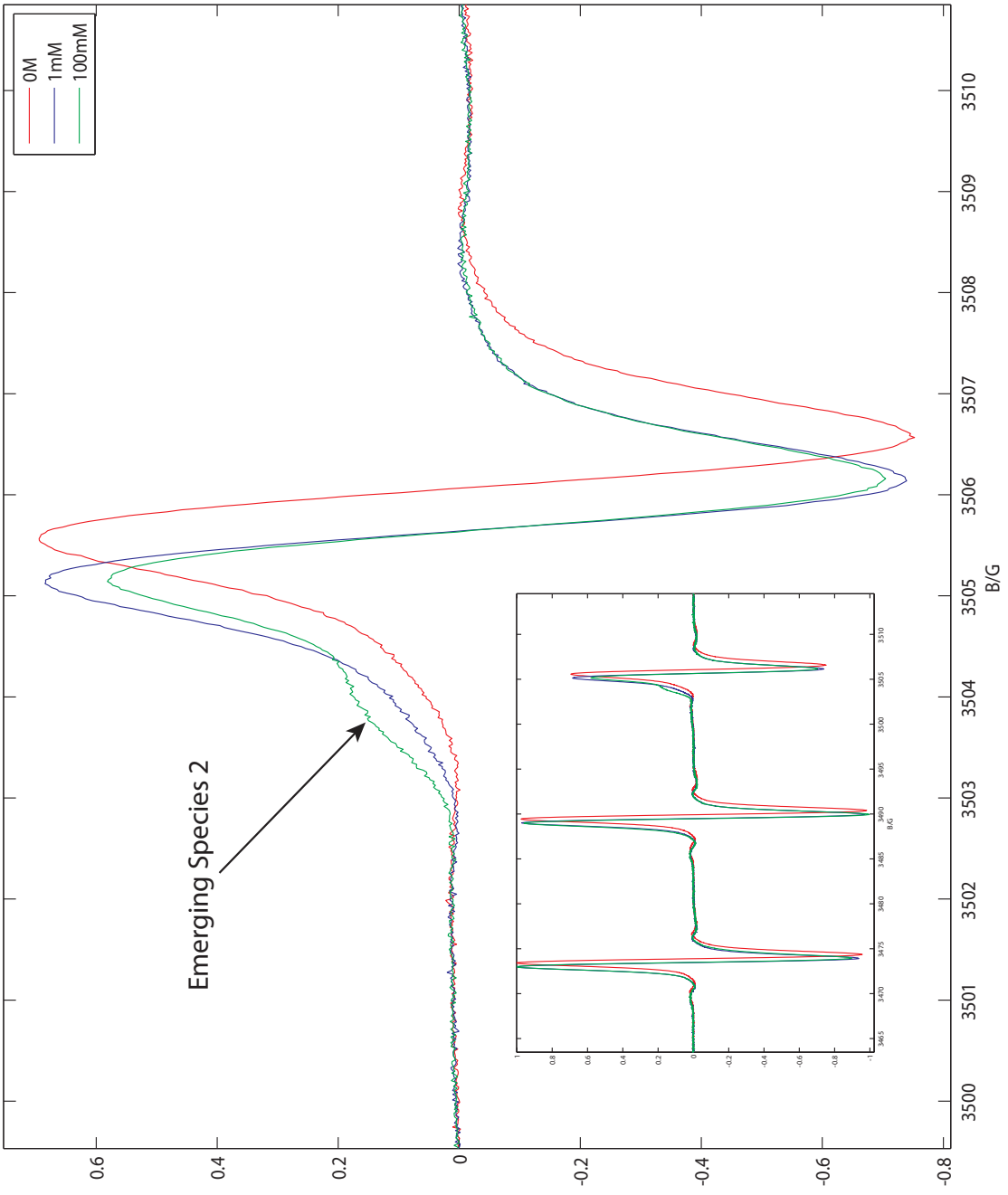

Figure B.2.: High-field peaks and full spectra of N1 with different concentrations of calcium chloride. Red: N1 without added salt, blue: 1 mM $CaCl_2$, green: 100 mM $CaCl_2$.

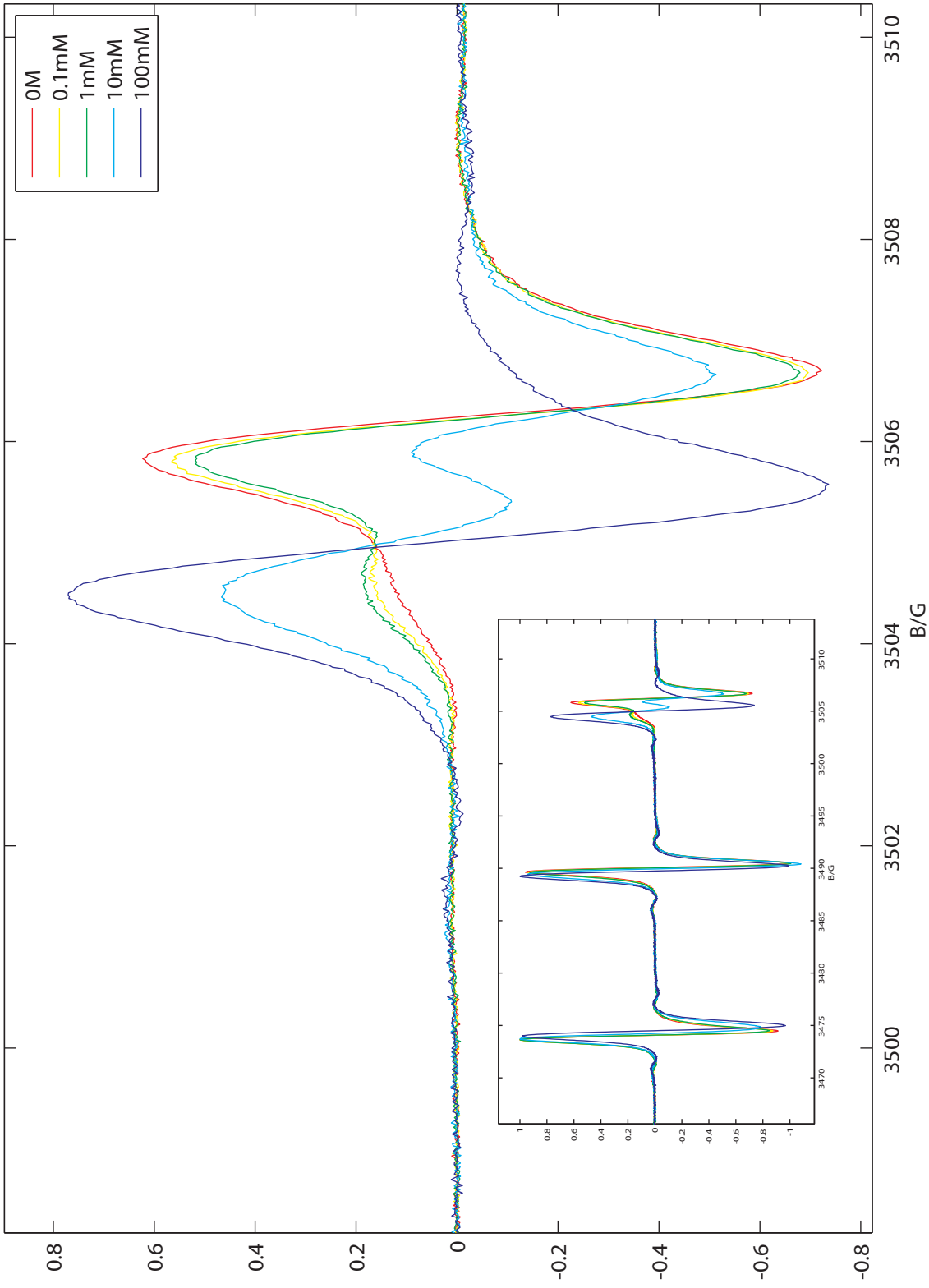

Figure B.3.: High-field peaks and full spectra of N1 with different concentrations of zinc fluoride. Red: N1 without added salt, yellow: 0.1 mM ZnF_2, green: 1 mM ZnF_2, cyan: 10 mM ZnF_2, blue: 100 mM ZnF_2.

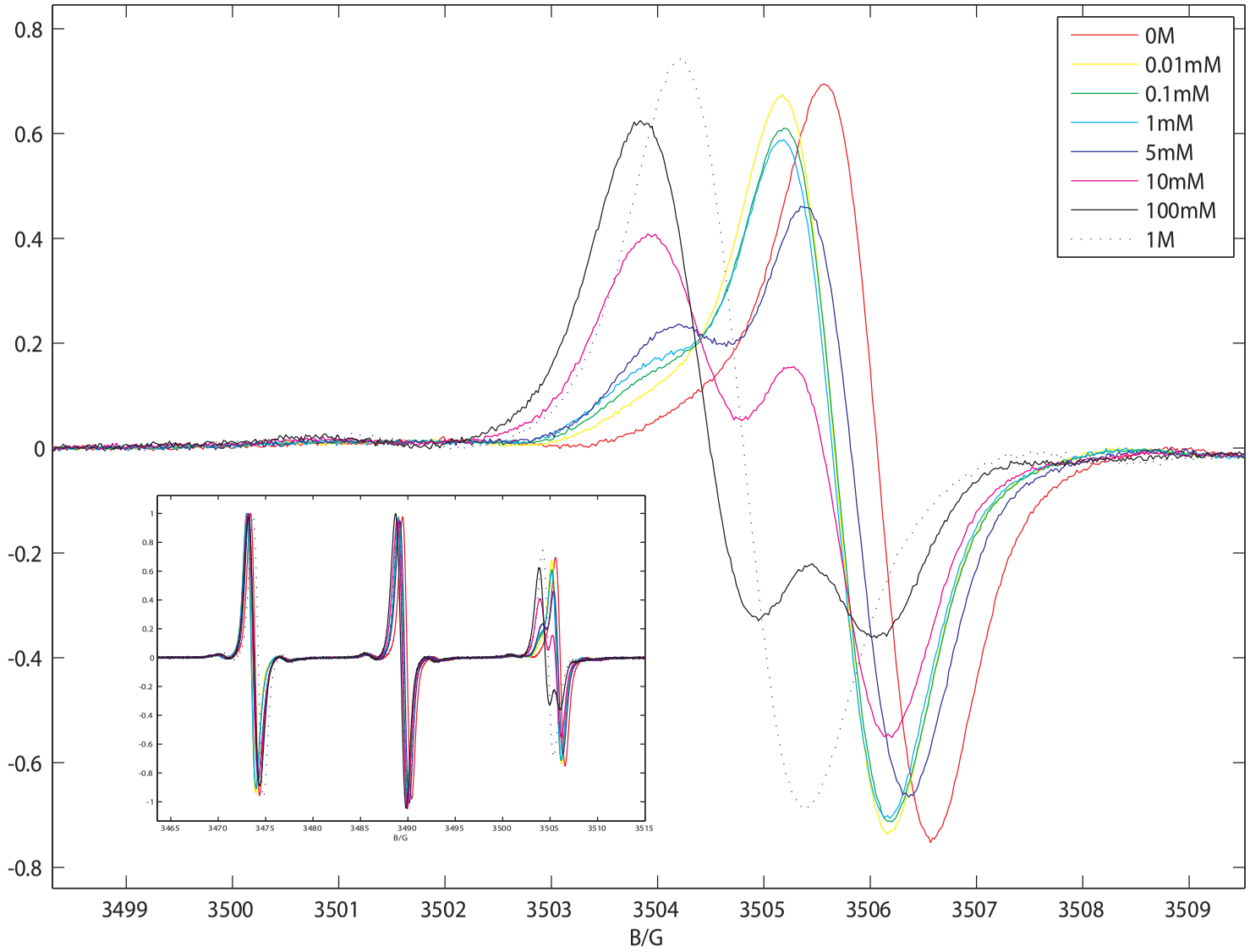

Figure B.4.: High-field peaks and full spectra of N1 with different concentrations of zinc chloride. Red: N1 without added salt, yellow: 0.01 mM $ZnCl_2$, green: 0.1 mM $Zncl_2$, cyan: 1 mM $ZnCl_2$, blue: 5 mM $ZnCl_2$, magenta: 10 mM $ZnCl_2$, black: 100 mM $ZnCl_2$, dotted line: 1 M $ZnCl_2$.

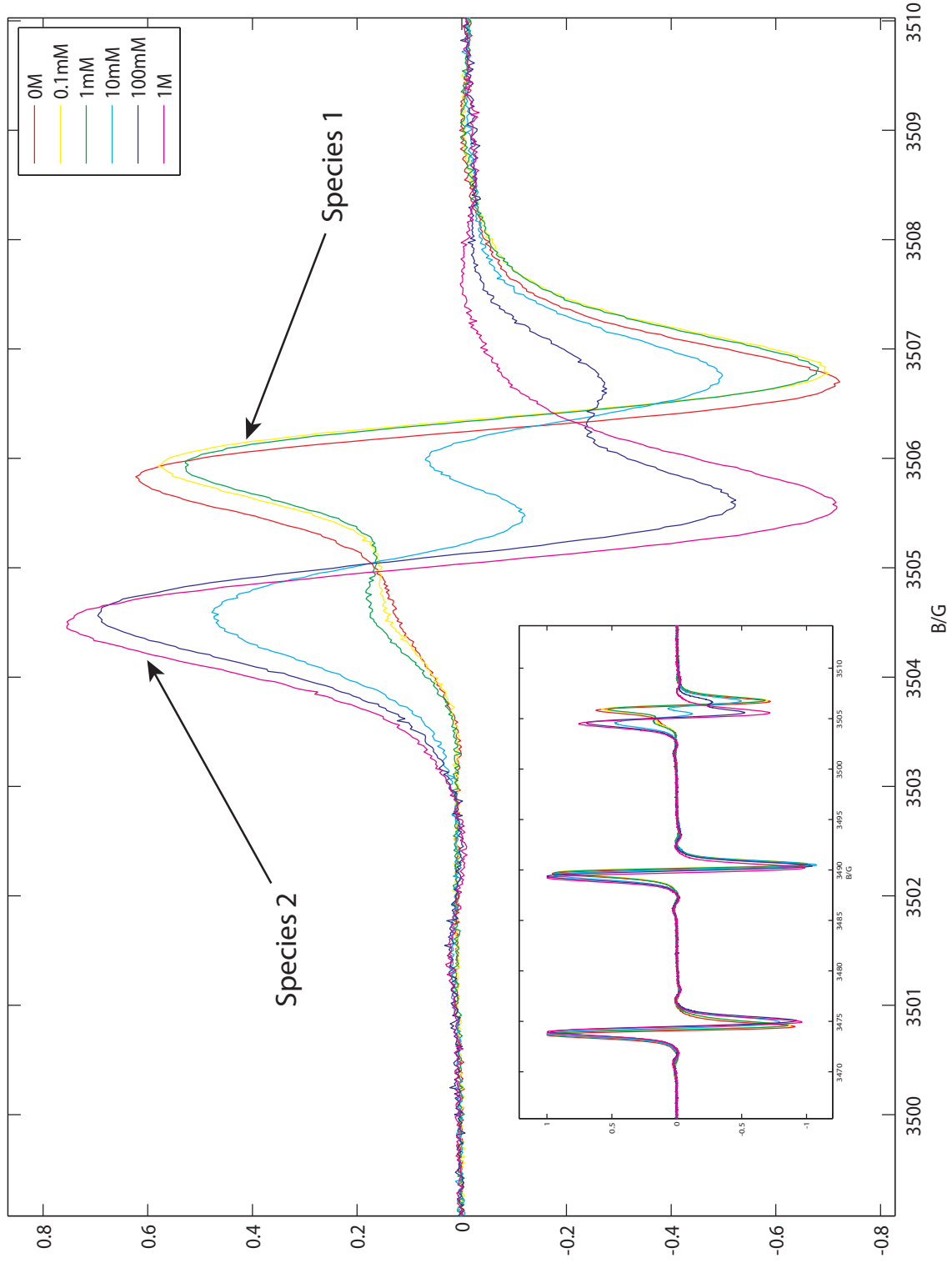

Figure B.5.: High-field peaks and full spectra of N1 with different concentrations of zinc bromide. Red: N1 without added salt, yellow: 0.1 mM $ZnBr_2$, green: 1 mM $ZnBr_2$, cyan: 10 mM $ZnBr_2$, blue: 100 mM $ZnBr_2$, magenta: 1 M $ZnBr_2$.

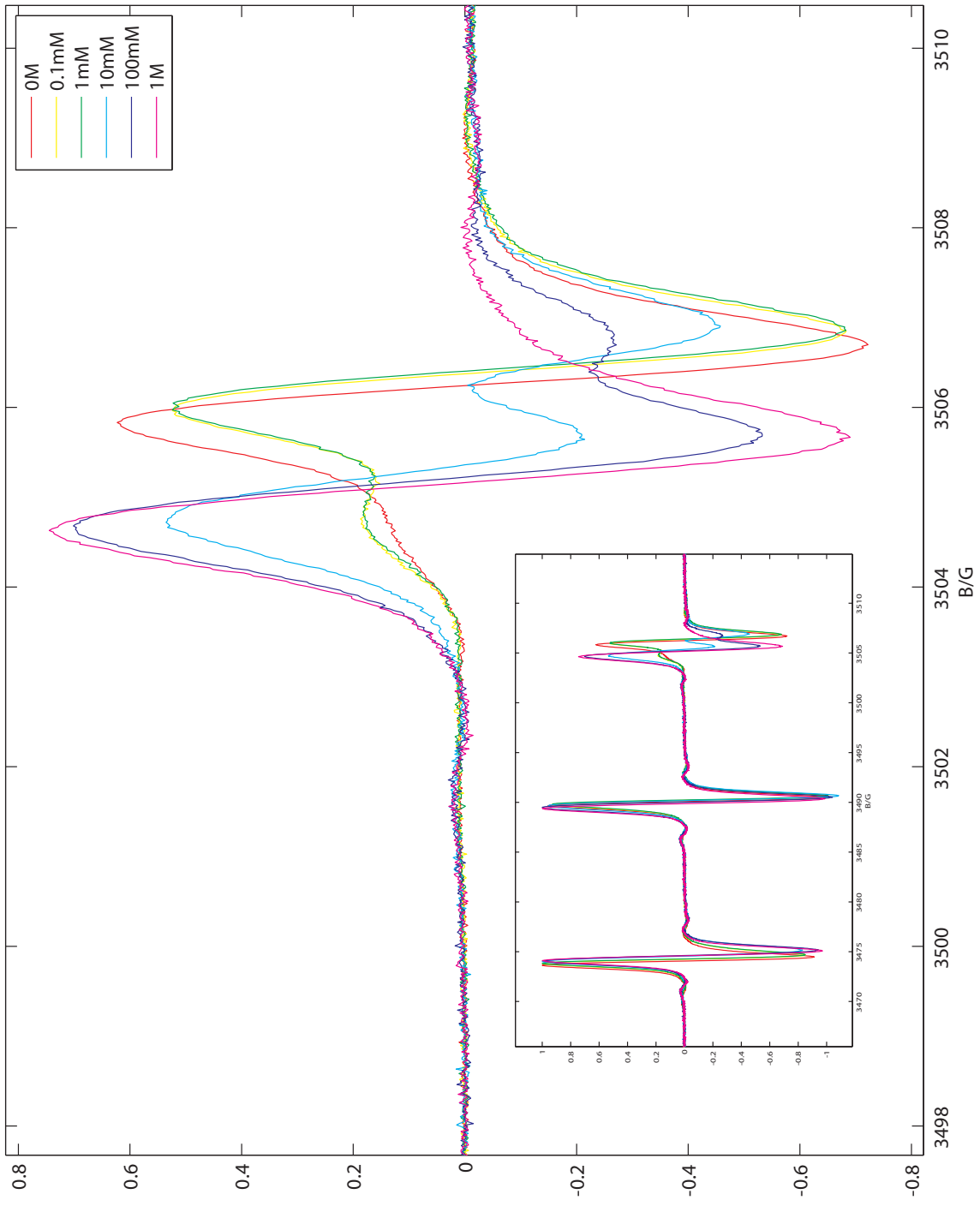

Figure B.6.: High-field peaks and full spectra of N1 with different concentrations of zinc iodide. Red: N1 without added salt, yellow: 0.1 mM ZnI_2, green: 1 mM ZnI_2, cyan: 10 mM ZnI_2, blue: 100 mM ZnI_2, magenta: 1 M ZnI_2.

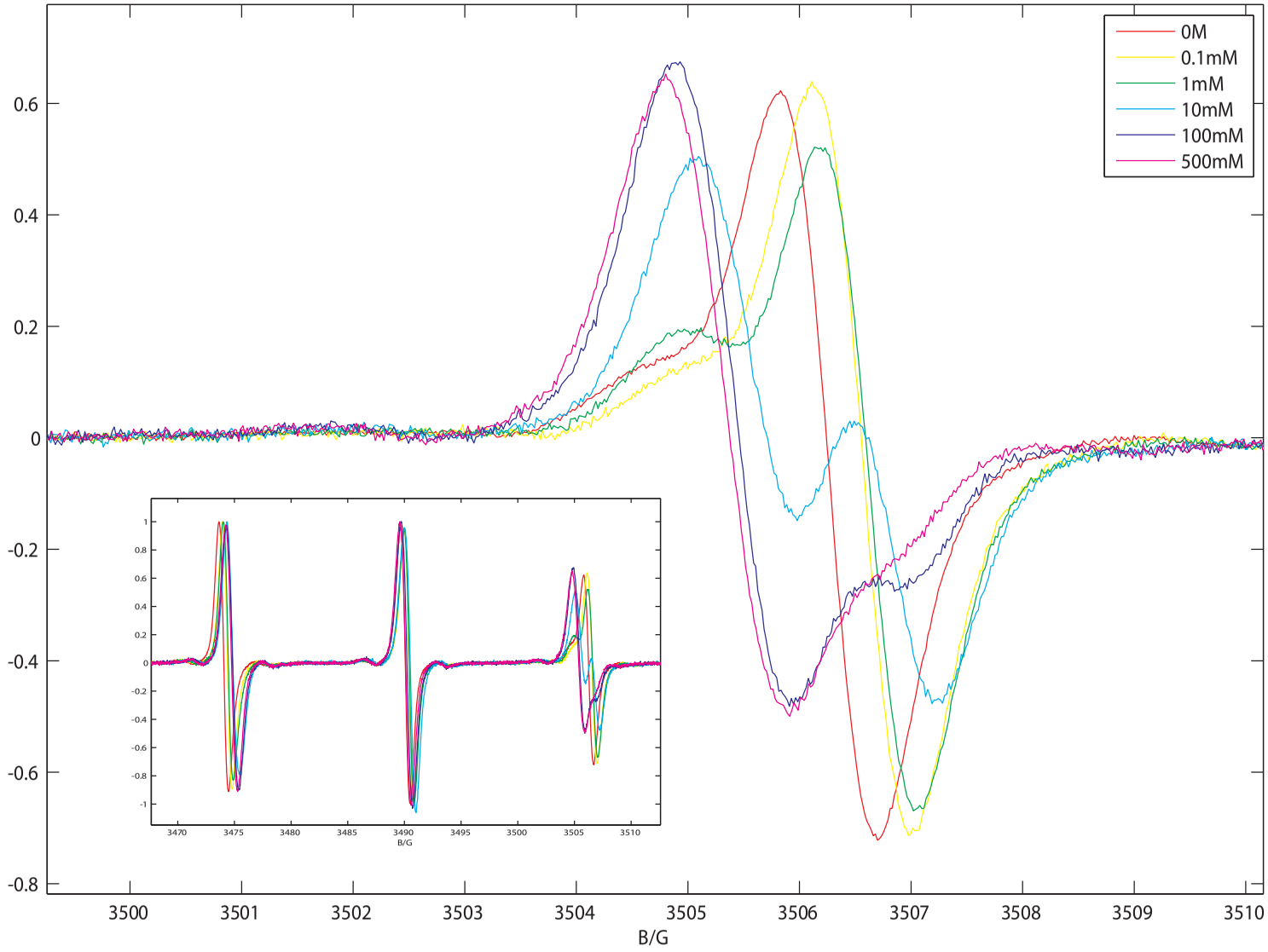

Figure B.7.: High-field peaks and full spectra of N1 with different concentrations of zinc acetate. Red: N1 without added salt, yellow: 0.1 mM $Zn(O_2CCH_3)_2$, green: 1 mM $Zn(O_2CCH_3)_2$, cyan: 10 mM $Zn(O_2CCH_3)_2$, blue: 100 mM $Zn(O_2CCH_3)_2$, magenta: 500 mM $Zn(O_2CCH_3)_2$.

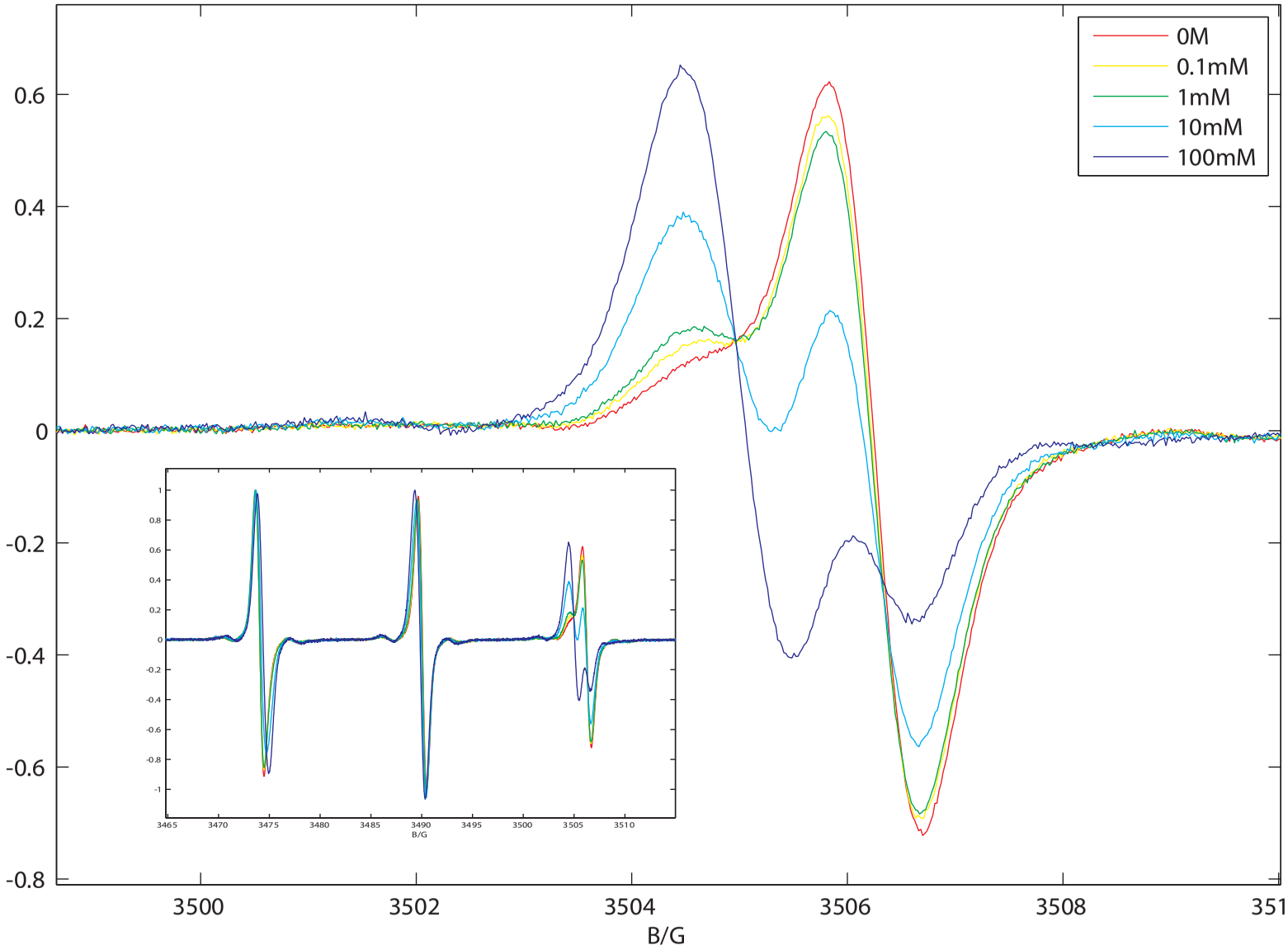

Figure B.8.: High-field peaks and full spectra of N1 with different concentrations of zinc sulfate. Red: N1 without added salt, yellow: 0.1 mM $ZnSO_4$, green: 1 mM $ZnSO_4$, cyan: 10 mM $ZnSO_4$, blue: 100 mM $ZnSO_4$.

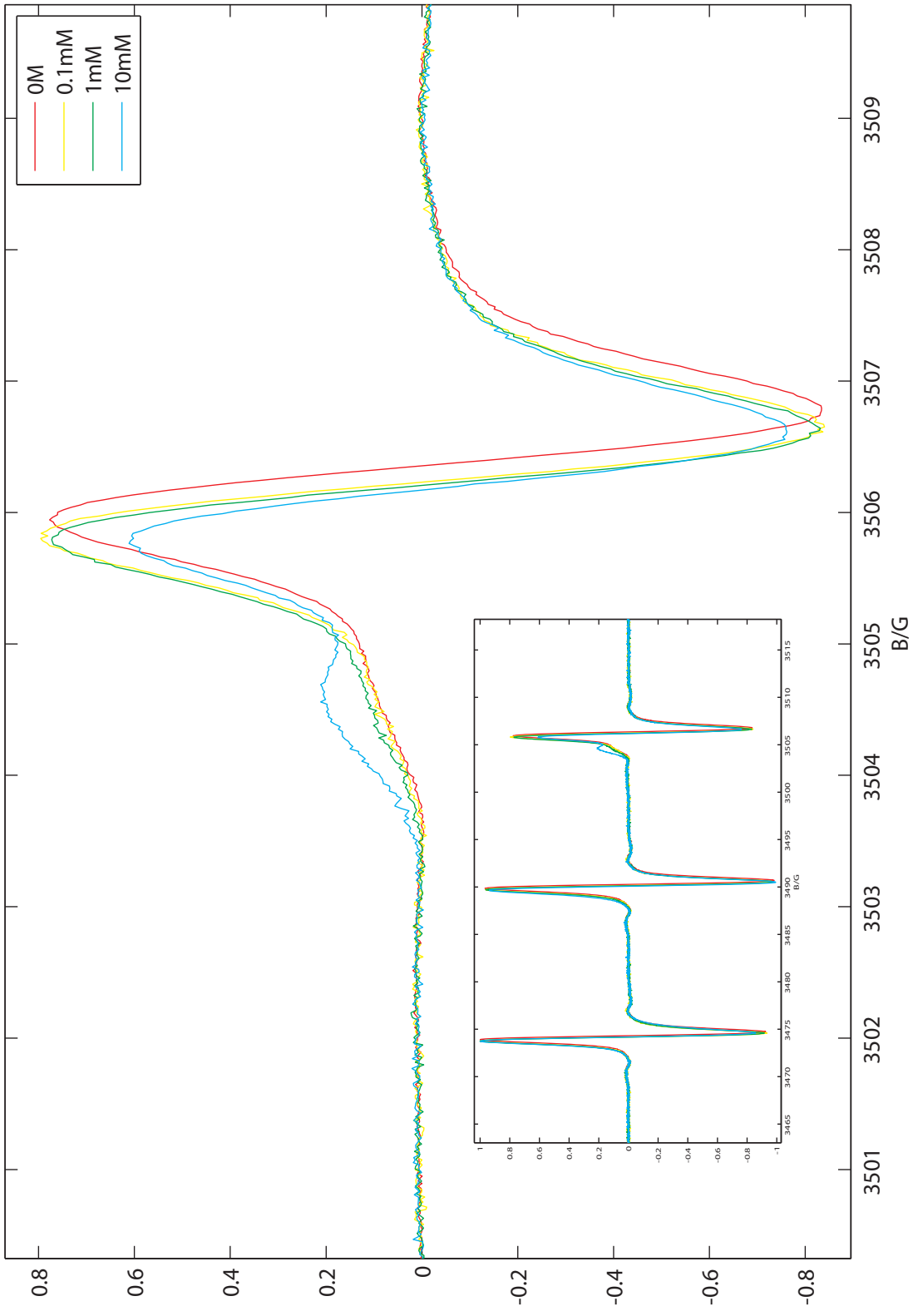

Figure B.9.: High-field peaks and full spectra of N2 with different concentrations of zinc fluoride. Red: N2 without added salt, yellow: 0.1 mM ZnF_2, green: 1 mM ZnF_2, cyan: 10 mM ZnF_2.

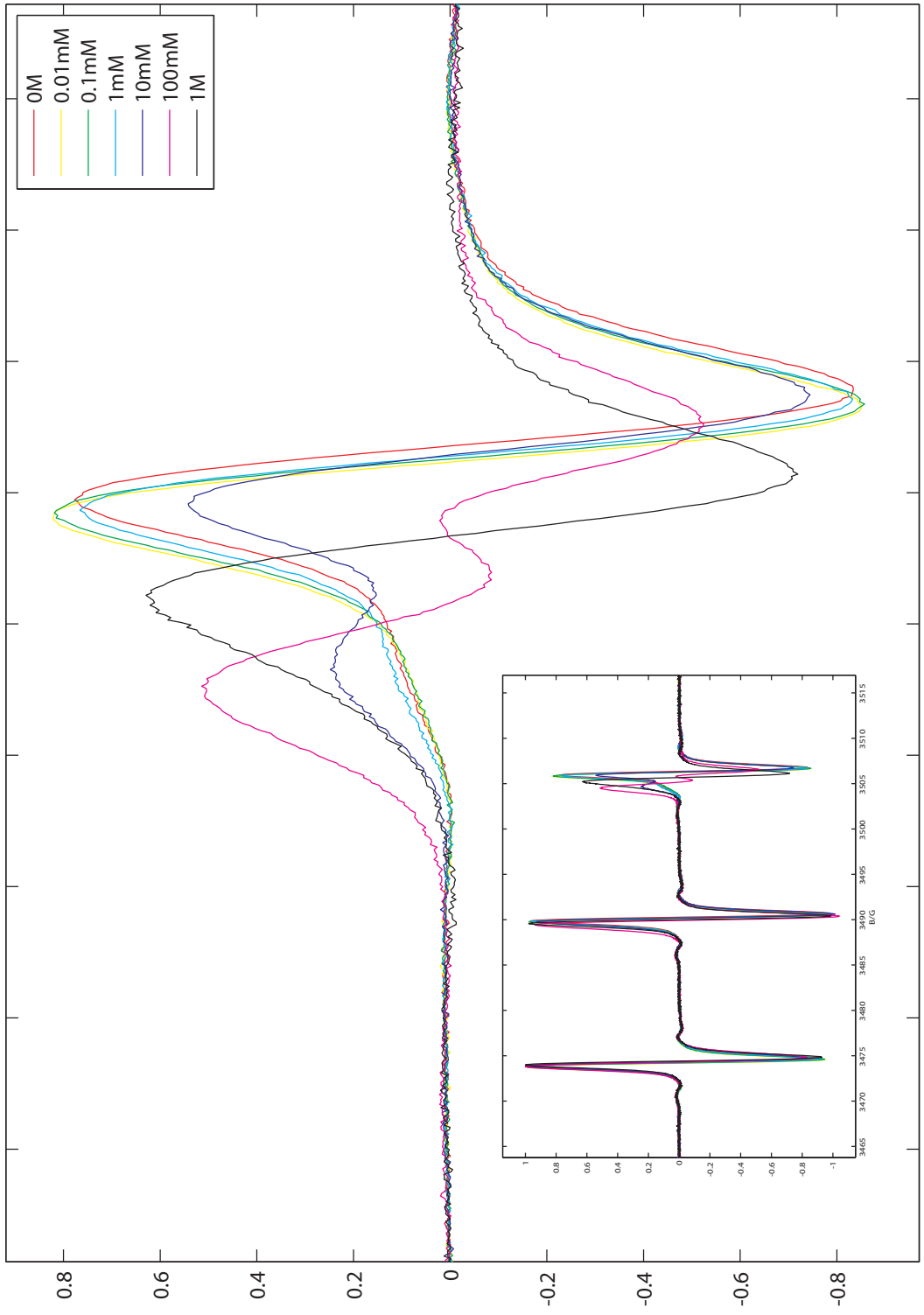

Figure B.10.: High-field peaks and full spectra of N2 with different concentrations of zinc chloride. Red: N2 without added salt, yellow: 0.01 mM $ZnCl_2$, green: 0.1 mM $ZnCl_2$, cyan: 1 mM $ZnCl_2$, blue: 10 mM $ZnCl_2$, magenta: 100 mM $ZnCl_2$, black: 1 M $ZnCl_2$.

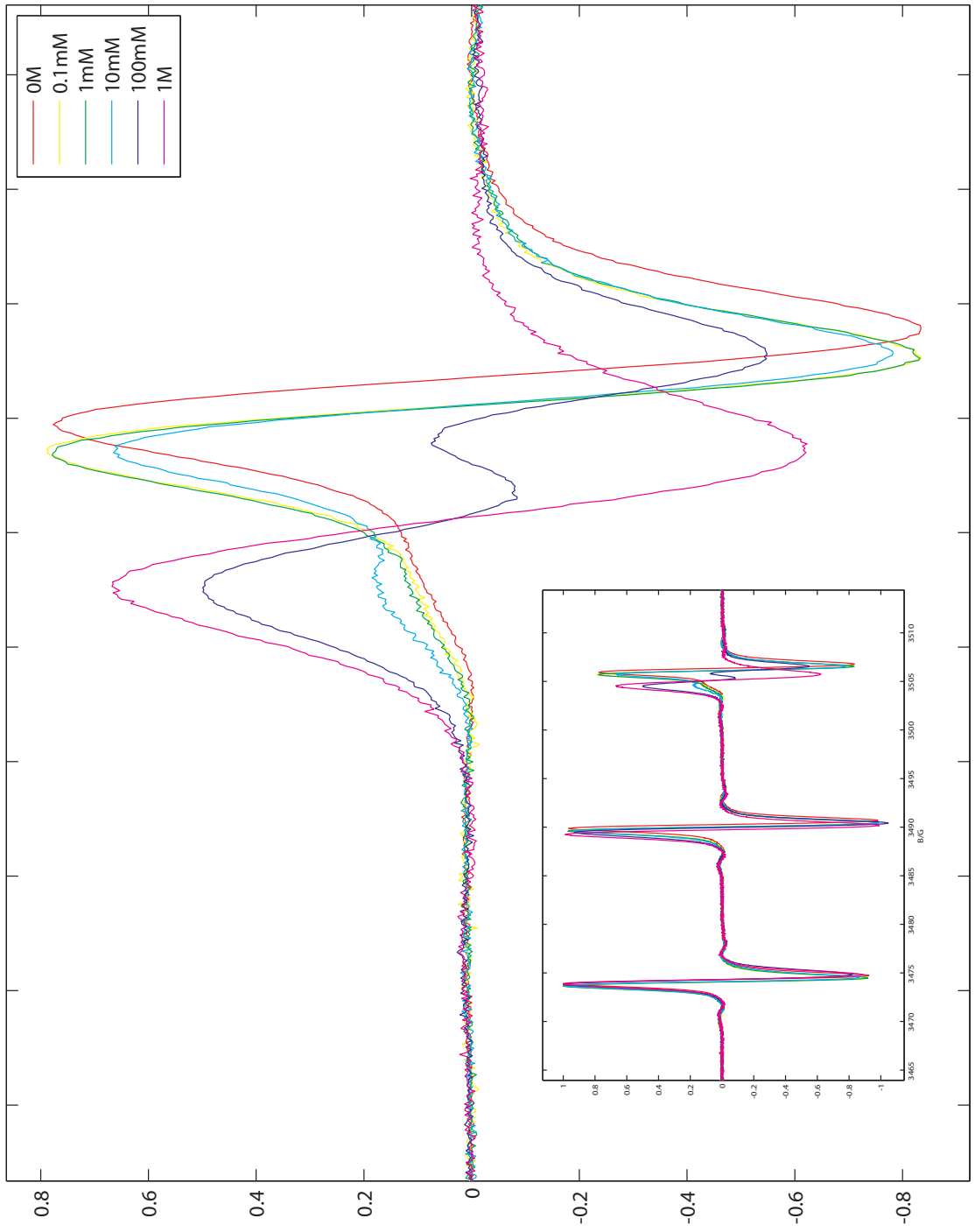

Figure B.11.: High-field peaks and full spectra of N2 with different concentrations of zinc bromide. Red: N2 without added salt, yellow: 0.1 mM $ZnBr_2$, green: 1 mM $ZnBr_2$, cyan: 10 mM $ZnBr_2$, blue: 100 mM $ZnBr_2$, magenta: 1 M $ZnBr_2$.

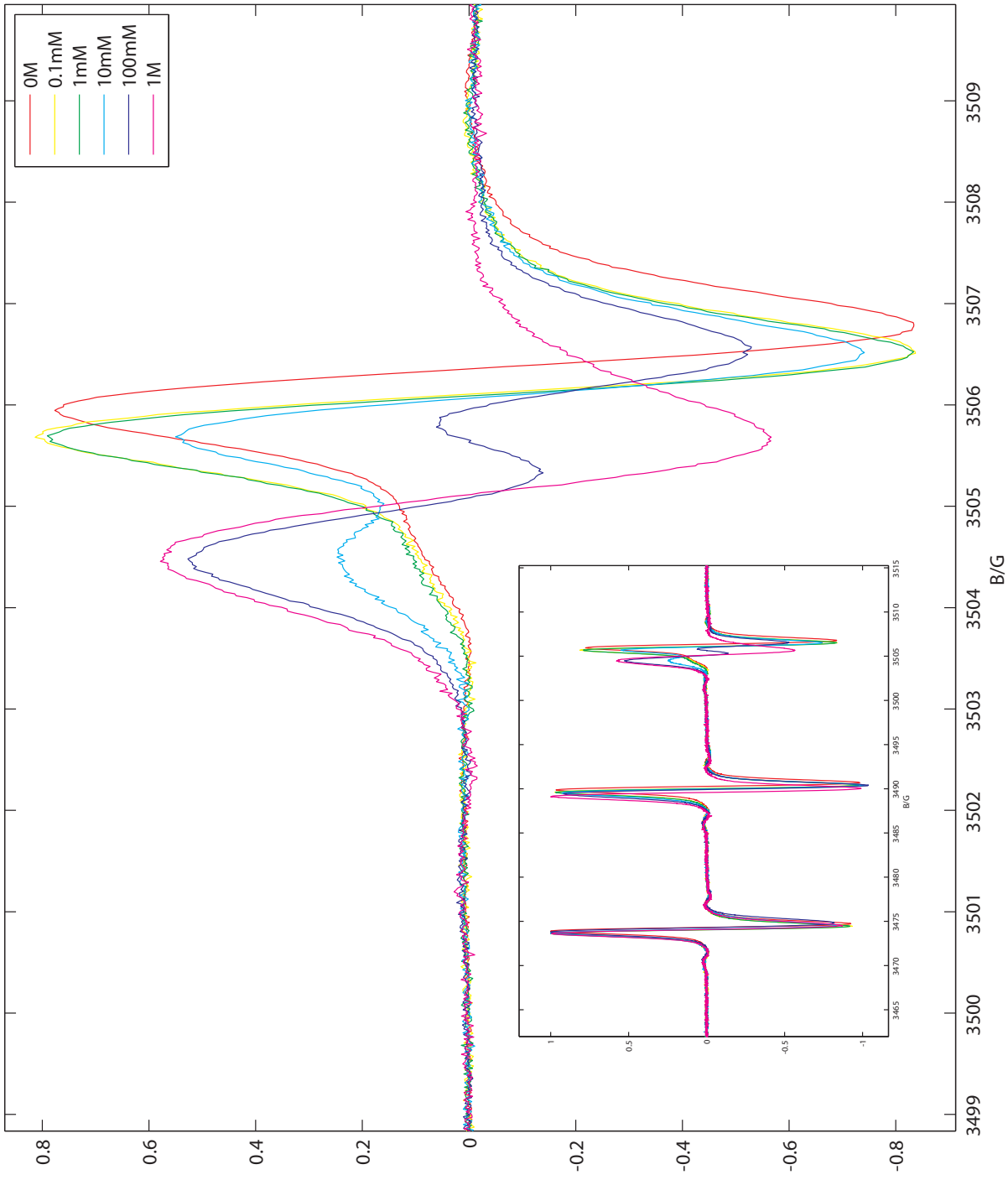

Figure B.12.: High-field peaks and full spectra of N2 with different concentrations of zinc iodide. Red: N2 without added salt, yellow: 0.1 mM ZnI_2, green: 1 mM ZnI_2, cyan: 10 mM ZnI_2, blue: 100 mM ZnI_2, magenta: 1 M ZnI_2.

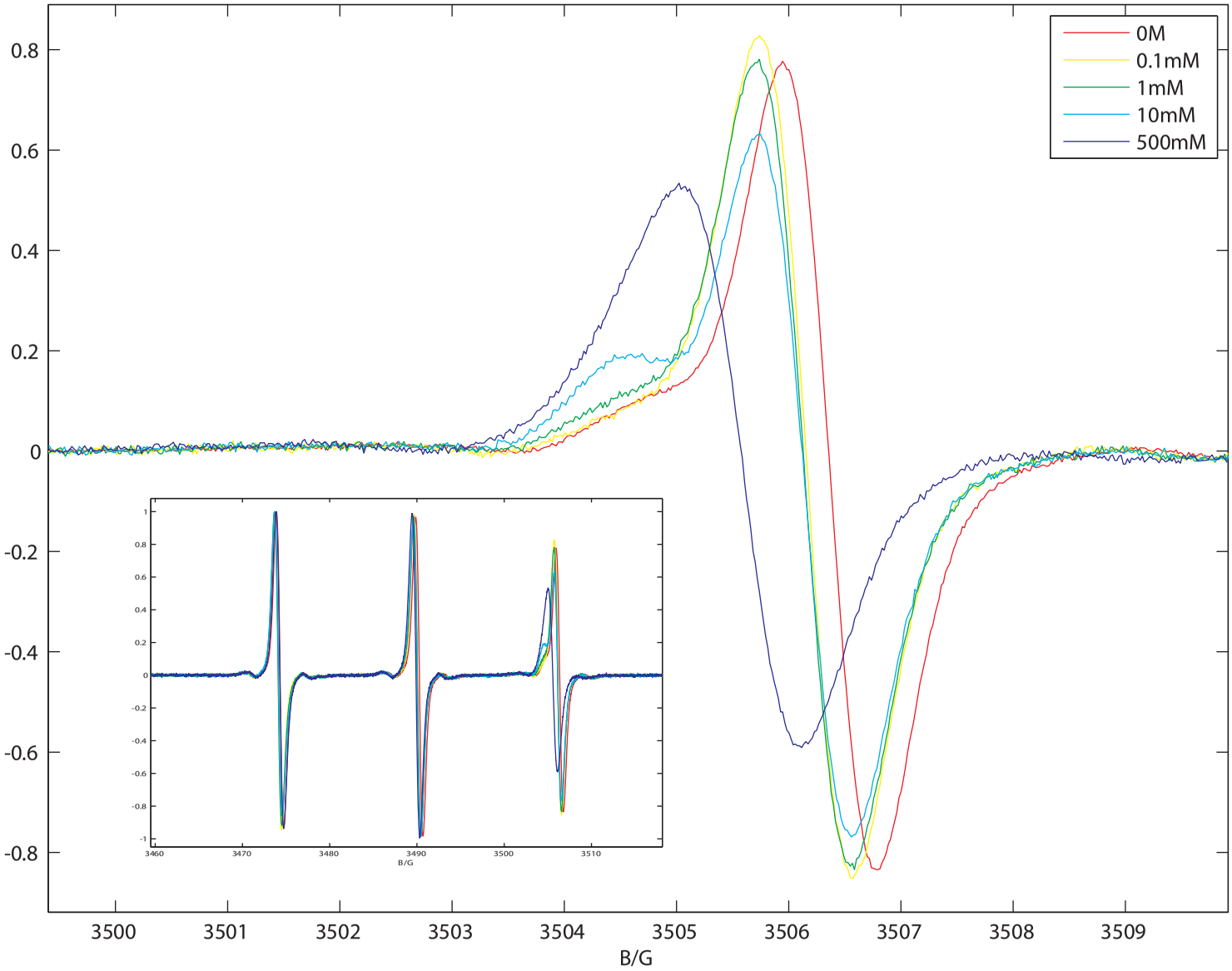

Figure B.13.: High-field peaks and full spectra of N2 with different concentrations of zinc acetate. Red: N2 without added salt, yellow: 0.1 mM $Zn(O_2CCH_3)_2$, green: 1 mM $Zn(O_2CCH_3)_2$, cyan: 10 mM $Zn(O_2CCH_3)_2$, blue: 500 mM $Zn(O_2CCH_3)_2$.

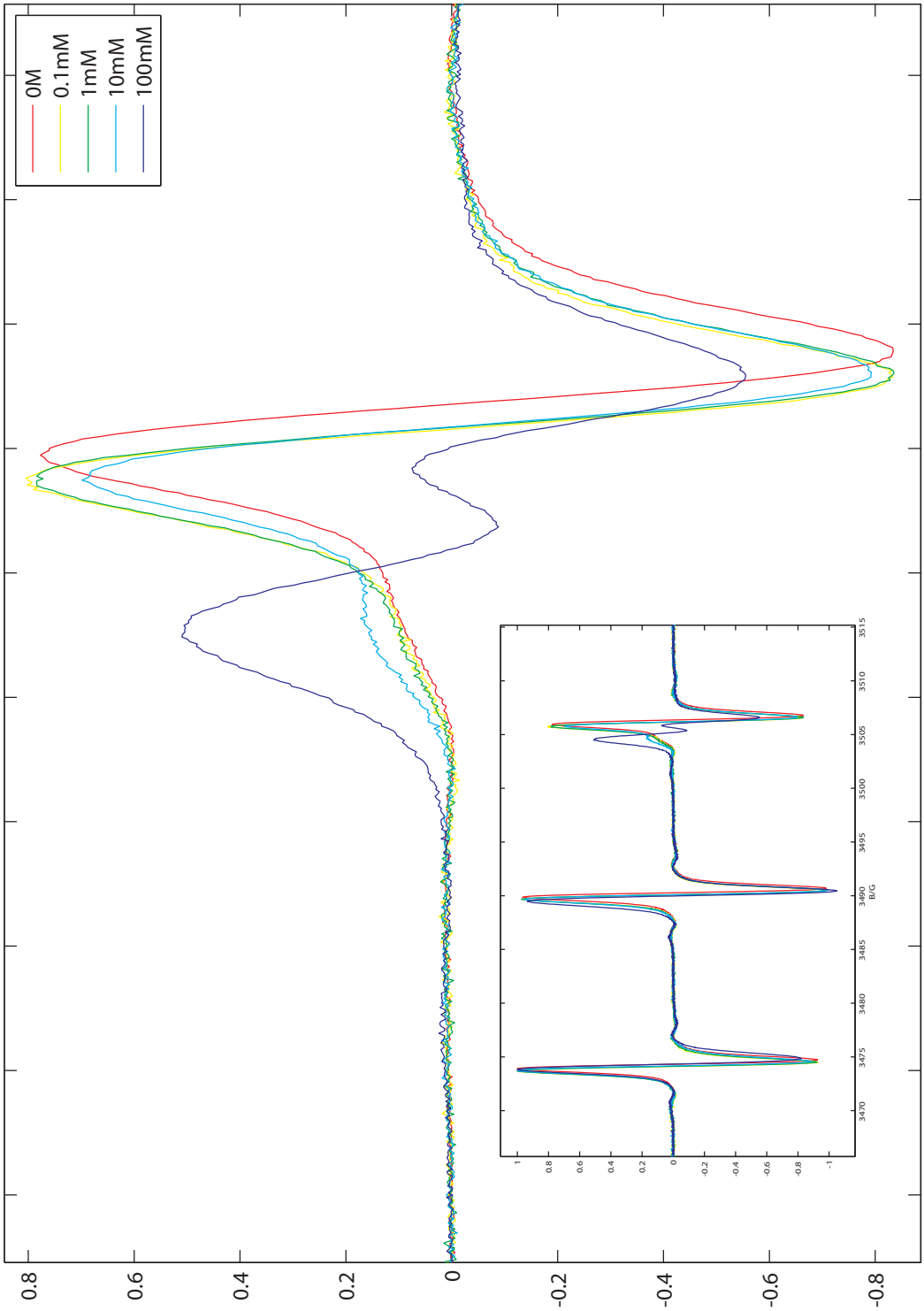

Figure B.14.: High-field peaks and full spectra of N2 with different concentrations of zinc sulfate. Red: N2 without added salt, yellow: 0.1 mM $ZnSO_4$, green: 1 mM $ZnSO_4$, cyan: 10 mM $ZnSO_4$, blue: 100 mM $ZnSO_4$.

Supplementary Material

C. Fitted Titration Curves

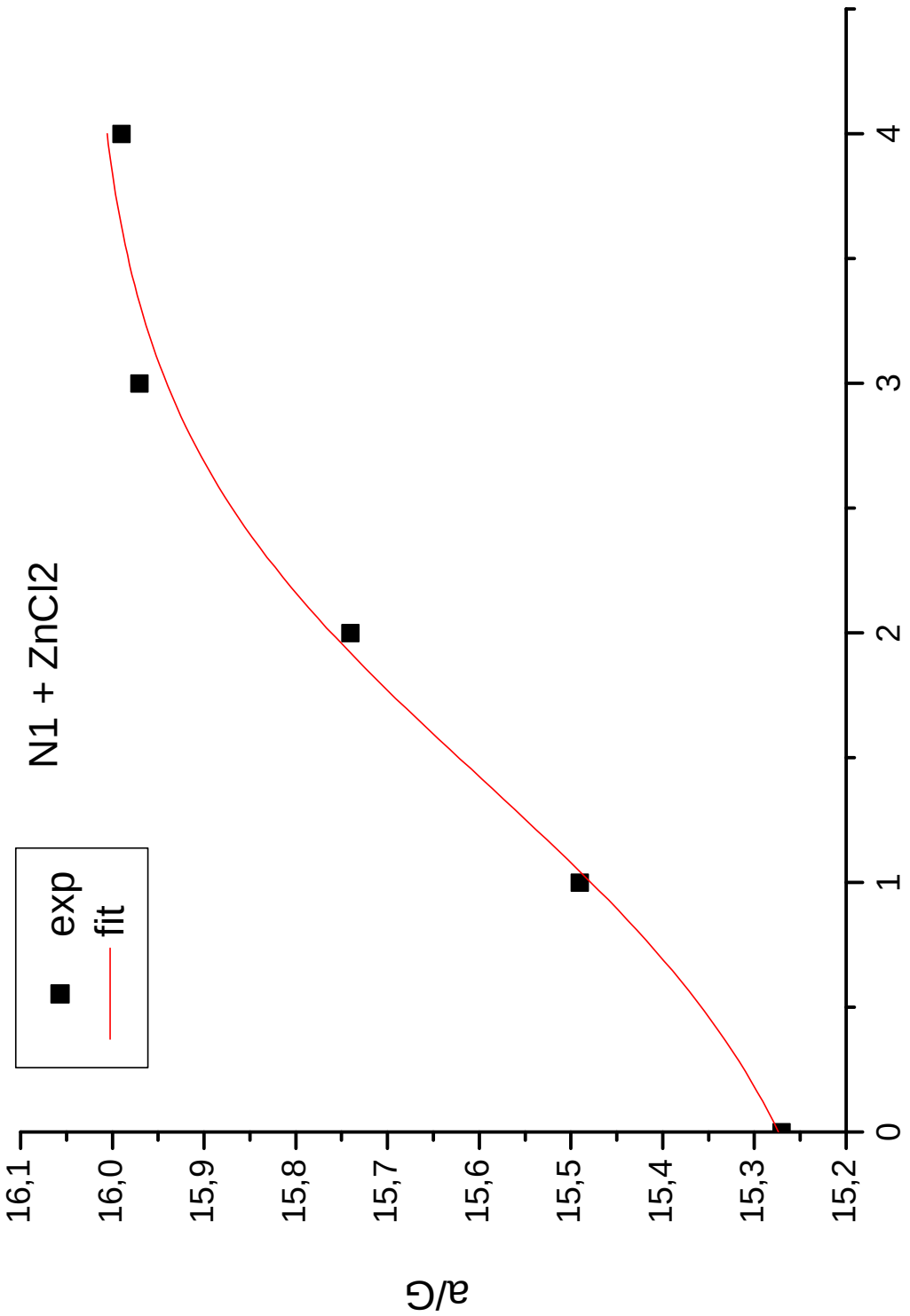

Figure C.1.: Sigmoidal fit of the titration curve for the system N1 + $ZnCl_2$. Squares: experimental values, line: fit according to Equation 4.3

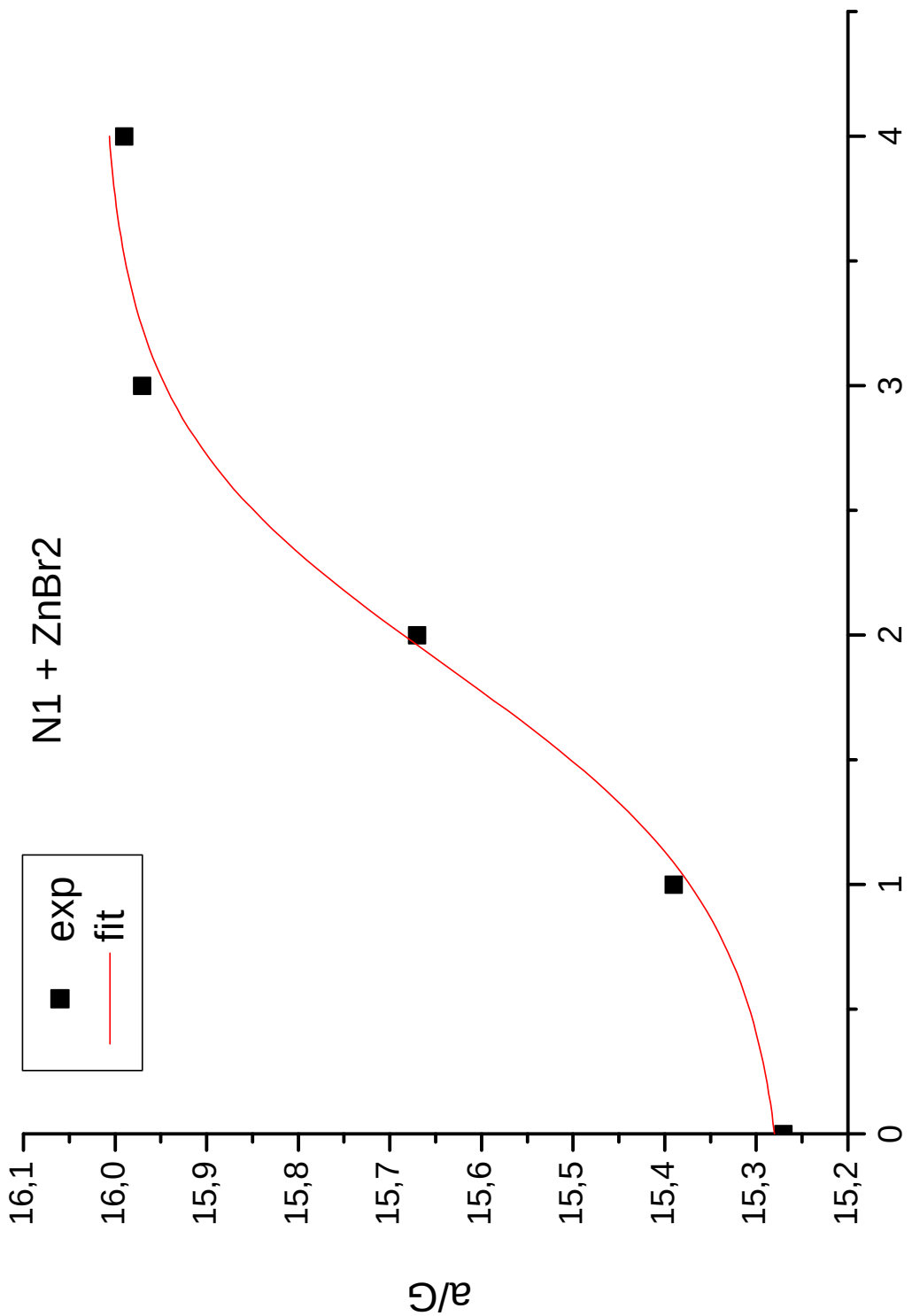

Figure C.2.: Sigmoidal fit of the titration curve for the system N1 + $ZnBr_2$. Squares: experimental values, line: fit according to Equation 4.3

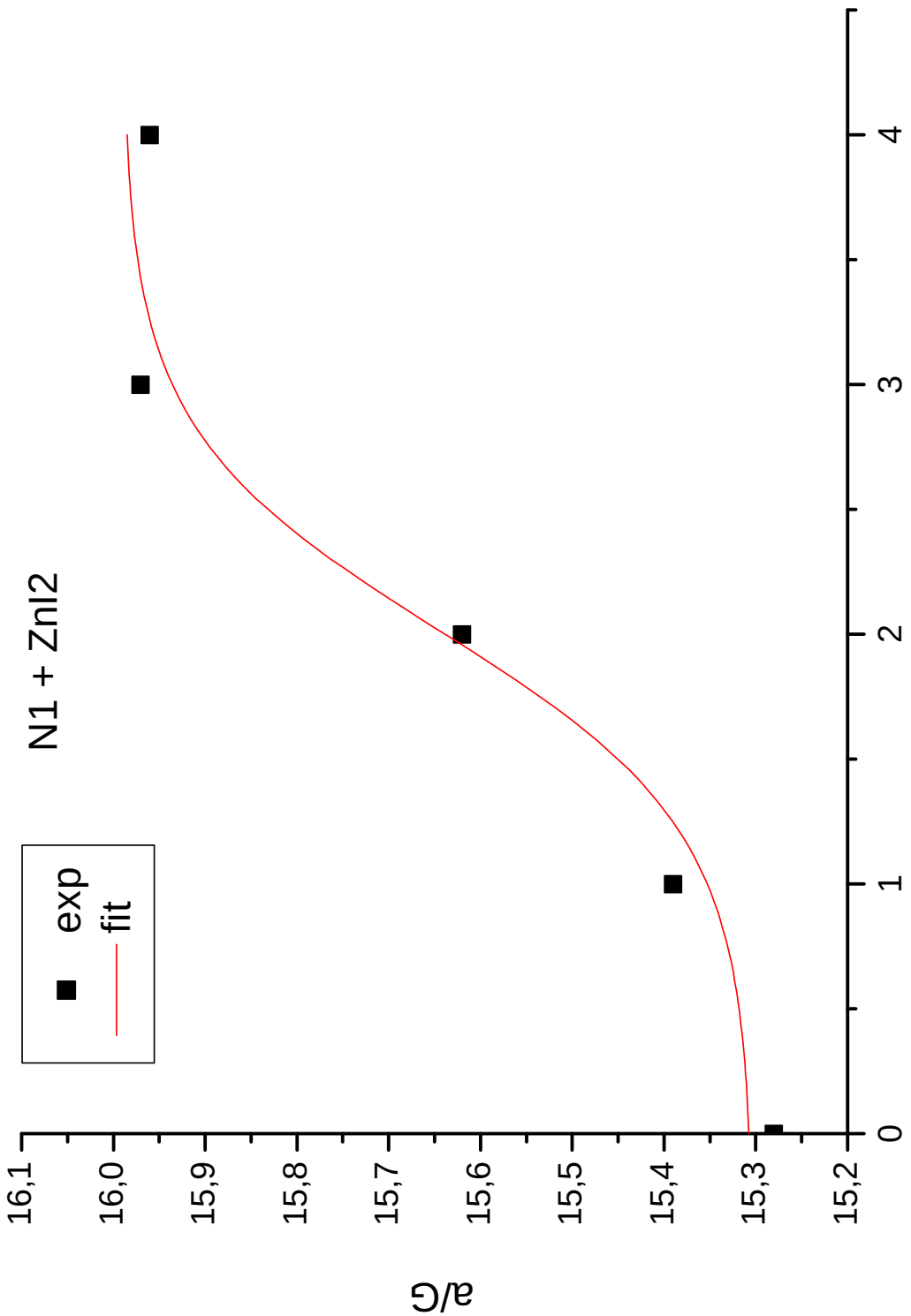

Figure C.3.: Sigmoidal fit of the titration curve for the system N1 + ZnI_2. Squares: experimental values, line: fit according to Equation 4.3

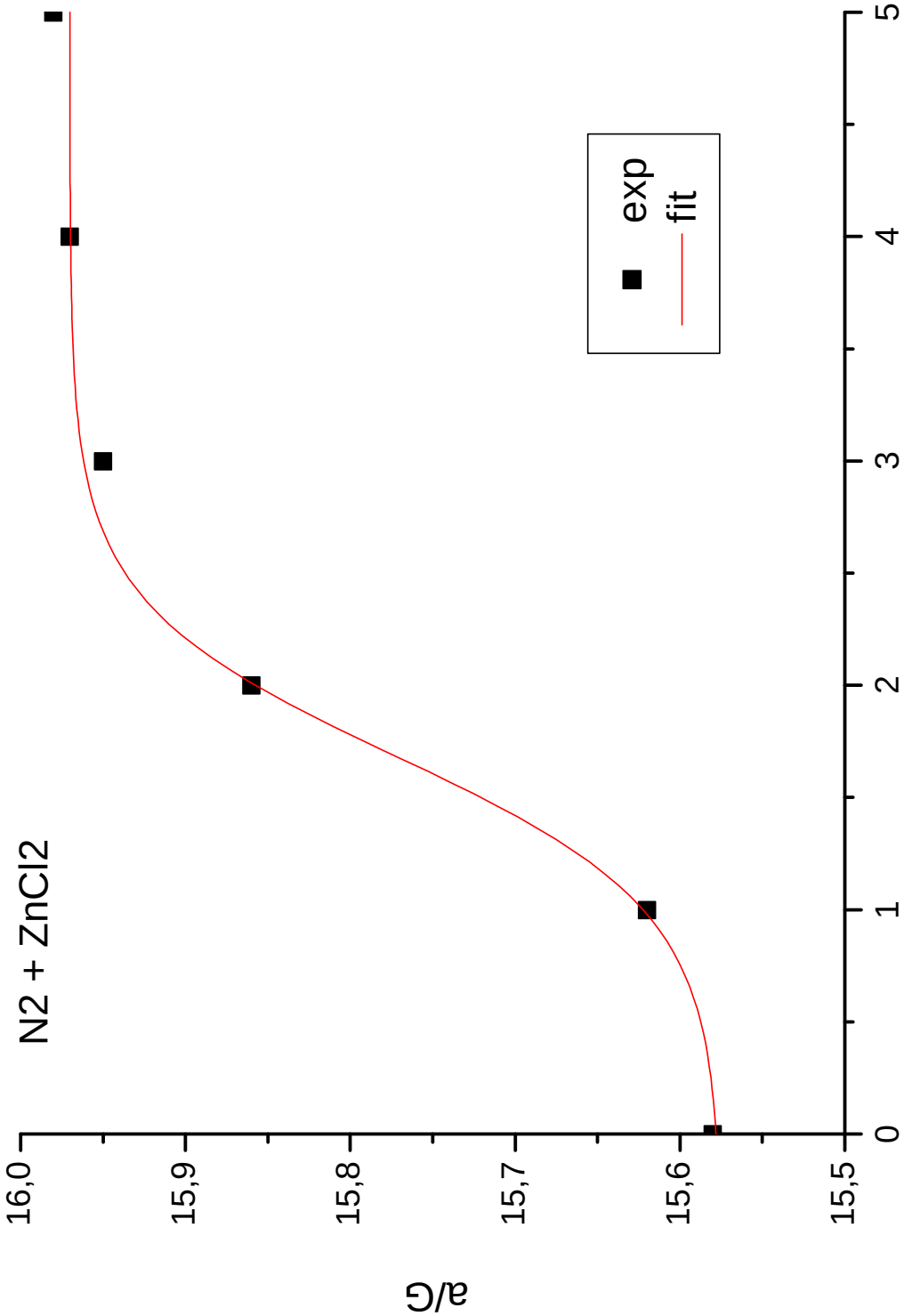

Figure C.4.: Sigmoidal fit of the titration curve for the system N2 + $ZnCl_2$. Squares: experimental values, line: fit according to Equation 4.3

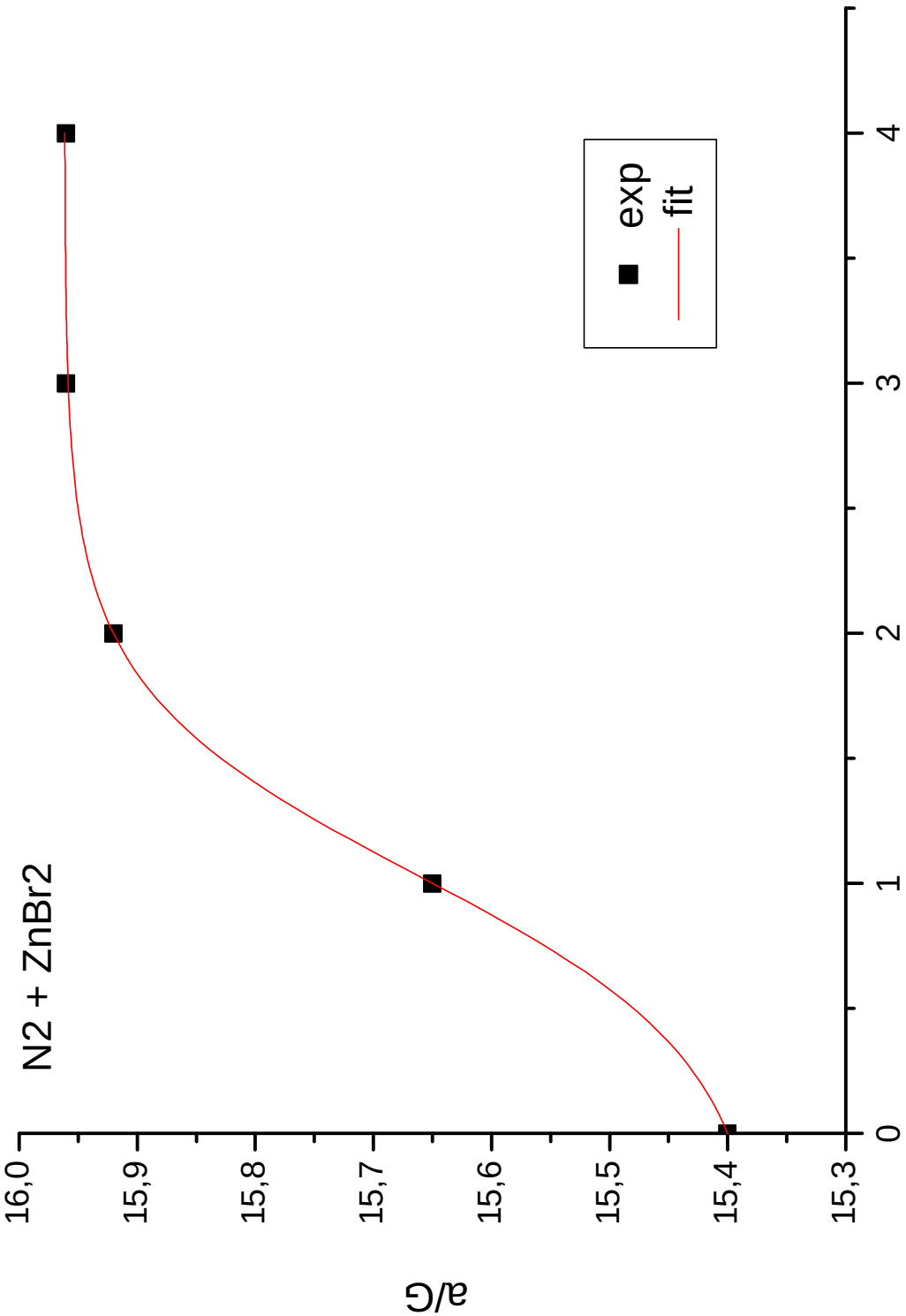

Figure C.5.: Sigmoidal fit of the titration curve for the system N2 + $ZnBr_2$. Squares: experimental values, line: fit according to Equation 4.3

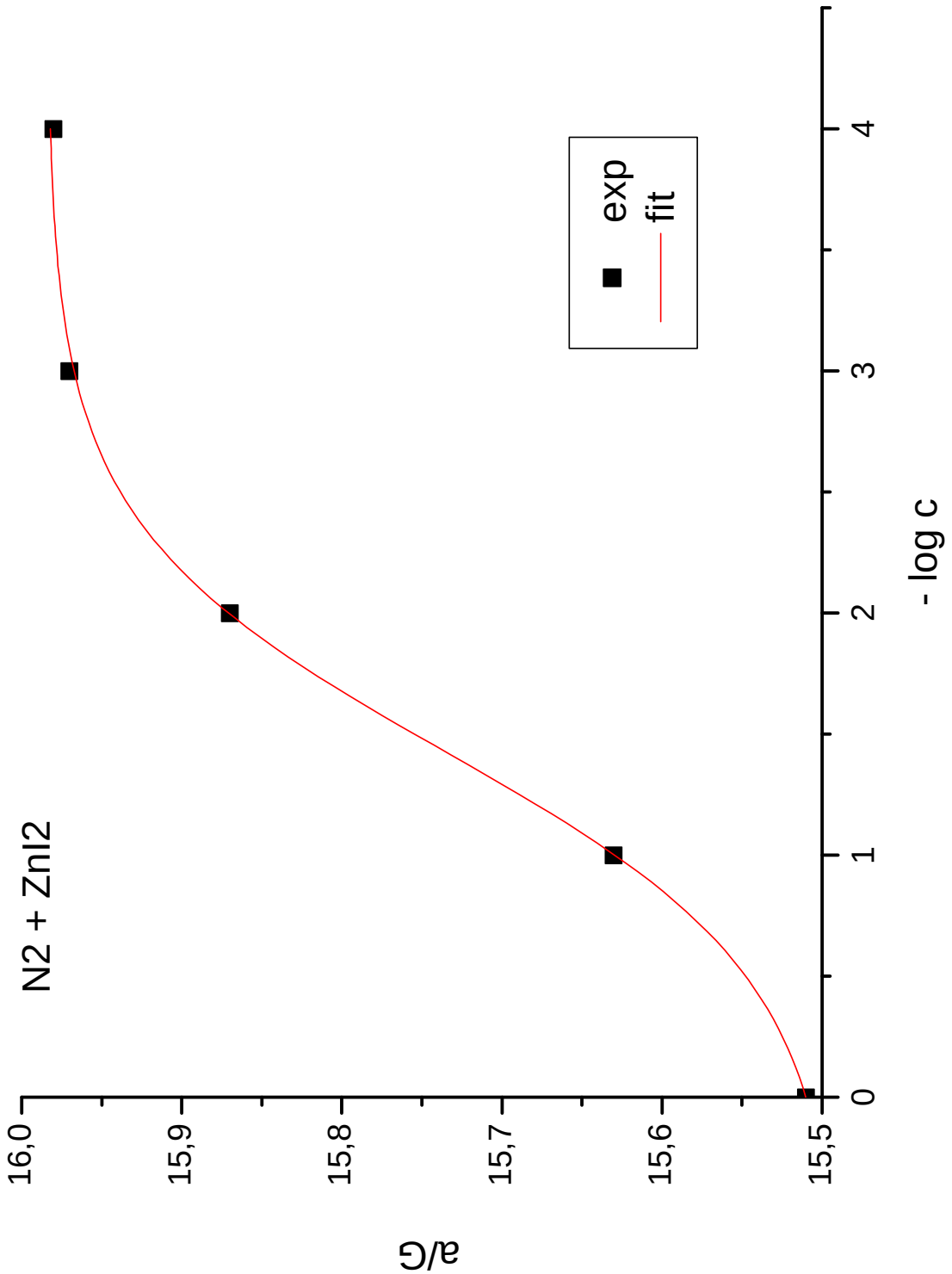

Figure C.6.: Sigmoidal fit of the titration curve for the system N2 + ZnI_2. Squares: experimental values, line: fit according to Equation 4.3

Supplementary Material

D. Calculated Structures

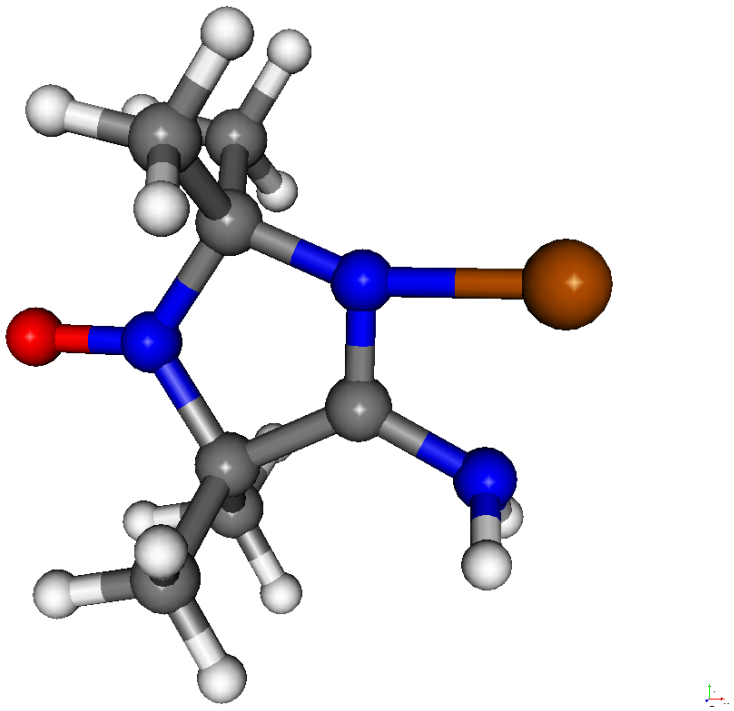

Figure D.1.: Calculated structure of the lithium-N2 complex.

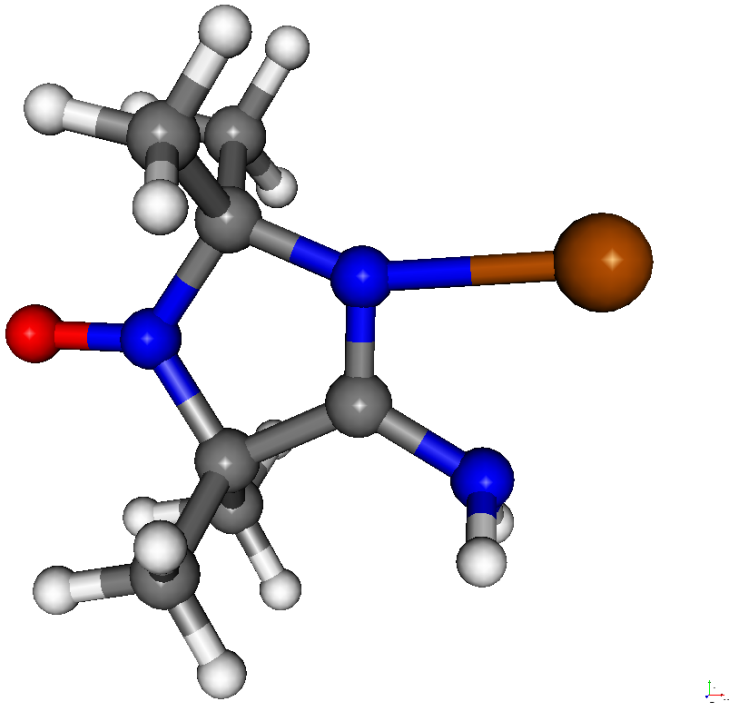

Figure D.2.: Calculated structure of the sodium-N2 complex.

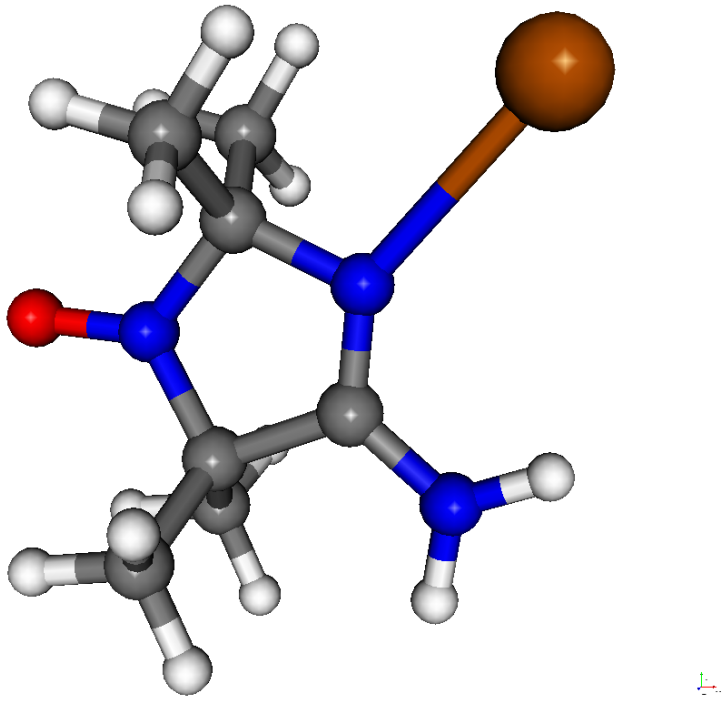

Figure D.3.: Calculated structure of the kalium-N2 complex.

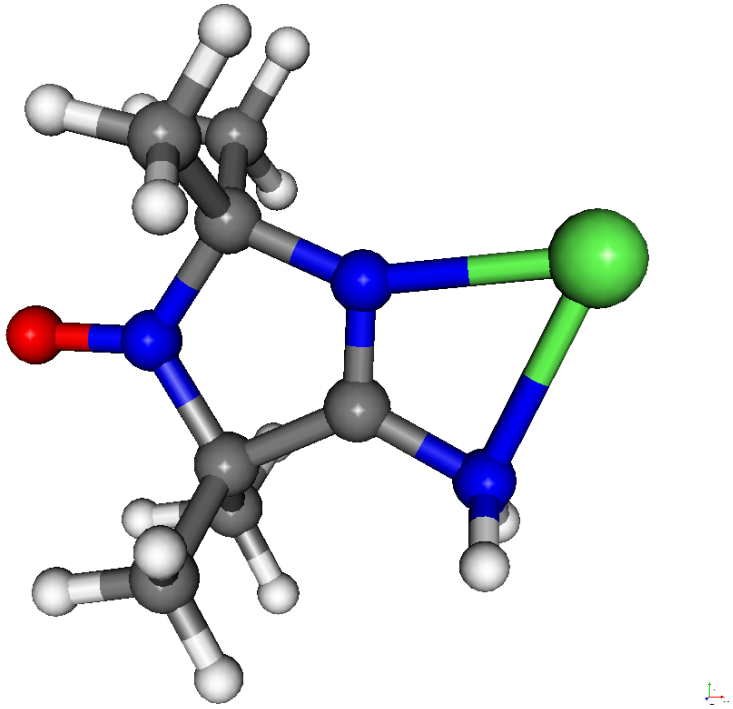

Figure D.4.: Calculated structure of the calcium-N2 complex.

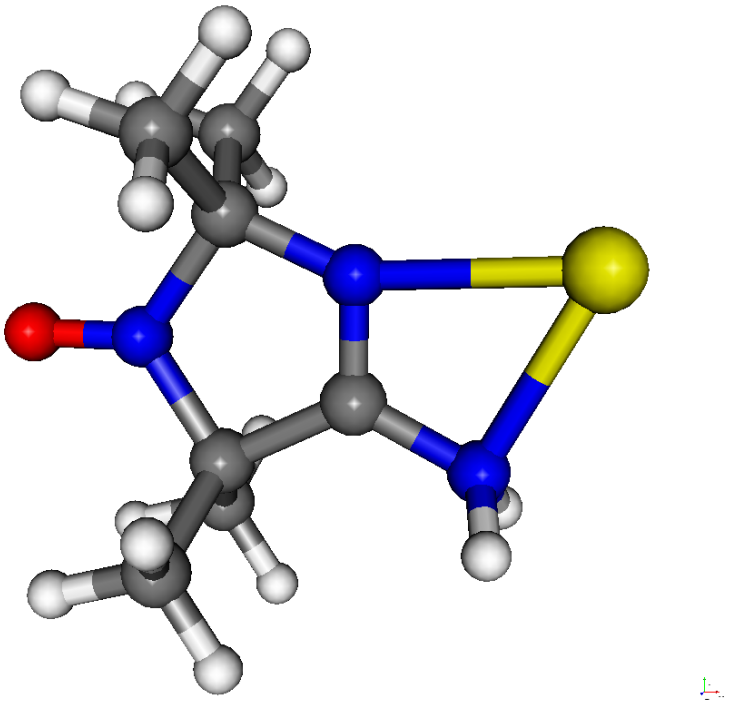

Figure D.5.: Calculated structure of the zinc-N2 complex.